

DESIGN OF KALMAN FILTER BASED  
ATTITUDE DETERMINATION ALGORITHMS FOR A LEO SATELLITE  
AND FOR A SATELLITE ATTITUDE CONTROL TEST SETUP

A THESIS SUBMITTED TO  
THE GRADUATE SCHOOL OF NATURAL AND APPLIED SCIENCES  
OF  
MIDDLE EAST TECHNICAL UNIVERSITY

BY

AYKUT KUTLU

IN PARTIAL FULFILLMENT OF THE REQUIREMENTS  
FOR  
THE DEGREE OF MASTER OF SCIENCE  
IN  
AEROSPACE ENGINEERING

SEPTEMBER 2008

Approval of the thesis:

**DESIGN OF KALMAN FILTER BASED  
ATTITUDE DETERMINATION ALGORITHMS FOR A LEO SATELLITE  
AND FOR A SATELLITE ATTITUDE CONTROL TEST SETUP**

submitted by **AYKUT KUTLU** in partial fulfillment of the requirements for the degree of **Master of Science in the Department of Aerospace Engineering, Middle East Technical University** by,

Prof. Dr. Canan Özgen  
Dean, Graduate School of **Natural and Applied Sciences**

\_\_\_\_\_

Prof. Dr. İsmail Hakkı Tuncer  
Head of department, **Aerospace Engineering**

\_\_\_\_\_

Prof. Dr. Ozan Tekinalp  
Supervisor, **Aerospace Engineering Department, METU**

\_\_\_\_\_

**Examining Committee Members:**

Dr. İlkey Yavrucuk  
Aerospace Engineering Department, METU

\_\_\_\_\_

Prof. Dr. Ozan Tekinalp  
Aerospace Engineering Department, METU

\_\_\_\_\_

Dr. Güçlü Seber  
Aerospace Engineering Department, METU

\_\_\_\_\_

Prof. Dr. Tuna Balkan  
Mechanical Engineering Department, METU

\_\_\_\_\_

Dr. Volkan Nalbantoğlu  
ASELSAN, MGEO

\_\_\_\_\_

**Date:**

10 September 2008

**I hereby declare that all information in this document has been obtained and presented in accordance with academic rules and ethical conduct. I also declare that, as required by these rules and conduct, I have fully cited and referenced all material and results that are not original to this work.**

Name, Last name : Aykut Kutlu

Signature :

## ABSTRACT

### DESIGN OF KALMAN FILTER BASED ATTITUDE DETERMINATION ALGORITHMS FOR A LEO SATELLITE AND FOR A SATELLITE ATTITUDE CONTROL TEST SETUP

Kutlu, Aykut  
M.S., Aerospace Engineering Department  
Supervisor : Prof. Dr. Ozan Tekinalp

September 2008, 169 pages

This thesis presents the design of Kalman filter based attitude determination algorithms for a hypothetical LEO satellite and for a satellite attitude control test setup.

For the hypothetical LEO satellite, an Extended Kalman Filter based attitude determination algorithms are formed with a multi-mode structure that employs the different sensor combinations and as well as online switching between these combinations depending on the sensor availability. The performance of these different attitude determination modes are investigated through Monte Carlo simulations. New attitude determination algorithms are prepared for the satellite attitude control test setup by considering the constraints on the selection of the suitable sensors. Here, performances of the Extended Kalman Filter and Unscented Kalman Filter are investigated. It is shown that robust and sufficiently accurate attitude estimation for the test setup is achievable by using the Unscented Kalman Filter.

**Keyword:** Extended Kalman Filter, Unscented Kalman Filter, Attitude Determination System, Satellite Attitude Control Test Setup, Sensor Fusion Algorithms, Attitude Determination Algorithms.

## ÖZ

### BİR ALÇAK YÖRÜNGE UYDUSU VE BİR UYDU YÖNELİM KONTROL TEST DÜZENEĞİ İÇİN KALMAN FİLTRE TABANLI YÖNELİM SAPTAMA AGORİTMALARI TASARIMI

Kutlu, Aykut  
Yüksek Lisans, Havacılık ve Uzay Mühendisliği Bölümü  
Tez Yöneticisi : Prof. Dr. Ozan Tekinalp

Eylül 2008, 169 sayfa

Bu tez bir alçak yörünge uydusu ve bir uydu yönelim kontrol test düzeneği için Kalman filtre tabanlı yönelim saptama algoritmaları tasarımını sunmaktadır.

Hayali bir alçak yörünge uydusu için, farklı algılayıcı birleşimleri kullanan ve de bu birleşimler arasında algılayıcı kullanılabilirliklerine göre çevrimiçi anahtarlama yapan çoklu-mod yapısında Genişletilmiş Kalman Filtresi tabanlı yönelim tahmin algoritmaları oluşturulmuştur. Tasarlanan bu farklı algoritmaların başarımları Monte Carlo benzetimleriyle incelenmiştir. Uydu yönelim kontrol test düzeneği sistemi için kullanılabilir algılayıcı kısıtları göz önünde bulundurularak yeni yönelim saptama algoritmaları hazırlanmıştır. Burada, Genişletilmiş Kalman Filtresi ile Yansız Kalman Filtresi başarımları incelenmiştir. Bu çalışmalar sonucu test düzeneği için gürbüz ve yeterli hassasiyette yönelim tahminine Yansız Kalman Filtresi kullanılarak erişildiği gösterilmiştir.

**Anahtar Kelimeler:** Genişletilmiş Kalman Filtresi, Yansız Kalman Filtresi, Yönelim Saptama Sistemi, Uydu Yönelim Kontrol Test Düzeneği, Algılayıcı Birleştirme Algoritmaları , Yönelim Tahmin Algoritmaları.

*To My Wonderful Wife*

## **ACKNOWLEDGMENTS**

I wish to express my deepest gratitude to my supervisor Prof. Dr. Ozan TEKİNALP for its advice, guidance, encouragement and insight he has supplied throughout this thesis study.

I would like to express my gratitude to my under-graduate supervisor Prof. Dr. Çingiz Hacıyev, from İstanbul Technical University, for its supports and precious guidance.

I would like to thank Turkish Aerospace Industries, Inc. (TAI), my fellow co-workers (especially Emre YAVUZOĞLU) and my chief Erhan SOLAKOĞLU for their support.

I would also like to thank and express my gratitude to my father M. Levent KUTLU for his support during my education life and for his special enthusiasm to academic studies that has encouraged me during my academic studies as well.

Finally, I would express very special thanks to my wife Esra KUTLU for her continuous support, love and patience during my graduate education.

## TABLE OF CONTENTS

ABSTRACT .....	iv
ÖZ .....	v
ACKNOWLEDGMENTS .....	vii
TABLE OF CONTENTS .....	viii
LIST OF TABLES .....	xi
LIST OF FIGURES .....	xii
CHAPTERS	
1 INTRODUCTION .....	1
2 SATELLITE SIMULATION MODEL.....	5
2.1 Satellite Rotational Motion Model.....	5
2.1.1 Dynamic Equations .....	5
2.1.2 Kinematics Equations .....	8
2.1.3 Satellite Specifications .....	9
2.2 Disturbances Torques.....	10
2.2.1 Gravity Gradient Torque.....	11
2.2.2 Solar Radiation Torque .....	12
2.2.3 Magnetic Field Torque.....	15
2.2.4 Aerodynamics Torque.....	16
2.2.5 Total Disturbances Torque.....	18
2.3 Reference Models.....	19
2.3.1 Orbit Propagator Model .....	20
2.3.2 Sun Position Model.....	30
2.3.3 Earth Magnetic Field Model .....	33
2.4 Sensor Measurements Models .....	37
2.4.1 Rate Gyroscopes .....	37
2.4.2 Sun Sensor.....	43
2.4.3 Magnetometers.....	45
2.4.4 Star Sensor .....	46
3 KALMAN FILTER BASED SATELLITE ATTITUDE DETERMINATION ...	49

3.1	Kalman Filter Theory and Modeling .....	49
3.1.1	Linear Continuous Kalman Filter.....	49
3.1.2	Linear Discrete Kalman Filter.....	53
3.1.3	Extended Kalman Filter .....	57
3.1.4	Filter Tuning .....	60
3.2	Satellite Attitude Determination System Structure.....	60
3.3	Angular Rate Estimation at Detumbling Mode.....	63
3.4	Coarse Full State Estimation.....	69
3.5	Accurate Full State Estimation.....	90
3.6	A Multimode Attitude Determination System.....	104
3.7	Conclusion .....	108
4	ATTITUDE DETERMINATION FOR THE SATELLITE ATTITUDE CONTROL TEST SETUP .....	109
4.1	SACoTS Simulation Model .....	109
4.2	SACoTS Sensor Measurements Models .....	113
4.3	SACoTS Attitude Determination System and Algorithms .....	116
4.3.1	Unscented Kalman Filter.....	117
4.3.2	Full State Estimation of SACoTS .....	121
4.4	Conclusion .....	138
5	CONCLUSION.....	141
	REFERENCES.....	143
	APPENDICES	
A.	DEFINITIONS AND NOTATIONS .....	146
A.1	Reference Frames.....	146
A.1.1	Earth-Centered Inertial (ECI) Reference Frames.....	146
A.1.2	Earth-Centered Earth Fixed (ECEF) Reference Frame.....	147
A.1.3	Orbit (ORB) Reference Frame .....	147
A.1.4	Earth-Centered Orbit (ECOF) Reference Frame.....	147
A.1.5	Body (BODY) Reference Frame.....	148
A.2	Attitude Representation.....	148
A.2.1	Direction Cosine Matrix.....	148
A.2.2	Euler Angles.....	149

A.2.3	Quaternions .....	151
A.2.4	Relationships Between DCM, Euler Angles and Quaternions.....	152
A.3	Transformation Between Different Frames.....	153
A.3.1	Transformation From ECOF to ECI and ECEF Frames .....	154
A.3.2	Transformation From ECEF to ECI Frame.....	154
A.3.3	Transformation From ECI to ORB Frame .....	154
A.3.4	Transformation From ECEF to ORB Frame .....	155
A.3.5	Transformation From ORB to BODY Frame .....	156
A.4	Kinematics Differential Equations.....	156
B.	SENSORS USED ON SATELLITE ADS SIMULATIONS .....	159
B.1	Rate Gyroscopes.....	159
B.2	Sun Sensor.....	161
B.3	Magnetometer.....	162
B.3	Star Sensor.....	164
C.	SENSORS USED ON SACOTS.....	165
D.	THREE AXIS SATELLITE ATTITUDE CONTROL TEST SETUPS.....	167
D.1	TASS (Three Axis Satellite Simulators).....	167
D.2	WHORL-1 and WHORL-2 .....	168
D.3	IACS-1 and IACS-2 .....	169

## LIST OF TABLES

### TABLES

Table 2-1: Orbital Parameters of the Hypothetical Satellite .....	10
Table 2-2: Error Parameters of the Rate Gyros Model .....	38
Table 2-3: NG FOG-200 specifications .....	43
Table 2-4: Magnetometer Specifications .....	46
Table 2-5: Star Sensor Specifications .....	48
Table 3-1: Continuous-time Linear Kalman Filter [4] .....	52
Table 3-2: Discrete-time Linear Kalman Filter [4] .....	56
Table 3-3: Discrete-time Extended Kalman Filter [4] .....	59
Table 3-4: Satellite ADS Modes .....	62
Table 3-5: Mode-1 Statistical Results of the Estimation Error .....	69
Table 3-6: Mode-2 Statistical Results of the Estimation Error .....	77
Table 3-7: Mode-3 Statistical Results of the Estimation Error .....	83
Table 3-8: Mode-4 Statistical Results of the Estimation Error .....	89
Table 3-9: Mode-5 Statistical Results of the Estimation Error .....	97
Table 3-10: Mode-6 Statistical Results of the Estimation Error .....	103
Table 4-1: SACoTS Parameters .....	112
Table 4-2: Accelerometer Error Parameters .....	114
Table 4-3: The Specifications of the IMU .....	116
Table 4-4: SACoTS ADS Modes .....	122
Table 4-5: Mode-s1 Statistical Results of the Estimation Error .....	130
Table 4-6: Mode-s2 Statistical Results of the Estimation Error .....	138
Table 4-7: The Performance Comparison Table of the EKF and UKF .....	139

## LIST OF FIGURES

### FIGURES

Figure 2-1: Axis Frames .....	6
Figure 2-2: Satellite Dimensions.....	9
Figure 2-3: Satellite Rotational Motion Model.....	10
Figure 2-4: Gravity Gradient Torque .....	12
Figure 2-5: Sun Light Position Vector with respect to Satellite .....	14
Figure 2-6: Solar Radiation Torque .....	15
Figure 2-7: Magnetic Field Torque.....	16
Figure 2-8: Aerodynamic Torques.....	17
Figure 2-9: Disturbances Model.....	18
Figure 2-10: Total Disturbance Torques.....	19
Figure 2-11: Reference Models.....	20
Figure 2-12: The Keplerian Elements [10] .....	21
Figure 2-13: The Keplerian Elements in plane [10].....	21
Figure 2-14: Satellite Position in Spherical Coordinates .....	29
Figure 2-15: Orbit Propagator Model Block Diagram.....	30
Figure 2-16: Sun Position Model Block Diagram.....	32
Figure 2-17: Magnitude of the Earth's Magnetic Field [14].....	33
Figure 2-18: The Earth's Magnetic Field from IGRF Model .....	36
Figure 2-19: Earth Magnetic Field Model Block Diagram.....	36
Figure 2-20: Rate Gyro Turn on Bias Error Model.....	38
Figure 2-21: Bias Stability Error Model .....	39
Figure 2-22: The Allan Variance Result for The Rate Gyros Data [14].....	40
Figure 2-23: Random Walk Error Model.....	41
Figure 2-24: Scale Factor Error Model .....	42
Figure 2-25: Rate Gyro Measurement Model Block Diagram .....	42
Figure 2-26: Sun Sensor Measurement Model Block Diagram.....	44
Figure 2-27: Magnetometer Measurement Model Block Diagram.....	46

Figure 2-28: Star Sensor Measurement Model Block Diagram.....	47
Figure 3-1: Satellite Attitude Determination Block Diagram .....	61
Figure 3-2: Mode-1 Real and Estimated Angular Rates .....	68
Figure 3-3: Mode-1 Std. Dev. and Mean of the Angular Rate Estimation Error.....	68
Figure 3-4: Mode-2 Real and Estimated Angular Rates .....	74
Figure 3-5: Mode-2 Real and Estimated Quaternions.....	74
Figure 3-6: Mode-2 Real and Estimated RPY Angles .....	75
Figure 3-7: Mode-2 Mean of the Angular Rate Estimation Error.....	76
Figure 3-8: Mode-2 Standard Deviation of the Angular Rate Estimation Error.....	76
Figure 3-9: Mode-3 Real and Estimated Angular Rates .....	78
Figure 3-10: Mode-3 Real and Estimated Quaternions.....	78
Figure 3-11: Mode-3 Real and Estimated RPY Angles .....	79
Figure 3-12: Mode-3 Mean of the Angular Rates Estimation Error .....	80
Figure 3-13: Mode-3 Standard Deviation of the Angular Rates Estimation Error ....	80
Figure 3-14: Mode-3 Mean of the Quaternions Estimation Error.....	81
Figure 3-15: Mode-3 Standard Deviation of the Quaternions Estimation Error.....	81
Figure 3-16: Mode-3 Mean of the RPY Angles Estimation Error .....	82
Figure 3-17: Mode-3 Standard Deviation of the RPY Angles Estimation Error .....	82
Figure 3-18: Mode-4 Real and Estimated Angular Rates .....	84
Figure 3-19: Mode-4 Real and Estimated Quaternions.....	84
Figure 3-20: Mode-4 Real and Estimated RPY Angles .....	85
Figure 3-21: Mode-4 Mean of the Angular Rates Estimation Error .....	86
Figure 3-22: Mode-4 Standard Deviation of the Angular Rates Estimation Error ....	86
Figure 3-23: Mode-4 Mean of the Quaternions Estimation Error.....	87
Figure 3-24: Mode-4 Standard Deviation of the Quaternions Estimation Error.....	87
Figure 3-25: Mode-4 Mean of the RPY Estimation Error .....	88
Figure 3-26: Mode-4 Standard Deviation of the RPY Estimation Error .....	88
Figure 3-27: Mode-5 Real and Estimated Angular Rates .....	92
Figure 3-28: Mode-5 Real and Estimated Quaternions.....	93
Figure 3-29: Mode-5 Real and Estimated RPY Angles .....	93
Figure 3-30: Mode-5 Mean of the Angular Rates Estimation Error .....	94
Figure 3-31: Mode-5 Standard Deviation of the Angular Rates Estimation Error ....	94

Figure 3-32: Mode-5 Mean of the Quaternions Estimation Error.....	95
Figure 3-33: Mode-5 Standard Deviation of the Quaternions Estimation Error.....	95
Figure 3-34: Mode-5 Mean of the RPY Estimation Error .....	96
Figure 3-35: Mode-5 Standard Deviation of the RPY Estimation Error .....	96
Figure 3-36: Mode-6 Real and Estimated Angular Rates .....	98
Figure 3-37: Mode-6 Real and Estimated Quaternions.....	98
Figure 3-38: Mode-6 Real and Estimated RPY Angles .....	99
Figure 3-39: Mode-6 Mean of the Angular Rates Estimation Error .....	100
Figure 3-40: Mode-6 Standard Deviation of the Angular Rates Estimation Error .	100
Figure 3-41: Mode-6 Mean of the Quaternions Estimation Error.....	101
Figure 3-42: Mode-6 Standard Deviation of the Quaternions Estimation Error.....	101
Figure 3-43: Mode-6 Mean of the RPY Angles Estimation Error .....	102
Figure 3-44: Mode-6 Standard Deviation of the RPY Angles Estimation Error .....	102
Figure 3-45: Sensor Flags and Selected ADS Mode.....	105
Figure 3-46: Mode Selection Scenario-1 .....	106
Figure 3-47: Mode Selection Scenario-2 .....	106
Figure 3-48: Attitude Estimation Performance For Several Successive Maneuvers	107
Figure 4-1: Axis Frames used for SACoTS .....	110
Figure 4-2: SACoTS Rotational Motion Model .....	112
Figure 4-3: Block Diagram of the Accelerometer Measurement Model .....	115
Figure 4-4: SACoTS Attitude Determination System Block Diagram.....	117
Figure 4-5: Mode-s1 Real and Estimated Angular Rates.....	125
Figure 4-6: Mode-s1 Real and Estimated Quaternions .....	126
Figure 4-7: Mode-s1 Real and Estimated RPY Angles .....	126
Figure 4-8: Mode-s1 Mean of the Angular Rate Estimation Error .....	127
Figure 4-9: Mode-s1 Standard Deviation of the Angular Rate Estimation Error ....	128
Figure 4-10: Mode-s1 Mean of the Quaternions Estimation Error .....	128
Figure 4-11: Mode-s1 Standard Deviation of the Quaternions Estimation Error ....	129
Figure 4-12: Mode-s1 Mean of the RPY Angles Estimation Error .....	129
Figure 4-13: Mode-s1 Standard Deviation of the RPY Angles Estimation Error ...	130
Figure 4-14: Mode-s2 Real and Estimated Angular Rates.....	133
Figure 4-15: Mode-s2 Real and Estimated Quaternions .....	133

Figure 4-16: Mode-s2 Real and Estimated RPY Angles .....	134
Figure 4-17: Mode-s2 Mean of the Angular Rate Estimation Error .....	135
Figure 4-18: Mode-s2 Standard Deviation of the Angular Rate Estimation Error ..	135
Figure 4-19: Mode-s2 Mean of the Quaternions Estimation Error .....	136
Figure 4-20: Mode-s2 Standard Deviation of the Quaternions Estimation Error ...	136
Figure 4-21: Mode-s2 Mean of the RPY Angles Estimation Error .....	137
Figure 4-22: Mode-s2 Standard Deviation of the RPY Angles Estimation Error ...	137

# CHAPTER 1

## INTRODUCTION

There has been a great progress in the development of the satellite attitude determination and control systems during the past few decades. Especially the subject of the Earth observation by using low Earth orbit satellites and satellite constellations has increased the importance of the satellite attitude determination and control systems for both civil and military applications. The increasing demands for high resolution missions (and decreasing swath widths in such) require very accurate and stable attitude determination and control system to keep the satellite at a specific orientation with respect to a defined reference frame. In order to obtain such a successful attitude control, this control system must be fed with an accurate and robust attitude determination system. For this reasons, this thesis addresses satellite attitude determination problems and contains the studies of the Kalman filter based attitude determination algorithms.

The Kalman filter is the most widely used method to incorporate multiple sensors for navigation and attitude determination of aerospace vehicles. The advances in digital computing made the usage of this filter practical and its applications has gone along way since the original work is published by R.E. Kalman in 1960 [1]. Kalman filter is applied in Apollo program and subsequent spacecraft attitude determination problems [2]. Kalman filters are used also to determine the attitude and gyro bias values by measuring angular rates directly from strapdown 3-axis gyros [2]. Psiaki et.al. used Kalman filter to estimate the attitude, attitude rates and constant disturbance torques for a 3-axis stabilized spacecraft [3]. The problem of filtering and estimation using nonlinear system and/or sensor measurement models is inherently more difficult than for the case of linear models. The Extended Kalman Filter (EKF) gives a good estimation results for the nonlinear systems where the first

order Taylor series linearization sufficiently approximates the nonlinear motion characteristics [4]. However, the estimation performance and accuracy of the EKF will not be adequate for the high order systems and this may cause the instability and divergence problem on estimation. The possible method to overcome these problems may lead the calculation errors because of their high computational burden. Therefore, the standard EKF has stayed the most popular filter for nonlinear estimation to this day. Other design approaches are investigated only when high performance is required [4]. For instance, Unscented Kalman Filter (UKF) that has been developed by Julier, Uhlman and Durrant-White [5]. The UKF may be applied in order to achieve more accurate estimation performance compared to EKF, therefore UKF applications can be experienced for the ground based satellite attitude control test setup. The reason to establish and use these test setups is to demonstrate the performance of the hardware and algorithms in ground and mitigates the risk to lose the high-cost satellite system in orbit. However, it is difficult to experimentally simulate satellite dynamics in ground laboratory because of the influences of gravity and friction. An air bearing provides a nearly torque-free environment. For this reason it is the preferred technology for ground-based research in satellite dynamics and control. Generally, spherical air bearings are one of the most common test setups used in spacecraft attitude dynamics, attitude determination and control researches because they provide three degrees of rotational freedom. Several satellite ground based test setups are investigated in order to determine the differences and the similarities between the dynamics and attitude determination systems of a satellite and a test setup. The first test setups examined are TASS (Three Axis Satellite Simulator) and TASS-2 which belong to Naval Postgraduate School (Monterey, California) [6]. The second test setups belong to Virginia Polytechnic Institute and State University (Blacksburg, Virginia, USA) and they called as WHORL-1 and WHORL-2. WHORL-1 is a tabletop style spherical air bearing and WHORL-2 is a dumbbell style spherical air bearing [7]. Other examples for test setups are IACS-1 (Integrated Attitude Control System) and IACS-2 that appertain to Georgia Institute of Technology (Atlanta, USA) [8][9]. The details about these investigated satellite test setup are given in the Appendix D. These foregoing examples are given in order to show the wide usage areas of the Kalman filter in aerospace fields.

The objective of this thesis is twofold. The first one is to generate Kalman filter based attitude determination system simulation for satellites including all required subcomponents such as satellite motion model, environmental disturbances model, sensor measurements model and attitude determination algorithms. The second one is to implement the algorithms for a ground based satellite control test setup. The original contributions in this thesis are developing a multimode attitude determination system for a hypothetical LEO satellite, which contains the sensor availability flag logic and comparing the performance of these different modes by applying Monte Carlo simulations. An additional contribution is to design a sufficiently accurate attitude determination system for satellite attitude control test setups by using different type of estimation algorithms instead to use additional reference sensor.

This thesis consists of three main chapters. Chapter 2 gives all the components that are required for the design of a satellite attitude determination system such as satellite motion model, disturbances torques model and sensor measurement models. The details of the several coordinate systems used in order to define the satellite's motion and attitude parameterization, the definition and notations used in this thesis are given in Appendix A.

Chapter 3 presents the details of the Kalman filter theory. EKF algorithms are formulated for different stages of mission phases such as angular rate estimation during detumbling phase of the satellite, coarse and accurate full state estimation during regular orbital phase. The performance of these different modes are investigated and compared at the end of this chapter.

Chapter 4 presents the Kalman filter based attitude determination system prepared for satellite attitude control test setup. Here, the capability of the sensor suite used is different then a usual satellite. The performance comparison between two different filter types, EKF and UKF, is given in this chapter. This chapter and related

Appendix D contain the general information about the satellite test setups existing on the some institutes and universities.

Finally, Chapter 5 summarizes the conclusions of all the studies performed in this thesis and provides recommendations for the future research.

## CHAPTER 2

### SATELLITE SIMULATION MODEL

This section presents the components of the simulation code developed for the design of a satellite attitude determination system. First the satellite motion model is given, and then the disturbance torques that act on satellites are modeled. Next, the satellite orbit propagator model, sun position model and Earth magnetic field model are given. These are used for sensors measurements. In addition sensor models also are presented in detail considering all type of the measurement noises. Then, satellite attitude determination system structure and the Kalman filter's details are explained. Finally the results obtained from the simulations of the attitude determination algorithms are presented.

#### 2.1 Satellite Rotational Motion Model

A mathematical model of the satellite attitude motion is derived in this section. This model can be considered into two sections: one is the *dynamics* of the satellite which describes the behavior under the effects of the external forces; the other is the *kinematics* of the satellite which defines the relation between the Body frame and the Orbit frame, the attitude of the satellite.

##### 2.1.1 Dynamic Equations

The dynamics of the satellite is given by Euler's equations of motion. In order to derive to dynamic equations, a rigid body in a circular orbit is considered. At the following

Figure 2-1, the ECI frame, the ORB frame and the BODY frame for an orbiting satellite are illustrated [10].

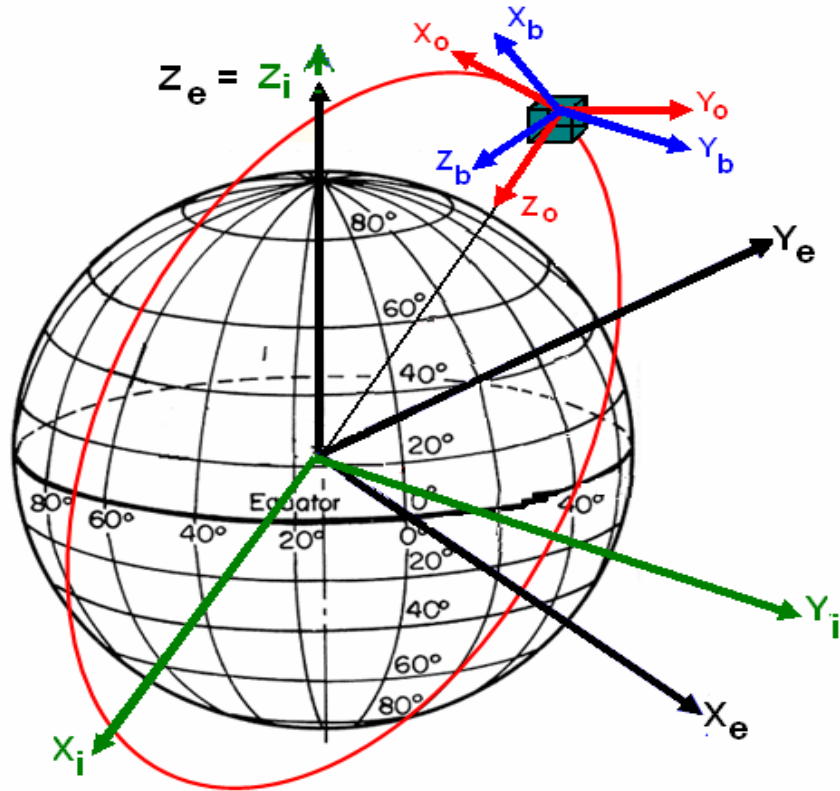


Figure 2-1: Axis Frames

The rotational equation of motion of a rigid body with an angular momentum  $\vec{H}$  in a circular orbit is given by:

$$\left. \frac{d\vec{H}}{dt} \right|_I = \left. \frac{d\vec{H}}{dt} \right|_B + \vec{\omega}_{IB}^B \times \vec{H}_B = \tau^B \quad (2.1.1)$$

as  $\vec{H} = I\vec{\omega}$  and  $\dot{I} = 0$ , the following equation is obtained:

$$I\dot{\vec{\omega}}_{IB}^B + \vec{\omega}_{IB}^B \times I\vec{\omega}_{IB}^B = \tau^B \quad (2.1.2)$$

where  $I$  is the inertial moments matrix,  $\vec{\omega}_{IB}^B$  is the angular velocity of the BODY frame relative to the ECI frame expressed in the BODY frame and  $\tau^B$  is the total torque acting on the satellite.

The dynamics of the satellite can be reformulated by using the diad notation as:

$$\dot{\omega}_{IB}^B = I^{-1}(-\tilde{\omega}_{IB}^B I \omega_{IB}^B + \tau^B) \quad (2.1.3)$$

where;

$$\tilde{\omega}_{IB}^B = \begin{bmatrix} 0 & -\omega_{IBz}^B & \omega_{IBy}^B \\ \omega_{IBz}^B & 0 & -\omega_{IBx}^B \\ -\omega_{IBy}^B & \omega_{IBx}^B & 0 \end{bmatrix} \quad (2.1.4)$$

The torques,  $\tau^B$ , acting on the satellite can be divided into disturbances and control torques [11]:

$$\tau^B = \tau_{dist} + \tau_{ctrl} = \tau_{gg} + \tau_{sol} + \tau_{mag} + \tau_{aero} + \tau_{ctrl} \quad (2.1.5)$$

1. Disturbances Torques
  - a. Gravity Gradient Torque
  - b. Solar Radiation Torque
  - c. Magnetic Field Torque
  - d. Aerodynamics Torque
2. Control Torques

The detailed explanations about the disturbances torques are given in the Section 2.2.

### 2.1.2 Kinematics Equations

The kinematics propagation of the satellite is done by using the quaternion representation. The following differential equation is given for the formulation of the satellite's attitude [10]:

$$\dot{q} = \frac{1}{2} \Omega_{OB}^B q \quad (2.1.6)$$

where;

$$\Omega = \begin{bmatrix} 0 & \omega_{OBz}^B & -\omega_{OB_y}^B & \omega_{OB_x}^B \\ -\omega_{OBz}^B & 0 & \omega_{OB_x}^B & \omega_{OB_y}^B \\ \omega_{OB_y}^B & -\omega_{OB_x}^B & 0 & \omega_{OBz}^B \\ -\omega_{OB_x}^B & -\omega_{OB_y}^B & -\omega_{OBz}^B & 0 \end{bmatrix} \quad (2.1.7)$$

here,  $\omega_{OB}^B$  is the angular velocities from BODY frame with respect to the ORBIT frame, expressed in BODY frame.

The body angular rates referenced to the orbit following coordinates can be obtained from the inertially referenced body rates as follows:

$$\omega_{OB}^B = \omega_{IB}^B - C_o^B \omega_{Io}^O \quad (2.1.8)$$

where  $C_o^B$  is the DCM from orbital frame to body frame, and  $\omega_{Io}^O = [0 \quad -\omega_o \quad 0]^T$  is the known angular velocity of the Orbit frame relative to the ECI frame, expressed in Orbit frame. This velocity depends on the altitude of the orbit, and can be calculated according to  $\omega_o = \sqrt{GM_e / R^3}$  where  $G$  is the gravitational constant of the Earth,  $M_e$  is the mass of the Earth and  $R$  is the distance from the centre of the Earth to the satellite. Finally the angular body rates obtained can be written as:

$$\omega_{OB}^B = \begin{bmatrix} \omega_{ox} \\ \omega_{oy} \\ \omega_{oz} \end{bmatrix}_O = \begin{bmatrix} \omega_x \\ \omega_y \\ \omega_z \end{bmatrix}_B - C_O^B \begin{bmatrix} 0 \\ -\omega_O \\ 0 \end{bmatrix} \quad (2.1.9)$$

### 2.1.3 Satellite Specifications

The hypothetical satellite model used in this report has a shape of rectangular prism with the dimensions HxWxL = 2.0x1.7x1.5 meters and weight of 200 kg. A rough calculation of the inertial moments is done with the assumption that the satellite structure has a uniform mass distribution. The inertia matrix then is:

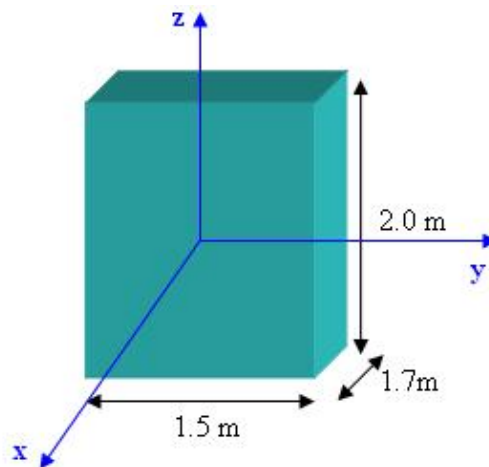


**Figure 2-2: Satellite Dimensions**

*mass = 200 kg*

$$I = \begin{bmatrix} 104.17 & 0 & 0 \\ 0 & 114.83 & 0 \\ 0 & 0 & 85.67 \end{bmatrix} \text{ kg.m}^2$$

The orbital parameters selected for this virtual satellite are given in the following table:

**Table 2-1: Orbital Parameters of the Hypothetical Satellite**

Inclination( $i$ ):	$97.8^\circ$
Eccentricity( $e$ ):	$0^\circ$ ( <i>circular orbit</i> )
Altitude( $h$ ):	$650 \text{ km}$
Semi Major Axis( $a$ ):	$R_{Earth} + h = (6378 + 650) \text{ km}$

The satellite dynamics module that defines the satellite rotational motion model containing dynamics and kinematics is prepared by Matlab/SIMULINK. This module with its inputs and outputs is given in the following Figure 2-3.

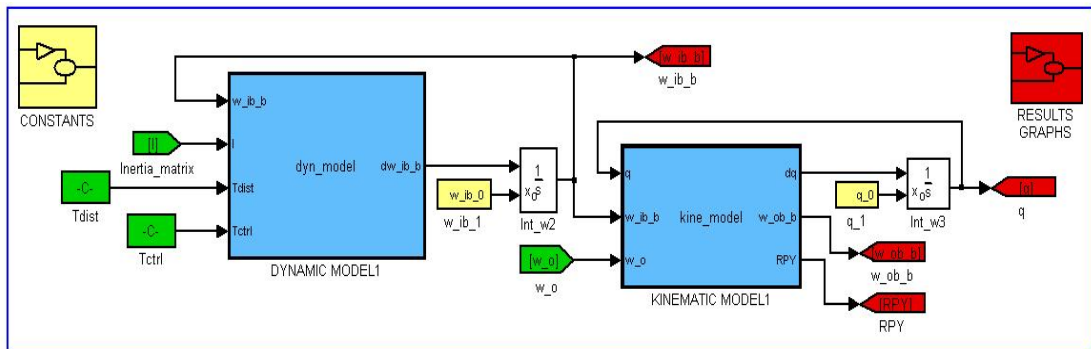


**Figure 2-3: Satellite Rotational Motion Model**

## 2.2 Disturbances Torques

In a Low Earth orbit, the spacecraft is exposed to several external torques caused by the space environment conditions. These disturbance torques arise from the gravity gradient force, solar radiation pressure, magnetic field and aerodynamic forces. The

magnitude of these torques depends on the spacecraft's orbital altitude, geometry, orientation, and mass properties. The most significant of these are gravity gradient torques. Depending on the satellite dimensions, the solar radiation, and magnetic field torques can be also taken into consideration on the model, but generally aerodynamic forces are not a design issue for most Low Earth Orbit (LEO) satellites above an altitude of 250 km [11].

The detailed descriptions and the calculation methods for the torques mentioned above are given in the following subchapters. The figures that show the magnitude of these torques and the block diagram of the disturbance model created for simulations also are included this following subchapters.

### 2.2.1 Gravity Gradient Torque

The Gravity Gradient torque is the one of the largest torque source that affects a LEO satellite; therefore, the solution of most satellite dynamics and control problems requires a consideration of this gravitational torque source. This disturbance, created by the distance between the opposite ends of the spacecraft, makes a small difference in the force acting on those end points. As a result, a torque occurs about the spacecraft's center of mass. This Gravity Gradient torque is expressed in dyadic form as [12]:

$$\tau_{gg} = 3.\omega_o^2.\vec{k}_o \times I.\vec{k}_o \quad (2.2.1)$$

where;  $\omega_o$  is the orbital mean motion and  $\vec{k}_o$  is the unit vector along the Z axis of the ORB frame ( $\vec{Z}_o$ ) expressed as:

$$\vec{k}_o = C_{13}.\vec{i}_B + C_{23}.\vec{j}_B + C_{33}.\vec{k}_B \quad (2.2.2)$$

here,  $\{ \vec{i}_B, \vec{j}_B, \vec{k}_B \}$  are the unit vectors of the BODY frame.

Finally the Gravity Gradient torque can be written in dyadic form as follows:

$$\tau_{gg} = 3.\omega_o^2.\tilde{k}_o.I.k_o = 3.\omega_o^2.\begin{bmatrix} 0 & -C_{33} & C_{23} \\ C_{33} & 0 & -C_{13} \\ -C_{23} & C_{13} & 0 \end{bmatrix}.I.\begin{bmatrix} C_{13} \\ C_{23} \\ C_{33} \end{bmatrix} \quad (2.2.3)$$

where  $C \equiv C_o^B$  is DCM from ORB frame to BODY frame.

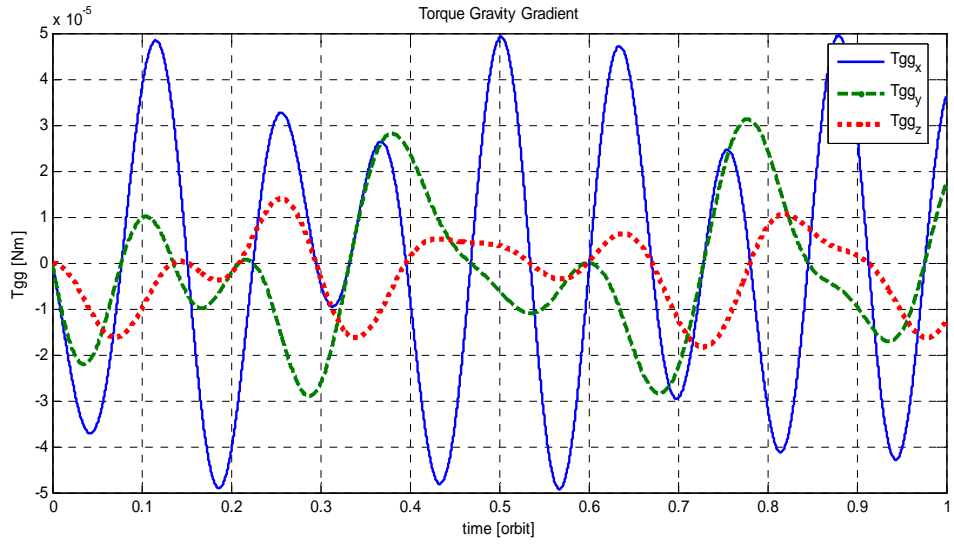


**Figure 2-4: Gravity Gradient Torque**

The above Figure 2-4 shows the values of the Gravity Gradient torque acting on the satellite during the 1 orbital period navigation. As seen on the Figure 2-4, the magnitude of this torque is of the order  $10^{-5} Nm$ .

### 2.2.2 Solar Radiation Torque

The distance between the satellite's center of pressure and its center of gravity causes the solar radiation pressure torque. While solar radiation reflected off by the sun, the satellite will create a torque about its center of gravity. On an Earth orbiting satellite

these disturbances are cyclic over an orbital period and are a function of the spacecraft's reflectivity.

The Solar Radiation torque can be calculated using the following equation [11]:

$$\tau_{sol} = F (C_{ps} - C_g) \quad (2.2.4)$$

where;

$$F = \frac{F_s}{C} A_s (1 + q) \cos(i) \quad (2.2.5)$$

and,

$F_s$  = solar constant (1358 W/m<sup>2</sup>)

$C$  = speed of light, (3.0E8 m/s)

$A_s$  = surface area, (0.6993 m<sup>2</sup>)

$C_{ps}$  = center of solar pressure

$C_g$  = center of gravity

$q$  = reflectance factor, (0.6 worst case)

$i$  = angle of incidence of the sun (degrees)

In order to calculate the solar radiation torque for the virtual satellite model given in the foregoing Section 2.1.3, formula are governed by taking into consideration the sun light position vector with respect to satellite.

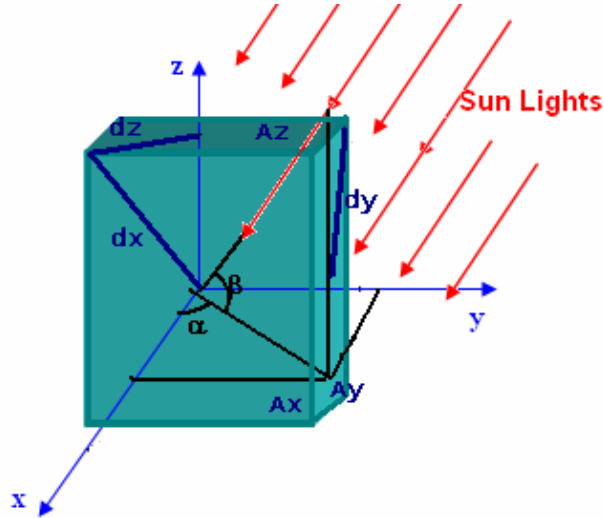


**Figure 2-5: Sun Light Position Vector with respect to Satellite**

The sun lights will create solar torques depending on the angle of incidence of the related surface of the satellite. The position angles  $\alpha$  and  $\beta$  can be calculated by using the position vector of the sun with respect to the spacecraft  $v_{S/SC} = [S_x \ S_y \ S_z]^T$ . This sun position information will be obtained by using the Ephemeris reference model (See Section 2.3.1):

$$\alpha = \tan^{-1}(S_y / S_x) \quad (2.2.6)$$

$$\beta = \sin^{-1}(S_z) \quad (2.2.7)$$

$$\begin{aligned} \tau_{sol\_x} &= \frac{F_s}{C} A_x (1+q) \cos(\alpha) \ dx \\ \tau_{sol\_y} &= \frac{F_s}{C} A_y (1+q) \sin(\alpha) \ dy \\ \tau_{sol\_z} &= \frac{F_s}{C} A_z (1+q) \sin(\beta) \ dz \end{aligned} \quad (2.2.8)$$

where,  $A_x, A_y, A_z$  are the surface areas and  $dx, dy, dz$  are the diagonal distances of these surfaces. These diagonal distances are taken as the distance between center of gravity and center solar pressure for the purpose of simulating the worst conditions.

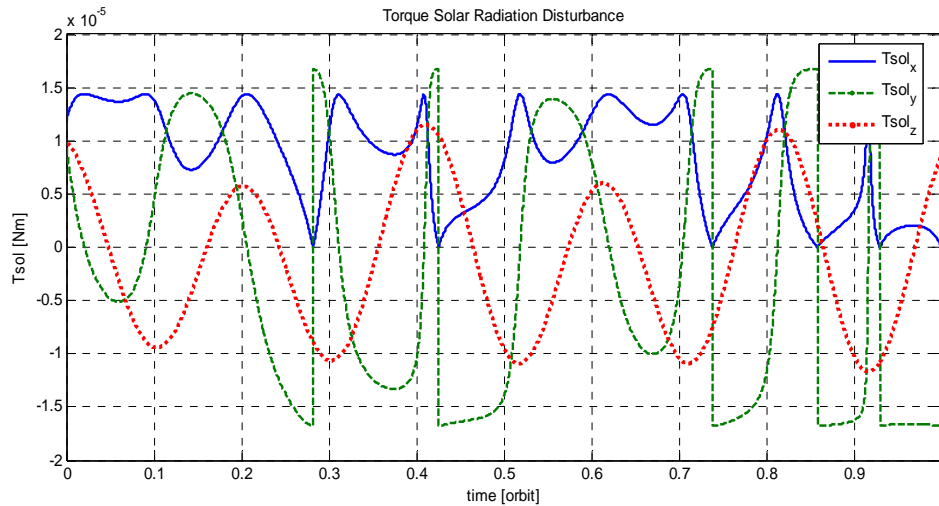


**Figure 2-6: Solar Radiation Torque**

Solar Radiation torque acting on the hypothetical satellite is given in the above Figure 2-6 and its magnitude is of the order  $10^{-5} Nm$  which is similar to the calculated Gravity Gradient torque magnitudes.

### 2.2.3 Magnetic Field Torque

The interactions between the spacecraft residual magnetic dipole and the Earth's magnetic field create Magnetic Field torque. For the preliminary design a  $1 Am^2$  residual dipole is selected as a good approximation for a small satellite.

The calculations were made using the following equation [11]:

$$\tau_{mag} = D.B = D.\frac{2M}{R^3} \quad (2.2.9)$$

where;

D = residual dipole (amp.m<sup>2</sup>)

B = Earth magnetic field (Tesla)

M = magnetic moment of the Earth, (7.96E15 tesla.m<sup>3</sup>)

R = radius of orbit (m)

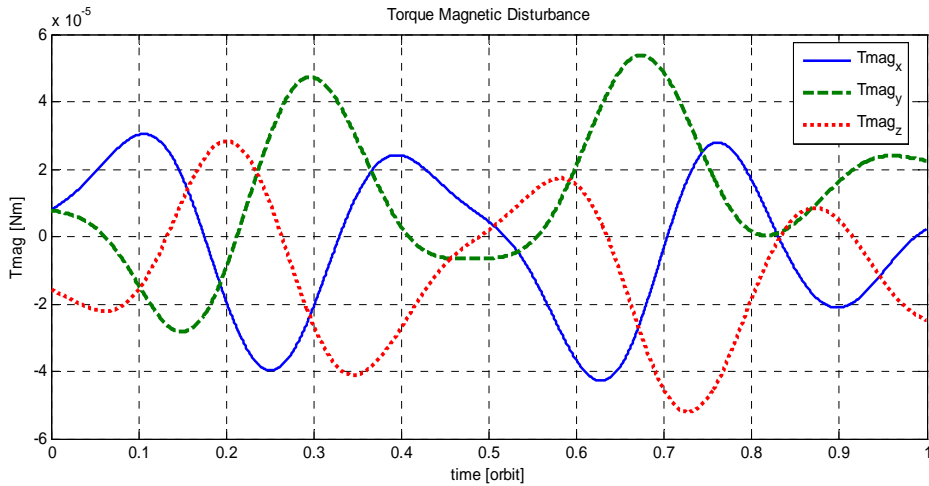


**Figure 2-7: Magnetic Field Torque**

Earth magnetic field value will be obtained by using Magnetic Model, presented in the Section 2.3.2. Magnetic Field torque acting on a satellite with  $1 \text{ A.m}^2$  residual dipole at the orbital conditions stated in Table 2-1 is given in the Figure 2-7 and the magnitude of this torque is about  $10^{-5} \text{ Nm}$ , similar to the Gravity Gradient and Solar Radiation torques.

#### 2.2.4 Aerodynamics Torque

Aerodynamics torque is the results of the atmospheric drag acting on the satellite. Especially for LEO satellites this torques can be quite significant (with magnitudes up to  $10^{-4} \text{ Nm}$ ), but at altitudes above 600 km these torques are negligible.

This torques is difficult to calculate because parameters such as cross sectional area can change rapidly with time depending on the attitude of the satellite. And also, atmospheric density varies significantly with solar activity. Torque calculations were made using the following equations [11]:

$$\tau_{aero} = F (C_{pa} - C_g) \quad (2.2.10)$$

where;

$$F = 0.5 (\rho \cdot C_d \cdot A \cdot V^2) \quad (2.2.11)$$

and;

$C_d$  = coefficient of drag

$A$  = cross-sectional area (m<sup>2</sup>)

$V$  = spacecraft velocity (m/s)

$C_{pa}$  = center of aerodynamic pressure

$C_g$  = center of gravity

$\rho$  = atmospheric density (kg/m<sup>3</sup>)

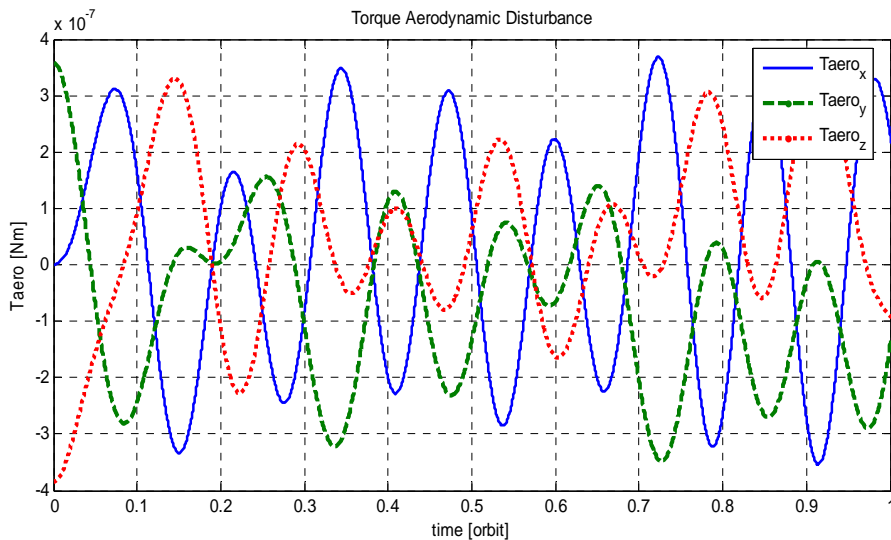


**Figure 2-8: Aerodynamic Torques**

Aerodynamics torque calculated for 1 orbital period for hypothetical satellite's orbital parameters defined in Table 2-1 is given in the following Figure 2-8. Magnitude obtained for this torque is of the order  $10^{-7} Nm$  which is 2 orders of magnitude smaller than the other disturbances torques. As mentioned above, according to the results obtained it can be stated that Aerodynamic torque is the smaller torque acting to the satellite when its altitude is about 600 km -700 km.

### 2.2.5 Total Disturbances Torque

The model including all of the disturbance torques is generated in order to simulate the space environment of the LEO satellite. The block diagram of this model is given in the following Figure 2-9.

The total disturbances torques acting on the hypothetical satellite is shown in Figure 2-10.

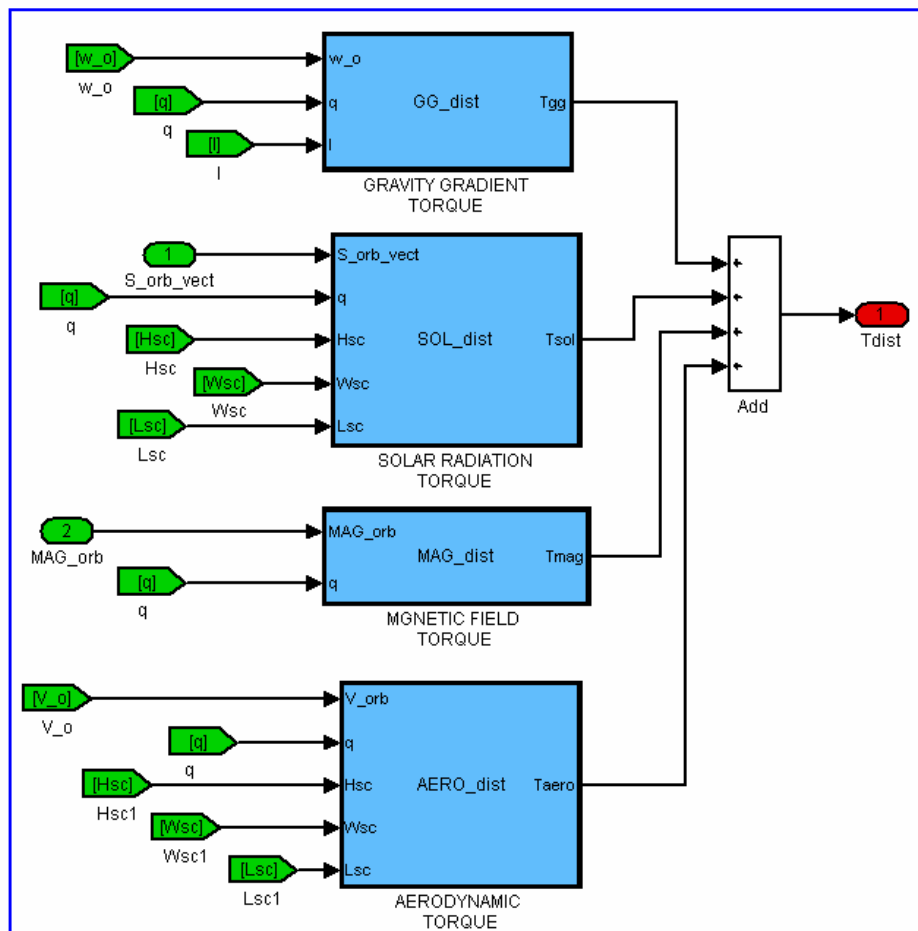
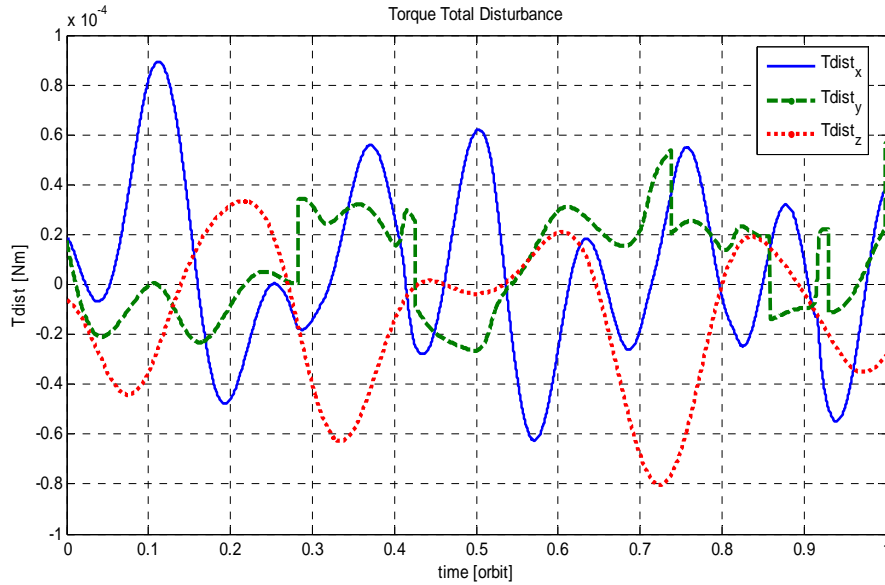


Figure 2-9: Disturbances Model



**Figure 2-10: Total Disturbance Torques**

It may be observed from the above results that the most dominant torques are the Gravity Gradient and Magnetic Field torques. It is also seen that for altitude around 600-700 km, the aerodynamics torques has no significance. As a result, the total magnitude of the disturbances torques is of the order  $10^{-4} Nm$ .

### 2.3 Reference Models

In order to determine the attitude of the satellite from the reference sensors, it is needed to know the satellite's orbit and its position in orbit. It is necessary to know the rotational relationship between the ECEF frame, in which the Earth magnetic field vector is given, the ECI frame, in which the Sun position vector is given and the ORB frame in which the measurements are taken by the reference sensors attached to the body frame. Therefore an *Orbit Propagator Model* is constructed to obtain the attitude relations mentioned above. Furthermore, reference sensors such as sun sensors and magnetometers require reference models to compare the measured data with. For the purpose of defining the measurements of the sensors *Sun Position Model* and *Earth Magnetic Field Model* are also created. The block diagram that shows the input and output relations between these models are given in Figure 2-11.

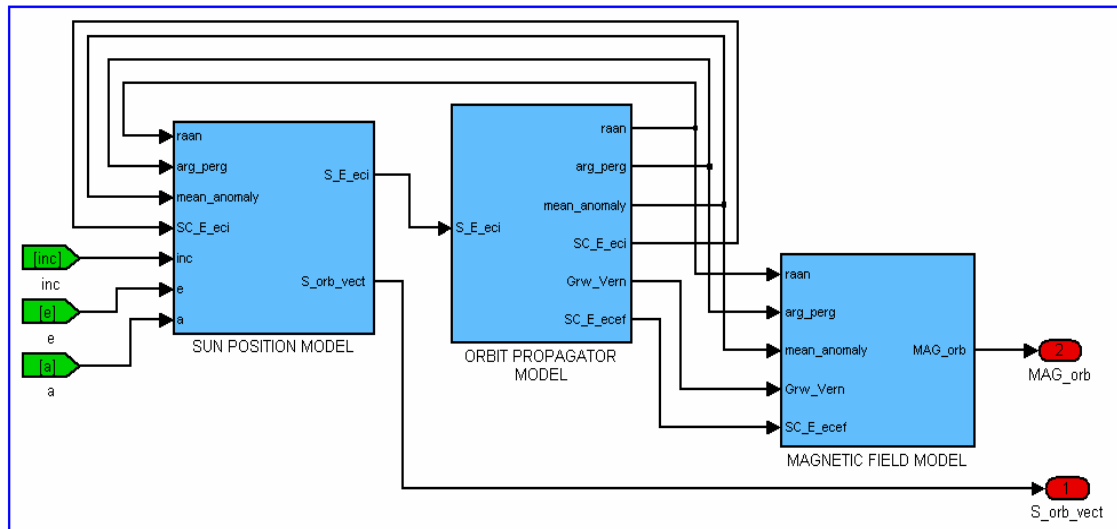


**Figure 2-11: Reference Models**

In the following subchapters the detailed explanations about these reference models are given.

### 2.3.1 Orbit Propagator Model

The physical laws describing the motion of planets were first described by Johann Kepler. Kepler's three laws state that:

1. The orbit of each planet is an ellipse, with the Sun at one of the foci.
2. The line joining the planet to the Sun sweeps out equal areas in equal times.
3. The square of the period of a planet is proportional to the cube of its mean distance from the Sun.

Kepler's laws are the basis for the Keplerian elements, called also orbital elements, which are used in predicting a satellite's orbit and position. The Earth is at one focus of the ellipse. The two foci coincide with the center in the case of the circular orbit and as a result, the Earth takes its place at the center of the ellipse [10].

The Orbit Propagator Model used in the simulation is given in Keplerian elements. See Figure 2-12 and Figure 2-13 for visual description of all the Keplerian elements:

1. Orbital Inclination
2. Right Ascension of Ascending Node (R.A.A.N.)
3. Argument of Perigee
4. Eccentricity
5. Mean Motion
6. Mean Anomaly

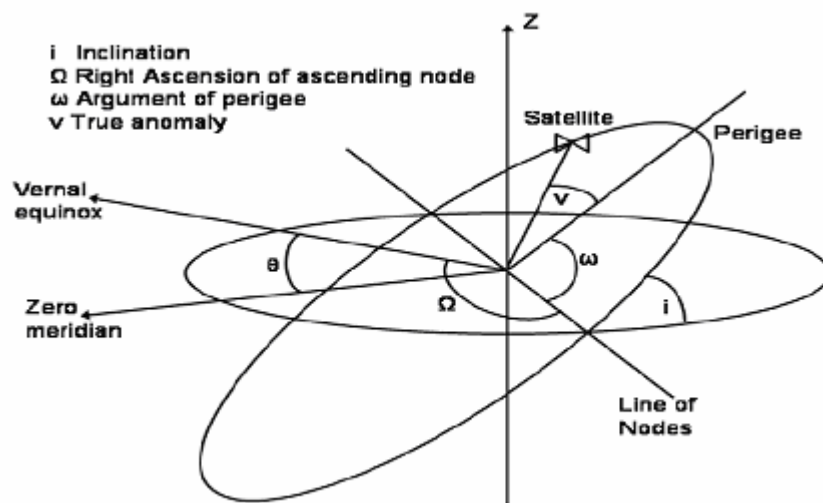


Figure 2-12: The Keplerian Elements [10]

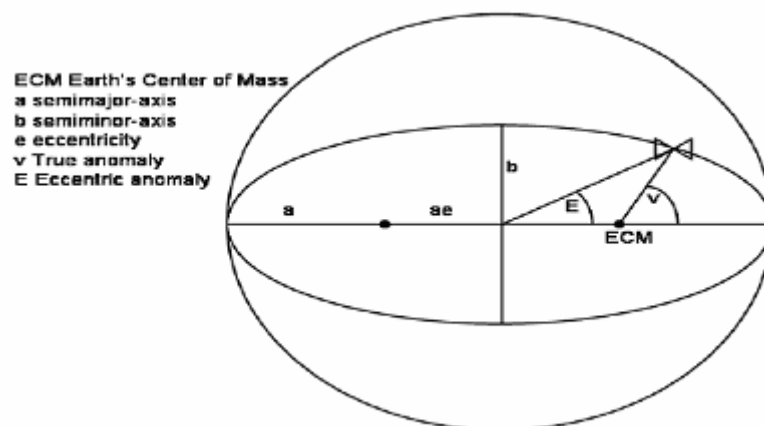


Figure 2-13: The Keplerian Elements in plane [10]

These elements describe the position of the satellite at a specific time. The most widely used format for this time is called epoch (Julian Date) that gives the year and day of the year as a decimal number. Based on this time, the ascension of the zero meridians ( $\theta$ ), can also be calculated. Using Eq. (A.3.3), with  $\lambda = \theta$ , the rotation between ECI and ECEF reference frame given by:

$$C_E^I = C_{z,\theta} = \begin{bmatrix} \cos \theta & \sin \theta & 0 \\ -\sin \theta & \cos \theta & 0 \\ 0 & 0 & 1 \end{bmatrix} \quad (2.3.1)$$

The following four Keplerian elements specify the orientation of the orbital plane, the orientation of the orbit ellipse in the orbital plane, and the shape of the orbit ellipse [10]:

***Orbital Inclination (i):***

The inclination is the angle between the orbital and equatorial plane. By convention, inclination is a number between 0 and 180 degrees. Orbits with inclination near 0 degrees are called equatorial orbits and orbits with inclination near 90 degrees are called polar. The intersection of the equatorial plane and the orbital plane is a line which is called the line of nodes. The line of nodes is more thoroughly described below.

***Right Ascension of Ascending Node ( $\Omega$ ):***

The line of nodes intersects the equatorial plane two places: One of them the satellite passes from south to north, this is called the ascending node and the other node where the satellite passes from north to south is called the descending node. The angle between the ascending node and the vernal equinox is called the right ascension of ascending node. By convention, the right ascension of ascending node is

between 0 and 360 degrees. The combination of the right ascension of ascending node and the inclination defines the orbital plane in which the elliptic orbit lies.

***Argument of Perigee ( $\omega$ ):***

In the ellipse, the closest point to the focus point, in which the earth lies, is called *perigee*, and the farthest point from the earth is called *apogee*. The angle between the line from perigee through the center of the earth to the apogee and the line of nodes is the argument of perigee. This angle is defined as the angle from the ascending node and by convention it is between 0 and 360 degrees.

***Eccentricity ( $e$ ):***

The eccentricity is given as

$$e = \sqrt{1 - \frac{b^2}{a^2}} \quad (2.3.2)$$

where  $a$  is the semimajor-axis and  $b$  is the semiminor-axis. The semimajor-axis is half the distance between the apogee and the perigee, and semiminor-axis half the length between the edges perpendicular to  $a$ . For an ellipse,  $e$  is between 0 and 1. For a perfect circle  $a = b$  and thus  $e = 0$ .

The following Keplerian elements is time varying and specify the position of the satellite in orbit using the previous four elements describing above [4]

***Mean Motion ( $n$ ):***

The mean motion is the average angular velocity describes the size of the ellipse. It is related to the semimajor-axis using Kepler's third law:

$$n = \sqrt{\frac{\mu_e}{a^3}} \quad (2.3.3)$$

where  $\mu_e = G.M_e$ ,  $G$  is the Earth's gravitational constant and  $M_e$  is the mass of the Earth.

**Mean Anomaly (M):**

Mean Anomaly defines the position of the satellite in the ellipse. It is an angle that marches uniformly in time from 0 to 360 degrees during one revolution. It is defined to be 0 degrees at perigee and 180 degrees at apogee.

There is an important point to note that in a non-circular ellipse, this angle does not give the direction towards the satellite except at perigee and apogee. This is because satellite does not have a constant angular velocity.

The different anomalies used are shown in Figure 2-13. The direction from the earth center towards the satellite is called *true anomaly* ( $v$ ) and the direction from the center of the ellipse towards the point on a circle is called *eccentric anomaly* ( $E$ ). The relationship between true anomaly and eccentric anomaly is

$$\cos v = \frac{\cos E - e}{1 - e \cos E} \quad (2.3.4)$$

$$\sin v = \frac{\sqrt{1 - e^2} \sin E}{1 - e \cos E} \quad (2.3.5)$$

And the relationship between mean anomaly and eccentric anomaly is

$$M = E - e \sin E(t) \quad (2.3.6)$$

The orbit propagator model can now be made by using the change of the mean anomaly in time. The prediction of the future position becomes relatively straight

forward thanks to keplerian elements for a single point in time. Given the Keplerian elements for a time,  $t_0$ , a prediction of the orbit is

$$M(t_0 + t) = M(t_0) + n \cdot t \quad (2.3.7)$$

where  $t$  is the time passed since  $t_0$ . Equation (2.3.7) describes the motion of the spacecraft in ECOF, coordinates. To transform this to ECEF frame it is required to solve Kepler's equation which relates the eccentric anomaly to the mean anomaly.

$$E(t) = M(t) + e \cdot \sin E(t) \quad (2.3.8)$$

This equation can be solved iteratively such as:

$$E_{i+1} = M + e \sin E_i \quad (2.3.9)$$

It is taken  $E_0 = 0$  for the initial condition as does Newton method and finally the following solution is obtained:

$$E_{i+1} = E_i + \frac{M + e \sin E_i - E_i}{1 - e \cos E_i} \quad (2.3.10)$$

Finally, the vector from the center of the Earth to the satellite expressed in the ECOF is formulated by using the eccentric anomaly as follows:

$$r^{OC} = a \begin{bmatrix} \cos E - e \\ \sqrt{1 - e^2} \sin E \\ 0 \end{bmatrix} \quad (2.3.11)$$

The orbit propagator can now be implemented in ECI frame and ECEF frame using the rotation in Eq. (A.3.1) and Eq. (A.3.2)

$$r^I = C_{OC}^I r^{OC} = C_z(-\Omega) C_x(-i) C_z(-\omega) r^{OC} \quad (2.3.12)$$

$$r^E = C_{OC}^E r^{OC} = C_z(-\Omega + \theta) C_x(-i) C_z(-\omega) r^{OC} \quad (2.3.13)$$

where  $\Omega$  is the Right Ascension of Ascending Node,  $i$  is the inclination of the satellite,  $\omega$  is Argument of Perigee and  $\theta$  is the ascension of the zero meridians.

An orbit propagator based only on the Keplerian elements will degrade in accuracy over time. In order to prevent from this error, certain improvements utilizing known irregularities can be made. The biggest source of degradation is the nonspherical shape of the Earth.. The deformation is often parameterized by the geopotential function as described in Wertz and Larson (1999), which uses the deformation coefficients  $J_i$  for  $i^{th}$  order deformations. The other error sources which are less influence on the perturbations of the spacecraft's orbit can be listed as gravitational forces from the sun and the moon, tidal earth and ocean, and different electromagnetic radiations [13]. In the following sub-sections the descriptions of these perturbations are given respectively:

### ***Perturbations due to the nonspherical Earth***

The earth has not a perfect spherical shape; actually it has a bulge at the equator, is flattened at the poles and is slightly pear-shaped. This imperfect form leads to perturbations in all Keplerian elements. In the second order deformation of the Earth it is considered that the Earth is partly flattened, and leads to the largest perturbations in the Keplerian elements. According to the Lagrange planetary equations, the flattening factor  $J_2$  is governed by using the time derivatives functions of the right ascension of the ascending node and the argument of perigee:

$$\dot{\Omega}_{J_2} = -\frac{3}{2}na_e^2 \frac{\cos i}{a^2(1-e^2)^2} J_2 \quad (2.3.14a)$$

$$\dot{\omega}_{J_2} = \frac{3}{4}na_e^2 \frac{5\cos^2 i - 1}{a^2(1-e^2)^2} J_2 \quad (2.3.14b)$$

where  $a_e$  is the Earth radius, and the numerical value of  $J_2$  for the Earth is  $1.08284 \cdot 10^{-3}$ .

### ***Perturbations due to the sun and the moon***

The Sun and the moon cause periodic variations in all Keplerian elements. There are only secular perturbations to the right ascension of the ascending node and the argument of perigee. An approximation is suggested by Wertz and Larson (1999) for nearly circular orbits as [13]:

$$\dot{\Omega}_{sun} = -0.00154 \frac{\cos i}{n} \quad (2.3.15)$$

$$\dot{\Omega}_{moon} = -0.00338 \frac{\cos i}{n} \quad (2.3.16)$$

and

$$\dot{\omega}_{sun} = 0.00077 \frac{5\cos^2 i - 1}{n} \quad (2.3.17)$$

$$\dot{\omega}_{moon} = 0.00169 \frac{5\cos^2 i - 1}{n} \quad (2.3.18)$$

where  $n$  is the number of the revolution per day and  $\dot{\Omega}$  and  $\dot{\omega}$  units are given in degree/day.

### ***Perturbations due to the atmospheric drag***

The atmospheric drag is a force which causes acceleration in the opposite direction of the spacecraft's velocity. The magnitude of this acceleration depends on the

velocity  $V$ , mass  $m$ , cross section area  $A$ , drag coefficient  $C_D$  of the satellite and on the density of the atmosphere  $\rho$ . This relation is given by the following formula:

$$a_D = -\frac{1}{2}\rho\frac{C_D A}{m}V^2 \quad (2.3.19)$$

The atmospheric drag is a breaking force and it causes the energy loss of the satellite in orbit. This energy loss leads to a decrease in orbital height, but the magnitude is a very low rates. Therefore this effect is not included in orbit propagator model.

### ***Perturbations due to the solar radiation***

The acceleration caused by the solar radiation creates the perturbations on satellite's orbit. The magnitude of this acceleration is given as:

$$a_R = -4.5 \cdot 10^{-6} (1+r) \frac{A}{m} \quad (2.3.20)$$

where  $r$  is the reflection factor between 0 and 1,  $A$  is the cross section area and  $m$  is the mass. The magnitude of these perturbations is less for lower orbit, for this reason it is not included on the orbit propagator model.

The improved orbit propagator; that all perturbations are included; can be reformulated in ECEF frame as follows:

$$r^E = C_z \left( -(\dot{\Omega}_0 + (\dot{\Omega}_{J_2} + \dot{\Omega}_{sun} + \dot{\Omega}_{moon})t) + \theta_0 + \omega_e \right) \cdot C_x(-i) \cdot C_z \left( -(\omega_0 + (\dot{\omega}_{J_2} + \dot{\omega}_{sun} + \dot{\omega}_{moon})t) \right) \cdot a \begin{bmatrix} \cos E - e \\ \sqrt{1-e^2} \sin E \\ 0 \end{bmatrix} \quad (2.3.21)$$

The position of the satellite can be indicated also in spherical coordinate system by using the radius  $\bar{r}^E$ , latitude  $\Phi$  and longitude  $\lambda$  parameters. The radius of the satellite orbit can be computed as Eq. (2.3.22) by using the position vector given in the Eq. (2.3.21). After that latitude and longitude values are calculated by the trigonometric functions given below (Eq. (2.3.23) & Eq. (2.3.24)):

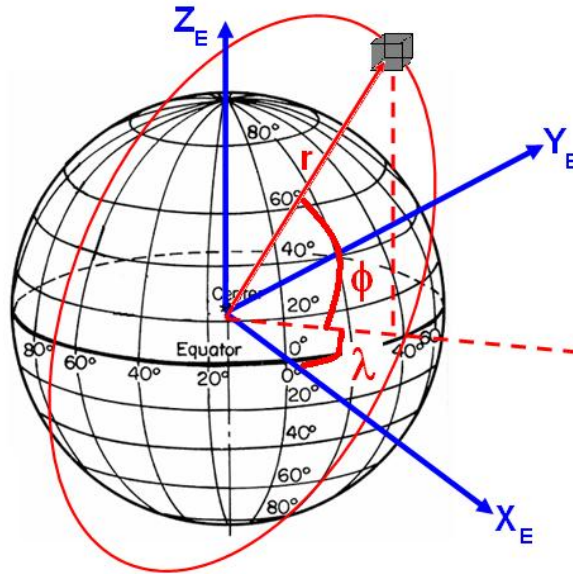


**Figure 2-14: Satellite Position in Spherical Coordinates**

$$\bar{r}^E = \sqrt{(r_x^E)^2 + (r_y^E)^2 + (r_z^E)^2} \quad (2.3.22)$$

$$\Phi = \sin^{-1}(r_z^E / \bar{r}^E) \quad (2.3.23)$$

$$\lambda = \tan^{-1}(r_y^E / r_x^E) \quad (2.3.24)$$

This orbit propagator model will also degrade with time, but this degradation is not as fast as the simple orbit propagator. It is possible to update this model with the accurate Keplerian elements in order to keep it accurate [10]

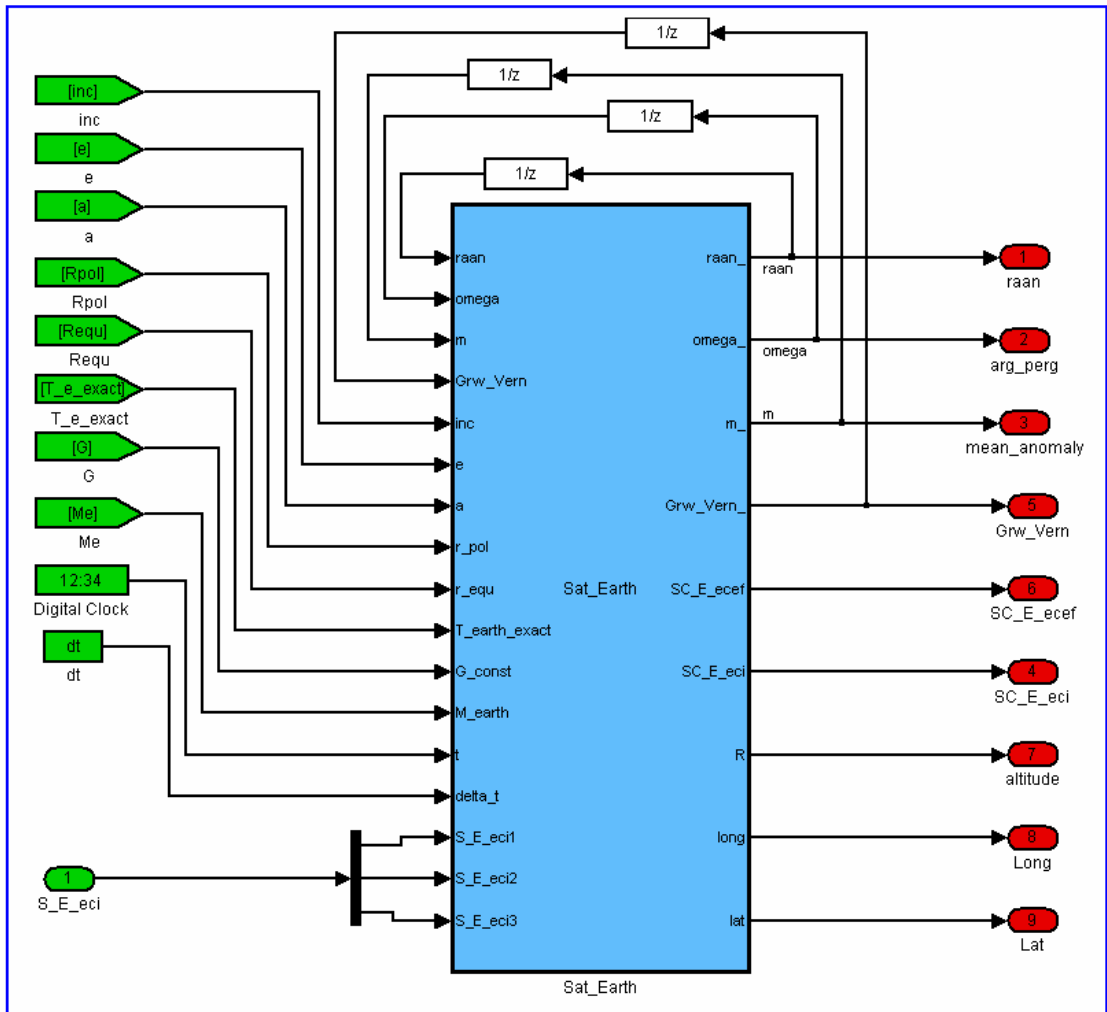


**Figure 2-15: Orbit Propagator Model Block Diagram**

The simulation module of the orbit propagator model is prepared in Matlab/SIMULINK. This module with its inputs and outputs is given in the foregoing Figure 2-15

### 2.3.2 Sun Position Model

It is known that the sun sensor measures the direction and/or intensity of the lights, origin from the Sun, in body frame of the satellite. In order to utilize the measured body frame sun vector, the sun vector in orbit frame must be known in such a way that the rotation between the two could be calculated. For the computation of the sun

vector, the sun movement with respect to the Earth is modeled given the classical orbital parameters as a two body problem.

Sun position with respect to the Earth is calculated by using the classical orbit parameters for the Earth's movement around the sun and reference time denoted epoch (Julian Date). As a first step, by using the Kepler's equation the eccentric anomaly  $\Psi$  is calculated from the mean anomaly  $M$  and the eccentricity  $e$ .

$$M = \Psi - e \sin(\Psi) \quad (2.3.25)$$

In order to find  $\Psi$ , the solution of the Kepler's equation has to be sought for iteratively. In fact, there is no closed form solution but for very near circular orbit suggest a series expansion that results in the following approximation [14]

$$\Psi = M + e \cdot \sin M \cdot (1 + e \cdot \cos M) \quad (2.3.26)$$

Since the Earth's orbit around the Sun has a very small eccentricity, the approach given above is sufficiently accurate [14]. After calculation of the eccentric anomaly, the following equations are used to compute the true anomaly:

$$R_x = R \cos \Theta = a (\cos \Psi - e) \quad (2.3.27)$$

$$R_y = R \sin \Theta = a \left( \sqrt{1 - e^2} \sin \Psi \right) \quad (2.3.28)$$

$$\Theta = \tan^{-1}(R_y / R_x) \quad (2.3.29)$$

and the distance from Earth to Sun is found as:

$$R = \sqrt{R_x^2 + R_y^2} \quad (2.3.30)$$

From the knowledge of the argument at perihelion  $\omega$  and the true anomaly  $\Theta$ , the suns longitude is calculated as below:

$$lon_{sun} = \Theta + \omega \quad (2.3.31)$$

The coordinates of the sun position expressed in rectangular coordinates in elliptic plane system can be given as:

$$\begin{aligned} x_s &= R \cos(lon_{sun}) \\ y_s &= R \sin(lon_{sun}) \\ z_s &= 0 \end{aligned} \quad (2.3.32)$$

and finally these rectangular coordinates expressed in inertial geocentric coordinate system can be written as follows:

$$\begin{aligned} x_e &= x_s \\ y_e &= y_s \cos(e) \\ z_e &= y_s \sin(e) \end{aligned} \quad (2.3.33)$$

The simulation module of the sun position model, prepared by Matlab/SIMULINK, is given with its inputs and outputs in the following Figure 2-16.

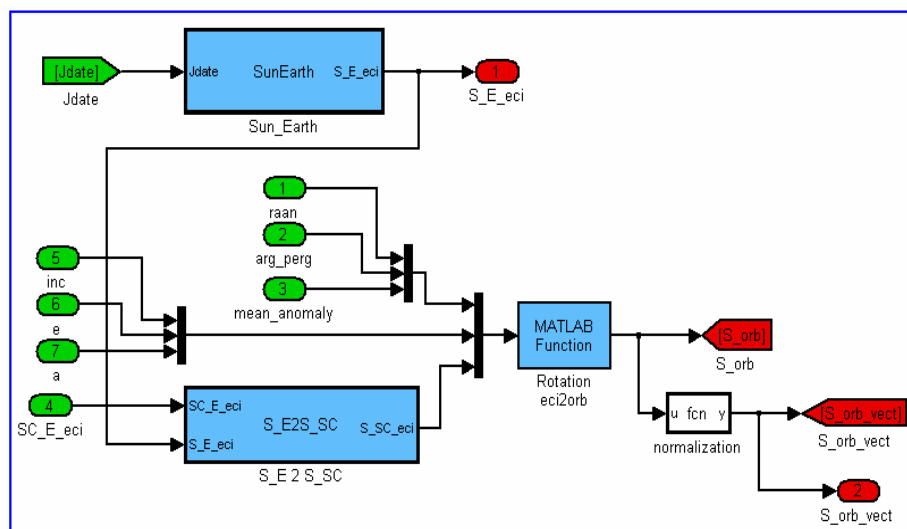


**Figure 2-16: Sun Position Model Block Diagram**

This sun position model will be used to get the direction of the sun light with respect to satellite and simulate the sun sensor measurements as indicated in the beginning of this subchapter. However there is one lighter source that effects the measurements of sun sensor called *Earth Albedo*. Earth Albedo is the reflection of the suns energy from the Earth. This effect seen on the sun sensor measurements should be taken into consideration in order to get more accurate attitude knowledge. Implementation of combining the sun model and Earth Albedo model is not considered in this thesis; it should be done as part of future work.

### 2.3.3 Earth Magnetic Field Model

In order to determinate the magnetic vector and compare this vector with magnetometer measurements, the earth's magnetic field must be known. As seen on Figure 2-17, the magnetic field is highly varying over the Earth's surface, hence usage of the high-resolution lookup-table, where each entry represents the magnetic field at that given position, would demand a very large memory on board a satellite's microcontroller. Therefore, a model called International Geomagnetic Reference Field (IGRF) model is used to obtain the Earth's magnetic filed values at a specific satellite's orbital position.

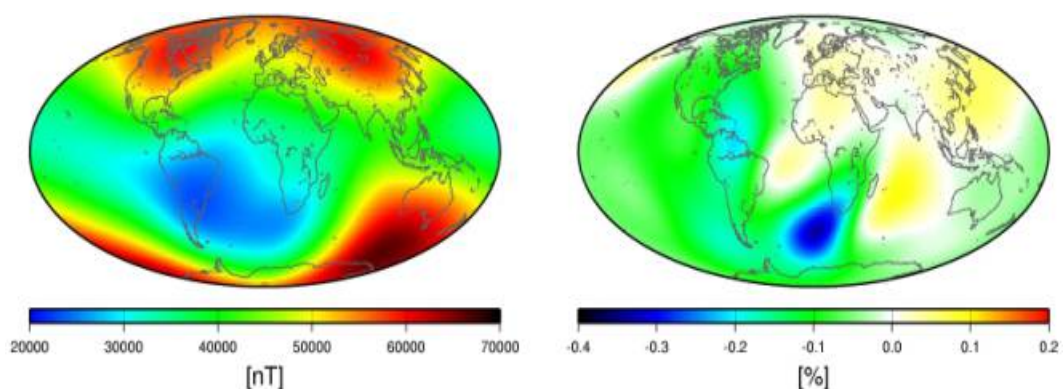


Figure 2-17: Magnitude of the Earth's Magnetic Field [14]

IGRF is an attempt by the International Association of Geomagnetism and Aeronomy (2003), IAGA, to provide a model acceptable to a variety of users. It gives a reasonable approximation of the Earth's magnetic field originating from the Earth's core. The IGRF specifies the numerical coefficients of a truncated spherical harmonic series at any given time and position. The IGRF model is specified every 5 years, for epochs 2000.0, 2005.0 etc. IAGA released the 10<sup>th</sup> Generation International Geomagnetic Reference Field, the latest version of a standard mathematical description of the Earth's main magnetic field. IAGA decided in 2001 that the main-field coefficients of the IGRF from the year 2000 onwards should extend to degree  $n_{\text{max}}=13$  and be quoted to 0.1 nT precision. Pre-2000 coefficients extend to degree 10 or 8 and are quoted to 1 nT precision. The predictive secular variation coefficients for the upcoming five-year epoch are given to degree 8 with a precision of 0.1 nT/year [14].

The IGRF model consists of a set of spherical harmonic coefficients called Gauss coefficients,  $g_n^m$  and  $h_n^m$ , in a truncated series expansion of a geomagnetic potential function of internal origin given in the following Eq. (2.3.34).

$$V = a \sum_{n=1}^N \sum_{m=0}^n \left( \frac{a}{r} \right)^{n+1} \left( g_n^m \cos(m\lambda) + h_n^m \sin(m\lambda) \right) P_n^m \cos(\bar{\phi}) \quad (2.3.34)$$

where  $V$  is the geomagnetic scalar potential,  $a$  is the mean radius of Earth (6371.2 km) and  $r, \lambda, \bar{\phi}$  are the geocentric spherical coordinates:  $r$  is the distance from the centre of the Earth,  $\lambda$  is the longitude eastward from Greenwich,  $\bar{\phi}$  is the colatitudes equal  $90^\circ$  minus the latitude. The maximum spherical harmonic degree of the expansion is  $N$ .  $P_n^m \cos(\bar{\phi})$  is the Schmidt quasi-normalized associated Legendre functions of degree  $n$  and order  $m$ , where  $n \geq 1$  and  $m \leq n$ .

Magnetic field estimation can be made by using IGRF model and the orbit propagator model together. As the IGRF model is rotating with the Earth, it is given

in ECEF frame. The magnetic field in earth centered orbit frame is defined by using the inverted rotation given in Eq. (2.3.13):

$$MAG^{OC} = \left( C_z(-\Omega + \theta) C_x(-i) C_z(-\omega) \right)^{-1} MAG^{ECEF} \quad (3.3.35)$$

$$\Rightarrow MAG^{OC} = C_z(\omega) C_x(i) C_z(\Omega - \theta) MAG^{ECEF} \quad (3.3.36)$$

where  $MAG^{ECEF}$  is the resulting vector obtained from the IGRF model.

Finally, a rotation from Earth centered orbit frame to orbit frame is done by the following transformation:

$$MAG^O = C_x(\pi/2) C_z(v + \pi/2) MAG^{OC} \quad (2.3.37)$$

$$MAG^O = \begin{bmatrix} 1 & 0 & 0 \\ 0 & 0 & 1 \\ 0 & -1 & 0 \end{bmatrix} \begin{bmatrix} -\sin v & \cos v & 0 \\ -\cos v & -\sin v & 0 \\ 0 & 0 & 1 \end{bmatrix} MAG^{OC} \quad (2.3.38a)$$

$$MAG^O = \begin{bmatrix} -\sin v & \cos v & 0 \\ 0 & 0 & 1 \\ \cos v & \sin v & 0 \end{bmatrix} MAG^{OC} \quad (2.3.38b)$$

where  $v$  is the true anomaly.

The three components of the magnetic field in orbit frame for 5 orbits navigation, based on orbit data from the enhanced orbit estimator, are shown in the following Figure 2-18. The  $y$  axis of the orbit frame point in more or less the same direction all the time, and this cause the small variation on the  $y$  component of the magnetic field vector.

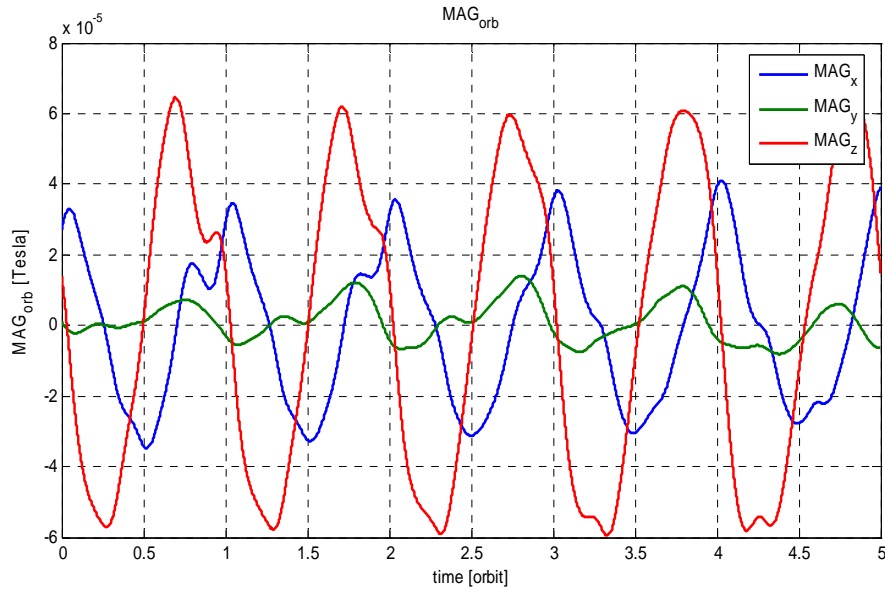


**Figure 2-18: The Earth’s Magnetic Field from IGRF Model**

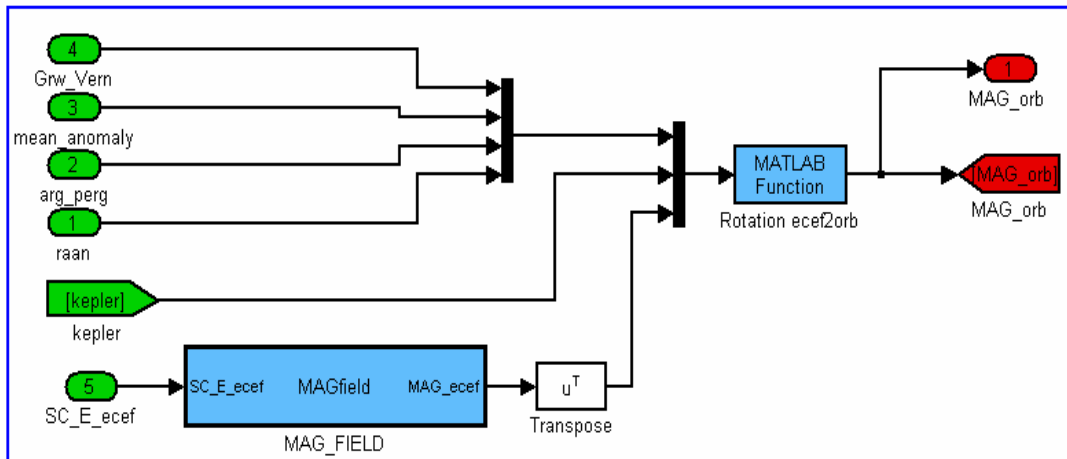


**Figure 2-19: Earth Magnetic Field Model Block Diagram**

The simulation module of the Earth Magnetic Field Model is prepared on Matlab/SIMULINK. This created block diagram can be seen in the following Figure 2-19 with its inputs and outputs.

## 2.4 Sensor Measurements Models

In this section, the detailed explanations about the mathematical measurement model of the sensors, which are used on the spacecraft to obtain its angular velocity and attitude, are given. The main targets of constituting the measurement model of the sensors are to simulate the sensors' measurements, to obtain the performance of these sensors and to see the accuracy of the attitude determination system.

Generally, the attitude determination system of a LEO satellite consists of inertial sensors and reference sensors. In this thesis, sensor systems of the hypothetical satellite, which specifications are given in Section 2.1.3, is composed of one inertial sensor (three axis rate gyroscope) and three reference sensors (three axis magnetometers, three axis sun sensor and 3 axis star tracker). The details about the measurements model of these sensors are given in the following subchapters.

### 2.4.1 Rate Gyroscopes

A gyroscope is an instrument which uses a spinning mass with a high velocity for the purpose of sensing and responding to changes in the inertial orientation of its spin axis [12]. Nowadays, the usage of the new technological product, called Micro-Electro-Mechanical Systems (MEMS) based rate gyros also become widespread.

Rate Gyros are usually the basic sensor of an automatic control system for either angular velocity control or attitude control. Rate Gyros measures the angular velocity of the vehicle with respect to the inertial reference frame [15]. For perfect measurement, without noises and errors, its output may be defined as follows:

$$\omega_{MEAS\_perfect} = \omega_{IB}^B \quad (2.4.1)$$

It is clear that the real measurements will not be perfect; therefore the simulation of the Rate Gyros measurement model is created that includes various errors. In the following Table 2-2, the error parameters defined for Rate Gyros are given and the

explanations about these parameters are listed respectively in the following subchapters.

**Table 2-2: Error Parameters of the Rate Gyros Model**

a. Turn on Bias
b.1. Bias Stability
2. The Correlation Time of the Bias Stability
c.1. Random Walk
2. Bandwidth of the random walk
d. Scale Factor Error
e. Misalignment Error

#### 2.4.1.1 Turn On Bias

Turn on Bias error is modeled as a Gaussian distribution and defined with  $1\sigma$  standard deviation value. This bias is computed at the beginning of the simulation, when  $t_0 = 0\text{sec}$ , and then it is taken constant during the simulation. The block diagram of the Turn on Bias model created on Matlab/SIMULINK is given in the following Figure 2-20 [16].

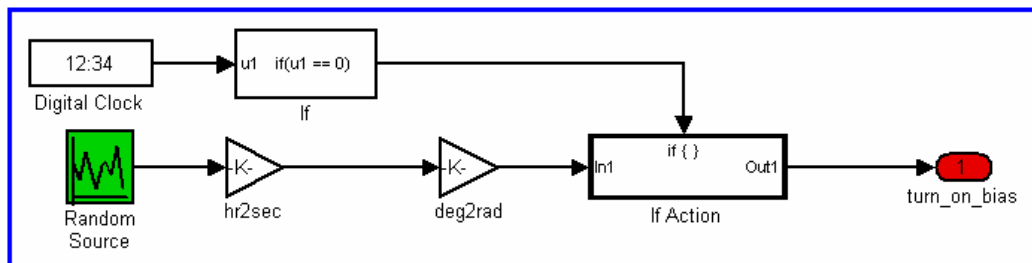


**Figure 2-20: Rate Gyro Turn on Bias Error Model**

#### 2.4.1.2 Bias Stability

Bias is a long term average of the data and it has no meaning in terms of a single data point. Thus, a long sequence of data must be taken and the average of these data must be computed in order to determine the bias. A *Bias Stability* term refers to changes in the bias measurements [17].

In the computation of bias stability, the time sequence is also an important parameter when collecting the measurements. The rate gyros outputs are read at a fixed frequency denoted  $\tau$  and the variance of the measurements are computed depending on this  $\tau$ . This parameter  $\tau$  is called as *The Correlation Time of the Bias Stability*.

The block diagram of the Bias Stability model created on Matlab/SIMULINK can be seen in the following Figure 2-21. In this model the correlation time value is taken as 20 seconds [17].

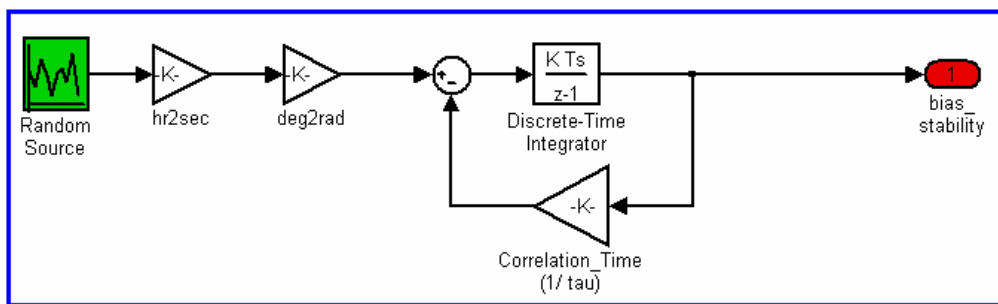


**Figure 2-21: Bias Stability Error Model**

### 2.4.1.3 Random Walk

The *Allan Variance* parameter, which is related to the bias stability error parameter, should be stated before explaining the *Random Walk (RW)* error. In order to obtain a quantitative measure of how much the bias stability value of the rate gyro measurements change at that particular value of averaging time (correlation time)  $\tau$ , the Allan Variance equation is derived [17]:

$$AVAR^2(\tau) = \frac{1}{2(n-1)} \sum_i (y(\tau)_{i+1} - y(\tau)_i)^2 \quad (2.4.2)$$

where  $AVAR(\tau)$  is the Allan Variance as a function of the averaging time  $\tau$ ;  $y(\tau)_i$  is the average value of the measurement in set  $i$ ; and  $n$  is the total number of measurements. After computing the  $AVAR(\tau)$  values for the different averaging time

$\tau$ , a graph the  $AVAR(\tau)$  results as a function of  $\tau$ . Figure 2-22 shows the results for this data, along with the error in the calculation. For clarity, the  $AVAR(\tau)$  data is plotted on a log-log scale [17].

For the short correlation times  $\tau$ , the Allan Variance is dominated by the noise in the sensor. There is a direct correlation between the standard deviation  $\sigma$  (the noise) of the output vs. time with the slope of the Allan Variance at small  $\tau$ . This is also referred to as *Angle Random Walk (ARW)* [17].

As seen in the Allan Variance plot (Figure 2-22), a better measure of the bias is obtained by increasing the correlation time  $\tau$ . However at some point, an interesting behavior on the measurements error happens as the  $\tau$  increases. At some point the Allan Variance starts to increase again because of the *Rate Random Walk (RRW)* in the sensor, this is an inherent instability in the output of the sensor. The standard definition of bias instability used by inertial sensor manufacturers is the minimum point on the Allan Variance curve. This is the best stability that can be achieved with a fully modeled sensor and active bias estimation [17].

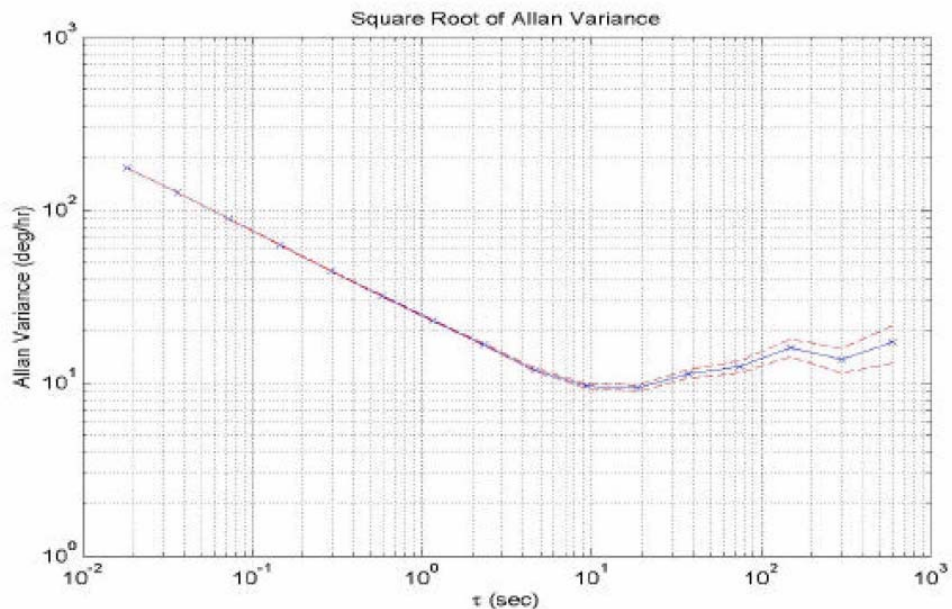


**Figure 2-22: The Allan Variance Result for The Rate Gyros Data [14]**

In the rate gyro measurement model used in this thesis, the *Random Walk* is taken as a Gaussian distribution white noise and defined with  $1\sigma$  standard deviation value. The converter equation used to obtain  $1\sigma$  value from *RW* is formulated as follows:

$$\begin{aligned}
 RW &\equiv y ; \text{ White\_Noise} \equiv z (1\sigma) \\
 z &= y \left( \frac{\text{deg}}{\sqrt{\text{hr}}} \right) = y \left( \frac{\text{deg}}{\sqrt{\text{hr}}} \right) \frac{\sqrt{3600 \text{ sec}}}{\sqrt{\text{hr}}} = y \left( \frac{\text{deg}}{\text{hr}} \right) 60 \sqrt{\text{sec}} \left( \frac{\sqrt{1/\text{sec}}}{\sqrt{\text{Hz}}} \right) \rightarrow \\
 z &= y 60 \frac{1}{\sqrt{\text{Hz}}} \left( \frac{\text{deg}}{\text{hr}} \right)
 \end{aligned}
 \tag{2.4.3}$$

where *Hz* is the *Bandwidth* of the measurements taken.

The block diagram of the *Random Walk* model created on Matlab/SIMULINK is given in the following Figure 2-23.

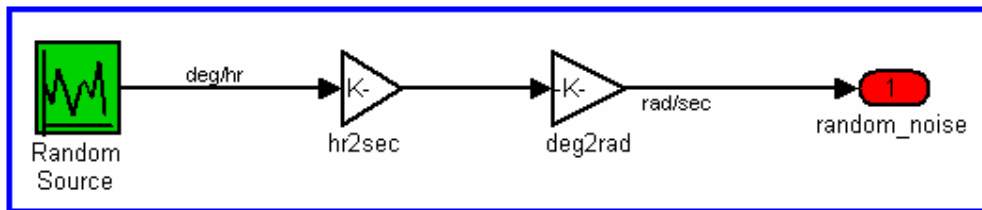


**Figure 2-23: Random Walk Error Model**

#### 2.4.1.4 Scale Factor Error

The *Scale Factor Error* is a kind of error that depends on the measured values. This error is defined as a Gaussian distribution and the  $1\sigma$  standard deviation value is given in the product specification sheets. Therefore, this error is computed at the beginning of the simulation, when  $t_0 = 0\text{sec}$ , by considering the  $1\sigma$  error distribution. The following Figure 2-24 shows the block diagram of the Scale Factor Error model created on Matlab/SIMULINK.

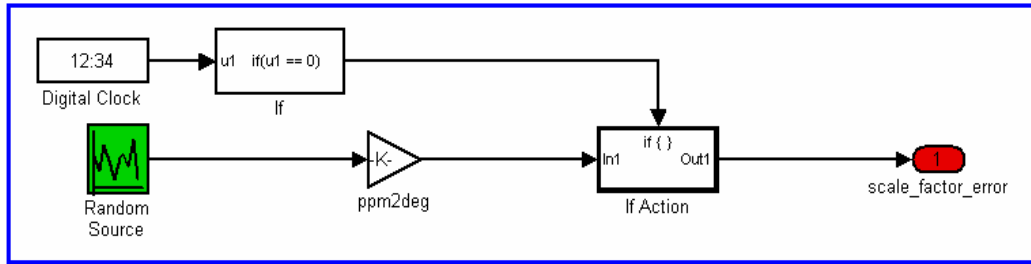


**Figure 2-24: Scale Factor Error Model**

#### 2.4.1.5 Misalignment Error

The sensor *Misalignment Error* is kind of manufacturing error and it occurs because of the no coincidence between the sensor axis frame and the measurement axis frames. The block diagram model created for the misalignment error has the same structure with the scale factor error; therefore Figure 2-24 describes also the misalignment error model.

The Rate Gyros Measurement Model is created by using all the error types defined above, and the block diagram of this model can be seen in the Figure 2-25.

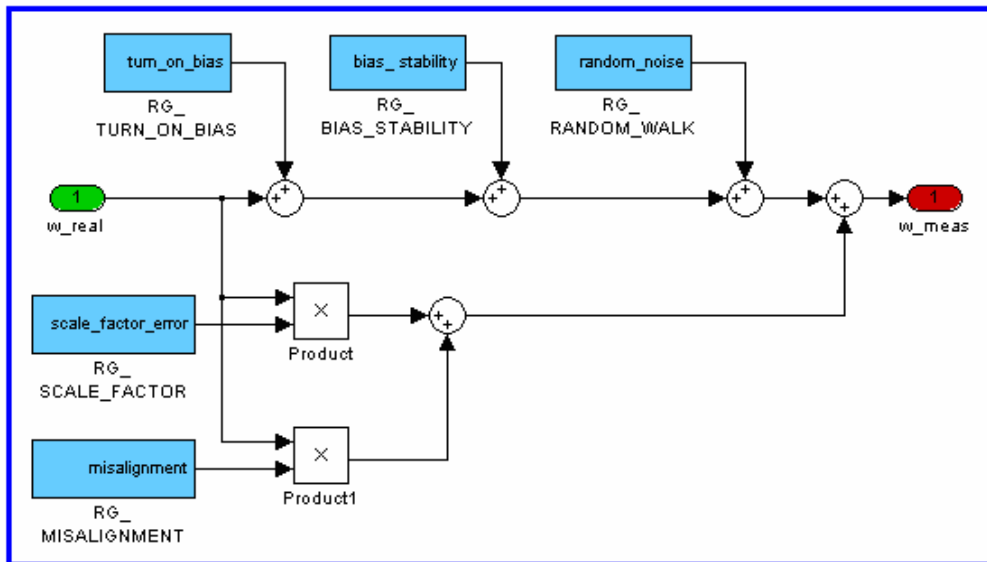


**Figure 2-25: Rate Gyro Measurement Model Block Diagram**

Rate Gyro selected for the simulations of the satellite attitude determination system is a Fiber Optic Gyro of the Northrop Grumman called FOG200. The specification sheet of this product is given in the Appendix B.1. The values of the error determined depending on the specification document of the product are listed in the following Table 2-3.

**Table 2-3: NG FOG-200 specifications**

<b>RG PARAMETERS</b>	<b>NG FOG 200</b>
a. Turn on Bias (deg/hr)	0.01
b.1. Bias Stability (deg/hr)	0.25 , 3 (over temp.)
2. The Correlation Time of the Bias Stability (sec)	20
c.1. Random Walk (deg/rt-hr)	0.012
2. Bandwidth of the random walk (Hz)	500
d. Scale Factor Error (ppm)	100, 2000 (over temp.)
e. Misalignment Error (mrad)	10

#### **2.4.2 Sun Sensor**

Sun sensors are the most widely used sensor type in the attitude determination and control system of the spacecrafts because of the several factors: for most applications, the Sun can be considered as a point-source because the angular radius of the Sun is nearly orbit independent and sufficiently small (0.267 deg at 1 AU); this independence simplifies both sensor design and attitude determination algorithms; Sun is sufficiently bright to permit the use of simple, reliable equipment without discriminating among sources; and their power consumption is low [15].

The Sun sensor measures the Sun position vector with respect to the satellite axis frames. From the knowledge of the Sun and satellite orbital locations, the current and expected measurements can be compared to determine the attitude of the satellite. The Sun position vector is computed by using the Sun position model described in Section 2.3.2.

The Sun sensor measurements are simulated by using the attitude matrix of the satellite. The measurement noise for this sensor is defined as a Gaussian distribution with  $1\sigma$  standard deviation.

$$S_{meas} = C_O^B \cdot S^O + v_{SUN} \quad (2.4.4)$$

where;  $S_{meas}$  is the measurement vector that gives the Sun position vector,  $S^O$  is the vector of the Sun position defined in orbital reference frame,  $C_O^B$  is the attitude matrix from orbital frame to body frame,  $v_{SUN}$  is the measurement noise vector of the Sun sensor.

The simulation module formed on Matlab/SIMULINK for the Sun sensor is given in Figure 2-26. This block diagram shows related inputs and outputs of the Sun Sensor Measurement Model.

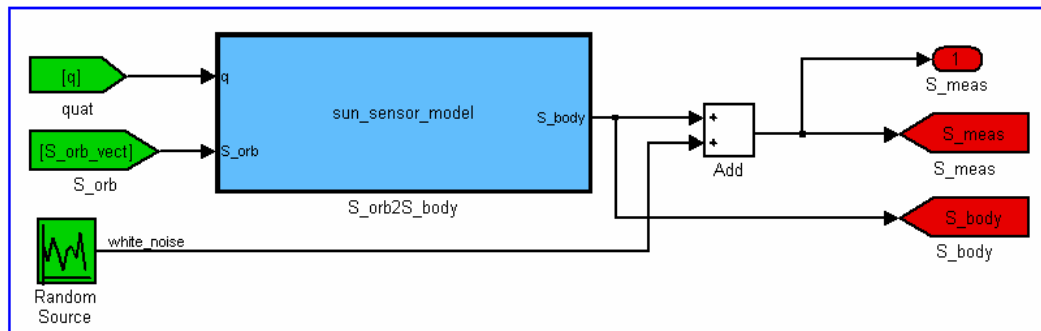


**Figure 2-26: Sun Sensor Measurement Model Block Diagram**

Sun Sensor selected for the simulations of the satellite attitude determination system is a product of Optical Energy Technologies (*Model 0.5 Sun Sensor*). The specification sheet of this product is given in the Appendix B.2. This Sun sensor is 2 axis sensor which has a accuracy  $0.5^0$  with a  $100^0$  of Field of View (FoV). In order to obtain 3 axis reference knowledge 2 unit of this sensor are used in the satellite attitude determination simulations.

### 2.4.3 Magnetometers

Magnetometers are widely used in the attitude sensor system of the spacecrafts for a variety of reasons: they provide both the direction and magnitude of the magnetic field as they are reference sensors; they are lightweight and their power consumption is low, have a wide operating temperature and they have no moving parts [15].

However, magnetometers are not accurate sensor because the magnetic field is not completely known and the models used to estimate the magnetic field magnitude and direction at the spacecraft's position may have substantial errors. Furthermore, because the Earth's magnetic field magnitude decrease depending on the distance from the Earth (as  $1/r^3$ ), the total magnetic field measurement are dominated by the residual spacecraft magnetic biases. Because of this effect, the magnetometers are not effective for the spacecraft at altitudes above 1000 km [15].

Magnetometer measures the magnitude of the magnetic field with respect to the spacecraft axis frames. In practice, in order to determine the attitude of the spacecraft, these measurements are compared with the magnitude of the magnetic field known with respect to orbital reference frame. Magnetic field values defined in orbital reference frame are computed by using the IGRF model and Orbit Propagator that detailed descriptions are given in the Section 2.3.3.

The magnetometer measurements are formulated using the attitude matrix that gives the rotation information between the satellite and orbital reference frames and the measurement noises defined as a Gaussian distribution with  $1\sigma$  standard deviation value.

$$MAG_{meas} = C_O^B \cdot MAG^O + v_{MAG} \quad (2.4.5)$$

where  $MAG_{meas}$  is the vector of the magnetometer measurements,  $MAG^O$  is the vector of the magnetic field values defined in orbital reference frame,  $C_O^B$  is the attitude matrix from orbital frame to body frame,  $v_{MAG}$  is the vector of the measurement noises.

The simulation module of the Magnetometer is prepared on Matlab/SIMULINK. This created block diagram is given in the following Figure 2-27 with its inputs and outputs.

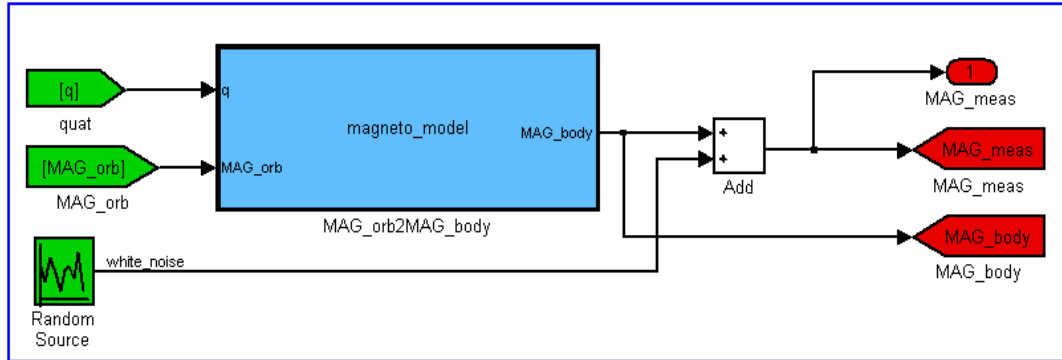


**Figure 2-27: Magnetometer Measurement Model Block Diagram**

Magnetometer selected for the simulations of the satellite attitude determination system is a product of *Zarm Technik*. The specification sheet of this product is given in the Appendix B.3. The values of the error determined depending on the specification document of the product are listed in the following Table 2-4.

**Table 2-4: Magnetometer Specifications**

MAG PARAMETERS	ZARM
Range	+/- 64e-6 T
Scale Factor	App. 0.5e-9 T
Resolution/Noise	100e-12 T @ 1Hz 5e-9 T @ 50 Hz
Accuracy	0.64e-6 T
Alignment	1 deg
Sampling rate	50 Hz

#### 2.4.4 Star Sensor

Star sensor measures the star directions in the satellite body axis frame. This sensor provides attitude information by comparing its measurements with known star directions from its star catalog. Star sensors are the most accurate sensors used in the

attitude system. It is possible to obtain accuracy in arc-second range. However, they are expensive, heavy and they need more power than most other sensors. Furthermore, they need extensive computation. The usage of the star sensors also suffers due to the obscuration and interference from the Sun, the Earth, and other bright sources. However, in spite of these disadvantages, the accuracy and the versatility of the star sensors have led to applications in a variety of different spacecraft attitude environments [15].

Since the star sensor fuses the measurements of stars directions, it is possible to obtain the quaternion direction, as output. Therefore, in the star sensor measurement model the quaternion knowledge obtained from the satellite kinematics model is used. In order to simulate the real measurements, a Gaussian distribution white noise is added to the quaternion values. Consequently, quaternion measurements are formulated as follows:

$$q_{meas} = q + v_q \quad (2.4.6)$$

where;  $q_{meas}$  is the measured quaternion,  $q$  is the real quaternion and  $v_q$  is the white noise with  $1\sigma$  variance value. The block diagram of the Star sensor measurement model can be seen in the following Figure 2-28 with its inputs and outputs. This simulation module is prepared on Matlab/SIMULINK.

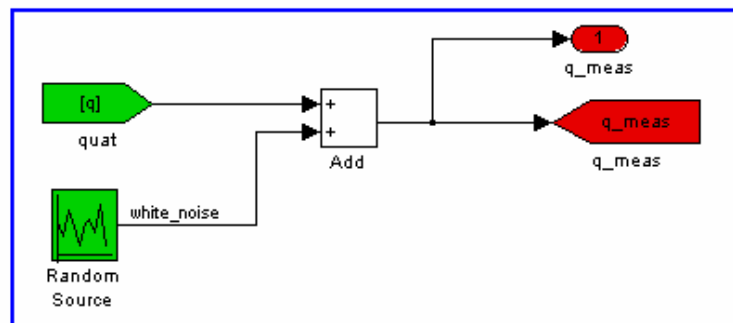


**Figure 2-28: Star Sensor Measurement Model Block Diagram**

Star Sensor selected for the simulations of the satellite attitude determination system is a product of Jena Optronik.

**Table 2-5: Star Sensor Specifications**

<b>STAR SENSOR</b>	<b><i>ASTRO 15</i></b>
Star Accuracy: Bias (1 sigma)	<i>2.5 arcsec</i>
Star Accuracy: Noise (1 sigma)	<i>2.5 arcsec</i>
<i>LOS Accuracy:</i>	
pitch & yaw (1 sigma)	<i>1 arcsec</i>
roll (1 sigma)	<i>10 arcsec</i>

The specification sheet of this product is given in the Appendix B.3. The errors determined depending on the specification document of the product are listed in the Table 2-5.

## **CHAPTER 3**

### **KALMAN FILTER BASED SATELLITE ATTITUDE DETERMINATION**

This chapter presents a Kalman filter based satellite attitude determination system designed for the hypothetical LEO satellite defined in the previous chapter. In first section the general information about Kalman filter is given, afterwards the theory of the Kalman filter with detailed explanations about different types of the Kalman filters are given. Then, Satellite Attitude Determination System Structure created for a LEO Satellite is presented. In the last section, the sensor fusion algorithms of the attitude determination modes which are related to the sensor activation situation are explained in details. Finally simulation results are given for different orbit navigation and attitude scenarios.

#### **3.1 Kalman Filter Theory and Modeling**

This section describes the derivation of the Kalman filter using the system models and measurement models. Kalman filter contains different structures depending on the linearity and nonlinearity of the system and measurements. In the following subsections the explanations about the linear Kalman filter, Linear Discrete Kalman filter, and Extended Kalman filter is given in details.

##### **3.1.1 Linear Continuous Kalman Filter**

In this section the Kalman Filter is derived using continuous-time models and measurements and this derivation approach provides some unique perspectives that are especially useful for small sampling intervals. However, due to the extensive use

of digital computers in today's time, the continuous-time Kalman filter is not widely used in practice [4].

Consider the following truth linear system model and linear measurement model defined in continuous time:

$$\dot{x}(t) = F(t)x(t) + B(t)u(t) + G(t)w(t) \quad (3.1.1a)$$

$$\tilde{y}(t) = H(t)x(t) + v(t) \quad (3.1.1b)$$

where  $x(t)$  is the  $n \times 1$  state vector,  $F(t)$  is the  $n \times n$  state matrix of the system,  $H(t)$  is the  $m \times m$  measurement matrix,  $w(t)$  and  $v(t)$  are zero-mean Gaussian white noise processes with covariances given by:

$$E\{w(t)w^T(\tau)\} = Q(t) \delta(t - \tau); \quad (3.1.2a)$$

$$E\{v(t)v^T(\tau)\} = R(t) \delta(t - \tau) \quad (3.1.2b)$$

$$\text{where, } \delta(t - \tau) = \begin{cases} 1, & t = \tau, \\ 0, & t \neq \tau. \end{cases} \text{ is the Kronecker expression.} \quad (3.1.2c)$$

$$E\{v(t)w^T(\tau)\} = 0 \quad (3.1.2d)$$

The last equation implies that  $w(t)$  and  $v(t)$  are uncorrelated. The Kalman Filter structure for the estimation of the states and outputs is given by the following equations:

$$\hat{\dot{x}}(t) = F(t)\hat{x}(t) + B(t)u(t) + K(t)[\tilde{y}(t) - H(t)\hat{x}(t)] \quad (3.1.3a)$$

$$\hat{y}(t) = H(t)\hat{x}(t) \quad (3.1.3b)$$

The dynamics of the state vector estimation error parameters ( $\tilde{x}(t) = \hat{x}(t) - x(t)$ ) can be reformulated by using the Eq. (3.1.1) and Eq. (3.1.3) as follows:

$$\dot{\tilde{x}}(t) = E(t)\tilde{x}(t) + z(t) \quad (3.1.4)$$

where;

$$E(t) = F(t) - K(t)H(t) \quad (3.1.5)$$

$$z(t) = -G(t)w(t) + K(t)v(t) \quad (3.1.6)$$

When using the matrix exponential solution for the Eq. (3.1.6), the following expression is obtained for the state propagation:

$$\tilde{x}(t) = \Phi(t, t_0)\tilde{x}(t_0) + \int_{t_0}^t \Phi(t, \tau) z(\tau) d\tau \quad (3.1.7)$$

Here, it is noted that  $u(t)$  cancels in the error state. Since the system error  $w(t)$  and measurement error  $v(t)$  are uncorrelated the following expression is obtained as the covariance matrix of the measurement error:

$$E\{z(t)z^T(\tau)\} = [G(t)Q(t)G^T(t) + K(t)R(t)K^T(t)] \delta(t - \tau) \quad (3.1.8)$$

The state error covariance is defined by

$$P(t) \equiv E\{\tilde{x}(t)\tilde{x}^T(t)\} \quad (3.1.9)$$

As a result, using the Eq. (3.1.7) and Eq. (3.1.8) the time derivative expression of the covariance matrix is obtained. The simplified form of this expression is given as follows:

$$\begin{aligned} \dot{P}(t) = & [F(t) - K(t)H(t)]P(t) + P(t)[F(t) - K(t)H(t)]^T \\ & + G(t)Q(t)G^T(t) + K(t)R(t)K^T(t) \end{aligned} \quad (3.1.10)$$

In order to determine the Kalman gain  $K(t)$ , the minimization on Eq. (3.1.10) with respect to  $K(t)$  is done. The necessary conditions lead to:

$$\frac{\partial J}{\partial K(t)} = 0 = 2K(t)R(t) - 2P(t)H^T(t) \quad (3.1.11)$$

Solving Eq. (3.1.11) for  $K(t)$ , the following expression is obtained:

$$K(t) = P(t)H^T(t)R^{-1}(t) \quad (3.1.12)$$

By substituting this gain expression into Eq. (3.1.10), the following expression known as the *continuous Riccati Equation* is obtained

$$\dot{P}(t) = F(t)P(t) + P(t)F^T(t) - P(t)H^T(t)R^{-1}(t)H(t)P(t) + G(t)Q(t)G^T(t) \quad (3.1.13)$$

**Table 3-1: Continuous-time Linear Kalman Filter [4]**

<b>Model</b>	$\dot{x}(t) = F(t)x(t) + B(t)u(t) + G(t)w(t)$ , $w(t) \sim N(0, Q(t))$ $\tilde{y}(t) = H(t)x(t) + v(t)$ , $v(t) \sim N(0, R(t))$
<b>Initialize</b>	$\hat{x}(t_0) = \hat{x}_0$ $P_0 = E\{\tilde{x}(t_0)\tilde{x}^T(t_0)\}$
<b>Gain</b>	$K(t) = P(t)H^T(t)R^{-1}(t)$
<b>Covariance</b>	$\dot{P}(t) = F(t)P(t) + P(t)F^T(t) - P(t)H^T(t)R^{-1}(t)H(t)P(t) + G(t)Q(t)G^T(t)$
<b>Estimate</b>	$\hat{\dot{x}}(t) = F(t)\hat{x}(t) + B(t)u(t) + K(t)[\tilde{y}(t) - H(t)\hat{x}(t)]$

A summary of the continuous-time Kalman filter is given in the Table 3-1. At first step state and error covariance are initialized. Then, the Kalman gain is calculated

with the initial covariance value. Next, the covariance and estimated states are numerically integrated using the continuous-time measurement. The integration of the estimated state and covariance continues until the final measurement time is reached.

### 3.1.2 Linear Discrete Kalman Filter

In this section the Kalman Filter is derived assuming that both the models and measurements are available in discrete-time form. The truth linear system model and linear measurement model for this discrete-time case is given by [4]:

$$x_{k+1} = \Phi_k x_k + \Gamma_k u_k + \Psi_k w_k \quad (3.1.14a)$$

$$\tilde{y}_k = H_k x_k + v_k \quad (3.1.14b)$$

where  $w_k$  and  $v_k$  are assumed as zero-mean Gaussian white noise processes with covariances given by:

$$E\{v_k v_j^T\} = R_k \delta_{kj} \quad (3.1.15a)$$

$$E\{w_k w_j^T\} = Q_k \delta_{kj} \quad (3.1.15b)$$

$$\text{where; } \delta_{kj} = \begin{cases} 1 & ; k = j \\ 0 & ; k \neq j \end{cases} \quad (3.1.15c)$$

$$E\{v_k w_j^T\} = 0 \quad (3.1.15d)$$

This Kroneker delta requirement preserves the block diagonal structure of the covariance and weight matrices, and it is also assumed that  $v_k$  and  $w_k$  are uncorrelated.

The propagation of the current estimate and the update of the state by using the Kalman gain and measurements are done by using the equations given below:

$$\hat{x}_{k+1}^- = \Phi_k \hat{x}_k^+ + \Gamma_k u_k \quad (3.1.16a)$$

$$\hat{x}_{k+1}^+ = \hat{x}_{k+1}^- + K_k [\tilde{y}_k - H_k \hat{x}_k^-] \quad (3.1.16b)$$

The state error covariance matrix is defined by using the following expression:

$$\begin{aligned} P_k^- &\equiv E \left\{ \tilde{x}_k^- \tilde{x}_k^{-T} \right\}; & P_{k+1}^- &\equiv E \left\{ \tilde{x}_{k+1}^- \tilde{x}_{k+1}^{-T} \right\}; \\ P_k^+ &\equiv E \left\{ \tilde{x}_k^+ \tilde{x}_k^{+T} \right\}; & P_{k+1}^+ &\equiv E \left\{ \tilde{x}_{k+1}^+ \tilde{x}_{k+1}^{+T} \right\} \end{aligned} \quad (3.1.17a)$$

$$\begin{aligned} \tilde{x}_k^- &\equiv \hat{x}_k^- - x_k; & \tilde{x}_{k+1}^- &\equiv \hat{x}_{k+1}^- - x_{k+1}; \\ \tilde{x}_k^+ &\equiv \hat{x}_k^+ - x_k; & \tilde{x}_{k+1}^+ &\equiv \hat{x}_{k+1}^+ - x_{k+1}; \end{aligned} \quad (3.1.17b)$$

The expressions given in Eq. (3.1.17b) are the state errors using in the state prediction and state update. Here, the aim is to derive an expression for both  $P_{k+1}^-$  and  $P_{k+1}^+$ , and also an optimal expression for the Kalman gain  $K_k$ . Since eqn. (3.1.16a) is not a direct function of the gain  $K_k$ , it is fairly straightforward to derive the expression  $P_{k+1}^-$ . After substituting the Eq. (3.1.14a) and Eq. (3.1.16a) into Eq. (3.1.17b), then the following expression for  $P_{k+1}^-$  is obtained:

$$\begin{aligned} P_{k+1}^- &\equiv E \left\{ \tilde{x}_{k+1}^- \tilde{x}_{k+1}^{-T} \right\} \\ &= E \left\{ \Phi_k \tilde{x}_{k+1}^+ \tilde{x}_{k+1}^{+T} \Phi_k^T \right\} - E \left\{ \Phi_k \tilde{x}_{k+1}^+ w_k^T \Psi_k^T \right\} \\ &\quad - E \left\{ \Psi_k w_k \tilde{x}_{k+1}^{+T} \Phi_k^T \right\} + E \left\{ \Psi_k w_k w_k^T \Psi_k^T \right\} \end{aligned} \quad (3.1.18)$$

After carrying out certain simplifications, finally the following expression is obtained for the state covariance propagation:

$$P_{k+1}^- = \Phi_k P_k^+ \Phi_k^T + \Psi_k Q_k \Psi_k^T \quad (3.1.19)$$

The next step is to obtain an expression for the state covariance update. For this purpose the state propagation and the measurement update equations are used. This derivation for the expression for  $P_k^+$  is listed in the following set of equations:

$$\tilde{x}_k^+ = (I - K_k H_k) \hat{x}_k^- + K_k H_k x_k + K_k v_k - x_k \quad (3.1.20)$$

$$\begin{aligned} P_k^+ &\equiv E \left\{ \tilde{x}_k^+ \tilde{x}_k^{+T} \right\} \\ &= E \left\{ (I - K_k H_k) \tilde{x}_k^- \tilde{x}_k^{-T} (I - K_k H_k)^T \right\} \\ &+ E \left\{ (I - K_k H_k) \tilde{x}_k^- v_k^T K_k^T \right\} + E \left\{ K_k v_k \tilde{x}_k^{-T} (I - K_k H_k)^T \right\} \\ &+ E \left\{ K_k v_k v_k^T K_k^T \right\} \end{aligned} \quad (3.1.21a)$$

$$\text{Since } v_k \text{ and } \tilde{x}_k^- \text{ are uncorrelated } \Rightarrow E \left\{ \tilde{x}_k^- v_k^T \right\} = E \left\{ v_k \tilde{x}_k^{-T} \right\} = 0 \quad (3.1.21b)$$

$$P_k^+ = [I - K_k H_k] P_k^- [I - K_k H_k]^T + K_k R_k K_k^T \quad (3.1.22)$$

In order to determine the Kalman gain  $K_k$ , the minimization on Eq. (3.1.22) with respect to  $K_k$  is done. The necessary conditions lead to:

$$\frac{\partial J}{\partial K_k} = 0 = -2(I - K_k H_k) P_k^- H_k^T + 2K_k R_k \quad (3.1.23)$$

$$K_k = P_k^- H_k^T [H_k P_k^- H_k^T + R_k]^{-1} \quad (3.1.24)$$

Substituting Eq. (3.1.24) into Eq. (3.1.22), the simplified expression for the state covariance update is obtained:

$$P_k^+ = [I - K_k H_k] P_k^- \quad (3.1.25)$$

The above Eq. (3.1.25) infer that while the propagation step in Eq. (3.1.19) *increase* the covariance; in the opposite side, the update stage of the discrete-time Kalman filter *decreases* the covariance. This observation is instinctively consistent since in general more measurements improve the state estimate [4].

A further expression for the state update can be derived by using Kalman gain, real measurements and expected measurements as follows:

$$\hat{x}_k^+ = [I - K_k H_k] \hat{x}_k^- + K_k \tilde{y}_k = \hat{x}_k^- - K_k [\tilde{y}_k - H_k \hat{x}_k^-] \quad (3.1.26)$$

A summary for the algorithms of the discrete-time Kalman filter is given in Table 3-2. First, the initialization for the state and covariance are done. If a measurement is available, the state and covariance are updates by using Kalman gain values and the propagation of the state estimate and covariance are calculated for the next step. If a measurement is not available, state and covariance are propagated and this process is repeated until the new measurement is available.

**Table 3-2: Discrete-time Linear Kalman Filter [4]**

<b>Model</b>	$x_{k+1} = \Phi_k x_k + \Gamma_k u_k + \Psi_k w_k, \quad w_k \sim N(0, Q_k)$ $\tilde{y}_k = H_k x_k + v_k, \quad v_k \sim N(0, R_k)$
<b>Initialize</b>	$\hat{x}(t_0) = \hat{x}_0$ $P_0 = E\{\tilde{x}(t_0)\tilde{x}^T(t_0)\}$
<b>Gain</b>	$K_k = P_k^- H_k^T [H_k P_k^- H_k^T + R_k]^{-1}$
<b>Update</b>	$\hat{x}_k^+ = \hat{x}_k^- - K_k [\tilde{y}_k - H_k \hat{x}_k^-]$ $P_k^+ = [I - K_k H_k] P_k^-$
<b>Propagation</b>	$\hat{x}_{k+1}^- = \Phi_k \hat{x}_k^+ + \Gamma_k u_k$ $P_{k+1}^- = \Phi_k P_k^+ \Phi_k^T + \Psi_k Q_k \Psi_k^T$

### 3.1.3 Extended Kalman Filter

As described above, the Kalman filter addresses the general problem of trying to estimate the states of a linear discrete-time process; however a large class of estimation problem involves nonlinear models. A vast majority of such nonlinear applications use a Kalman filter that linearizes about the current mean and covariance, and this type of filter is called as an *Extended Kalman filter (EKF)* [18].

In order to derive the algorithm for EKF, first the discrete nonlinear system and measurement model are expressed as follows:

$$x_{k+1} = f(x_k, u_{k+1}, w_k, k) \quad (3.1.27a)$$

$$\tilde{y}_k = h(x_k, v_k, k) \quad (3.1.27b)$$

where, random variables  $w_k$  and  $v_k$  again represent zeros-mean Gaussian process and measurement noise. In practice the values of the noise  $w_k$  and  $v_k$  are unknown at each step time. However, the state and measurement vector can be defined without considering these values:

$$\tilde{x}_{k+1} = f(\hat{x}_k, u_{k+1}, 0, k) \quad (3.1.28a)$$

$$\tilde{y}_k = h(\tilde{x}_k, 0, k) \quad (3.1.28b)$$

The main difference between the linear and extended Kalman filter is in use of the linearized system and measurement model on the steps of the filtering algorithm. The linearization is done by using first-order Taylor series expansion. The first-order expansion of the system and measurement model is given as follows:

$$f(x_k, u_{k+1}, k) \cong f(\bar{x}_k, u_{k+1}, k) + \left. \frac{\partial f}{\partial x} \right|_{\bar{x}_k} [x_k - \bar{x}_k] \quad (3.1.29a)$$

$$h(x_k, k) \cong h(\bar{x}_k, k) + \left. \frac{\partial h}{\partial x} \right|_{\bar{x}_k} [x_k - \bar{x}_k] \quad (3.1.29b)$$

The propagation of the current estimate and covariance matrix are done by using the following equations:

$$\hat{x}_{k+1}^- = \hat{x}_k^+ + \int_k^{k+1} f_k(\hat{x}_k^+, k) dt = (I + F_k \cdot dt) \hat{x}_k^+ \quad (3.1.30)$$

$$P_{k+1}^- = (I + F_k \cdot dt) P_k^+ (I + F_k \cdot dt)^T + Q \quad (3.1.31)$$

where;

$$F_k = \frac{\partial f_k(\hat{x}_k^+, k)}{\partial \hat{x}_k^+} \quad (3.1.32)$$

Then Kalman gain  $K_k$  is computed when the measurement is available. In this computation the linearized measurement model is used:

$$K_k = P_k^- H_k^T [H_k P_k^- H_k^T + R_k]^{-1} \quad (3.1.33)$$

$$H_k = \frac{\partial h_k(\hat{x}_{k+1}^-, k)}{\partial \hat{x}_{k+1}^-} \quad (3.1.34)$$

In order to determine the error between the actual measurement and expected measurement the innovation step is executed:

$$e_k = \tilde{y}_k - H \hat{x}_{k+1}^- \quad (3.1.35)$$

Finally the expressions that provide the state update and covariance update is given as follows:

$$\hat{x}_{k+1}^+ = \hat{x}_{k+1}^- - K_k e_k \quad (3.1.36)$$

$$P_{k+1}^+ = [I - K_k H_k] P_{k+1}^- \quad (3.1.37)$$

The following Table 3-3 summarizes the procedures of the EKF. First the initialization is done for both state and covariance matrix. Then, Kalman gain is computed when the measurement is available. After computing the error between the real measurements and expected measurements, the state update and covariance update steps are implemented.

**Table 3-3: Discrete-time Extended Kalman Filter [4]**

<b>Model</b>	$x_{k+1} = \Phi_k x_k + \Gamma_k u_k + \Psi_k w_k, \quad w_k \sim N(0, Q_k)$ $\tilde{y}_k = H_k x_k + v_k, \quad v_k \sim N(0, R_k)$
<b>Initialize</b>	$\hat{x}(t_0) = \hat{x}_0$ $P_0 = E\{\tilde{x}(t_0)\tilde{x}^T(t_0)\}$
<b>Gain</b>	$K_k = P_k^- H_k^T [H_k P_k^- H_k^T + R_k]^{-1}$
<b>Update</b>	$\hat{x}_k^+ = \hat{x}_k^- - K_k [\tilde{y}_k - H_k \hat{x}_k^-]$ $P_k^+ = [I - K_k H_k] P_k^-$
<b>Propagation</b>	$\hat{x}_{k+1}^- = \Phi_k \hat{x}_k^+ + \Gamma_k u_k$ $P_{k+1}^- = \Phi_k P_k^+ \Phi_k^T + \Psi_k Q_k \Psi_k^T$

It is clear that extended Kalman filter works well only in the region where the first-order Taylor series linearization sufficiently approximates the nonlinear behavior of the system. For this reason, when the estimated initial state is far from the true state, instabilities may occur in estimation process. To overcome these instabilities EKF can be reconfigured by adding the second-order terms in Taylor series, but in that case the computational burden becomes important factor. Therefore in practice this standard EKF has remained the most popular method for nonlinear estimation problems. Other filters (like Unscented and Particle Kalman filters) are investigated only when the performance of the standard EKF is not sufficient, and the quantity or the performance of the sensors is limited [4].

In this thesis EKF is used for satellite attitude determination algorithms and several sensor measurements are fused through EKF. The details about this system are given in the following sub-chapters. However, for a satellite test setup system, it is experienced that the performance of the EKF is insufficient because of the constraint on the sensor types used. Therefore the Unscented Kalman filter (UKF) algorithm is studied on this test setup system. The details about the satellite test setup and UKF are presented in Chapter 4.

### **3.1.4 Filter Tuning**

The performance of the Kalman filter depends on the filter tuning: the selection of the covariances matrices  $P_0$ ,  $Q$  and  $R$ . Filter tuning has two main objectives: to obtain maximum estimation accuracy and to converge to an accurate estimate timely [3]. The  $P_0$  matrix determines the rapidity of the initial convergence and this matrix has no contribution on the steady-state performance of the filter. A  $P_0$  matrix with large entries, compared to the  $Q$  and  $R$ , provide a rapid initial convergence on estimation. In filter, the tradeoff between the rapid tracking of disturbance noise induced state variations is determined by the selection of the covariance matrices  $Q$  and  $R$  [3]. These matrices filter also the measurement noises. The  $Q$  and  $R$  also determine the filter stability in steady-state condition. Generally the values of  $Q$  is selected as the one hundredth or one thousandth of the  $P_0$ ; and the measurement noise level determines the value of  $R$  matrix.

## **3.2 Satellite Attitude Determination System Structure**

This section presents Kalman filter based satellite Attitude Determination System (ADS) structure that processes the sensor measurements to obtain attitude knowledge of the spacecraft. The block diagram of the ADS constituted for the hypothetical LEO satellite is given in Figure 3-1.

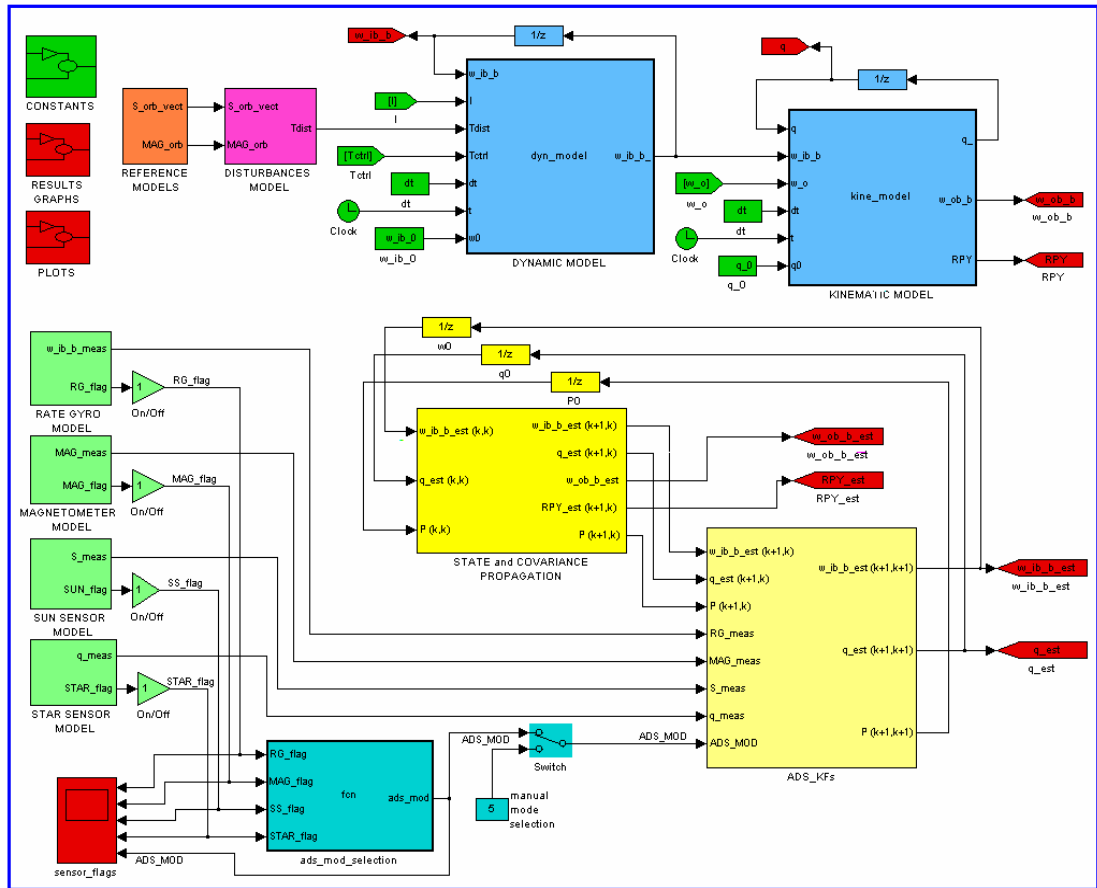


**Figure 3-1: Satellite Attitude Determination Block Diagram**

In this system the standard extended Kalman filter is applied to the sensor outputs in order to fuse different types of measurements and to acquire the angular rates and the attitude of the vehicle. The sensor packet of this system contains rate gyroscopes, magnetometers, sun sensors and a star sensor (see Section 2.4).

ADS contains six different modes which are created with respect to the different sensors combinations by considering sensor outputs rates and sensor availability at different orbital positions and at different mission phases (coarse or accurate attitude determination). For instance, the initial detumbling phase of the satellite after the separation from the launcher is taken into consideration. During this phase the only sensor can be used is the magnetometer and the main aim is to damp the satellite's motion, to control the angular rates. For this reason an attitude determination mode that estimates satellite's angular rates is prepared. Furthermore, when the star sensor

is exposed to the Sun lights directly, it is not possible to obtain measurements from star sensor. For this reason during this period star sensor is closed and attitude estimation filters are fed by other sensors measurements. On the other hand, when satellite is in the eclipse of the Earth, it is not possible to use Sun sensor. During the eclipse periods star sensor provides accurate attitude measurements by working together with the rate gyroscopes and the magnetometer.

The modes prepared for the satellite ADS, the function of the related mode, the sensor used and the state estimated are summarized in the following Table 3-4.

**Table 3-4: Satellite ADS Modes**

<b>Function</b>	<b>ADS Mode</b>	<b>Sensor Used</b>	<b>Estimated State Vector</b>
Angular Rate Estimation:	Mode-1	Magnetometer	$\hat{x} = \hat{\omega}_{OB}^B$
Coarse Full State Estimation:	Mode-2	Rate Gyros	$\hat{x} = [\hat{\omega}_{IB}^B \quad \hat{q}]^T$
Coarse Full State Estimation:	Mode-3	Rate Gyros + Magnetometer	$\hat{x} = [\hat{\omega}_{IB}^B \quad \hat{q}]^T$
Coarse Full State Estimation:	Mode-4	Rate Gyros + Sun Sensor	$\hat{x} = [\hat{\omega}_{IB}^B \quad \hat{q}]^T$
Accurate Full State Estimation:	Mode-5	Rate Gyros + Magnetometer + Sun Sensor	$\hat{x} = [\hat{\omega}_{IB}^B \quad \hat{q}]^T$
Accurate Full State Estimation:	Mode-6	Rate Gyros + Star Sensor	$\hat{x} = [\hat{\omega}_{IB}^B \quad \hat{q}]^T$

In the ADS structure, sensor availability is flagged for each sensor. Related flag values is equal to one when sensor is available and give an outputs, otherwise it gives always zeros values. Furthermore, a sub-module named *ADS mode selection* is prepared in order to select suitable ADS mode depending on the sensor availability knowledge's during the orbit navigation. This module output feed the Kalman Filters module and suitable Kalman filter algorithm is run. The details about the ADS modes are given respectively on the following subsections.

### 3.3 Angular Rate Estimation at Detumbling Mode

This section presents an extended Kalman filter algorithm that estimate the approximate angular rate of the satellite from magnetometer measurements. This estimator is planned for the initial detumbling phase of the satellite's life after separation from the launcher. The rate gyroscopes normally provide direct measurements of the body angular rate. However, these sensors are rarely used due to their power and cost constraints [2]. For this reason in this phase angular rate estimation is done using only magnetometer measurements. Magnetometers measure the geomagnetic field vector with respect to the satellite's body. The rate of change of these vectors relative to the body axes are used to extract the body angular rates. In the following explanations, first the system model is given. Then, measurement model and next the EKF steps are given in details.

#### *System Model:*

The dynamic model given in Eq. (2.1.3) is used in this EKF and this expression can be rewritten as follows. This expression can be also redefined in terms of the orbit referenced body angular rates by using the Eq. (2.1.8) as follows:

$$\dot{\omega}_{IB}^B = I^{-1} \left( -\tilde{\omega}_{IB}^B I \omega_{IB}^B + \tau^B \right) \quad (3.3.1)$$

$$\dot{\omega}_{OB}^B = \dot{\omega}_{IB}^B - \dot{C}_O^B \omega_{IO}^O = I^{-1} \left( -\tilde{\omega}_{IB}^B I \omega_{IB}^B + \tau^B \right) - \dot{C}_O^B \omega_{IO}^O \quad (3.3.2)$$

The last term in the Eq. (3.3.2),  $\dot{C}_O^B \omega_{IO}^O$ , is normally in the same order of magnitude as the disturbance torques. Therefore, it is modeled as system noise with the disturbance torques acting on the satellites.

The discrete-time system model which will be used in the EKF can be rewritten as follows:

$$\hat{x}_{k+1}^- = \omega_{OB_{k+1}}^B = \Phi_k \hat{x}_k^+ + \Gamma_k u_k + s_k \quad (3.3.3)$$

with,

$$\Phi_k = (I + F_k \cdot dt) \quad (3.3.4)$$

$$F_k = \frac{\partial f_k(\hat{x}_k^+, k)}{\partial \hat{x}_k^+} \quad (3.3.5)$$

$$\Gamma_k = I^{-1} \cdot dt \quad (3.3.6)$$

$$s_k = N(0, Q) \quad (3.3.7)$$

where  $Q$  is the discrete zero mean system noise covariance matrix

***Measurement Model:***

In EKF, the measurement model is formed by making use of the small-angle approximation of the direction cosine matrix:

$$C_O^B(k) \approx \begin{bmatrix} 1 & \psi & -\theta \\ -\psi & 1 & \phi \\ \theta & -\phi & 1 \end{bmatrix} \quad (3.3.8)$$

By reducing the sampling rate  $dt$ , it is possible to acquire small rotations between two successive sampling instances. Furthermore, it can be assumed almost constant angular rates during sampling period  $k$ , and as a result of this the direction cosine matrix can be redefined by using these small roll, pitch and yaw rotation angles as given in the following expression:

$$\begin{aligned} \phi_k &\approx \omega_{OB_x}^B(k) \cdot dt \\ \theta_k &\approx \omega_{OB_y}^B(k) \cdot dt \\ \psi_k &\approx \omega_{OB_z}^B(k) \cdot dt \end{aligned} \quad (3.3.9)$$

$$C_O^B(k) \approx I_{3 \times 3} + \Lambda \{ \omega_{OB}^B(k) \} \quad (3.3.10)$$

$$\Lambda\{\omega_{OB}^B(k)\} = \begin{bmatrix} 0 & \omega_{OB_z}^B(k).dt & -\omega_{OB_y}^B(k).dt \\ -\omega_{OB_z}^B(k).dt & 0 & \omega_{OB_x}^B(k).dt \\ \omega_{OB_y}^B(k).dt & -\omega_{OB_x}^B(k).dt & 0 \end{bmatrix} \quad (3.3.11)$$

In this algorithm, the relationship between two successive magnetic field measurement vectors is taken as the angular rate measurement and this relation can be formulated as follows:

$$v_{MAG}(k) = C_O^B(k).v_{MAG}(k-1) \quad (3.3.12)$$

The measurement model defined for these successive measurements is defined as:

$$\tilde{y}(k) = \delta v_{MAG} = H(k)x(k) + m(k) \quad (3.3.13)$$

with,  $m(k) = N(0, R)$  and  $R$  is the discrete zero mean measurement noise covariance matrix.

Finally the measurement matrix used in EKF is derived by using the following steps:

$$\begin{aligned} \delta v_{MAG} &= v_{MAG}(k) - v_{MAG}(k-1) \\ &= C_O^B(k).v_{MAG}(k-1) - v_{MAG}(k-1) \\ &= [C_O^B(k) - I_{3 \times 3}]v_{MAG}(k-1) \\ &= \Lambda\{\omega_{OB}^B(k)\}.v_{MAG}(k-1) \end{aligned} \quad (3.3.14)$$

$$\begin{aligned} H &= \frac{\partial(\Lambda.v_{MAG}(k-1))}{\partial \omega_{OB}^B} \\ &= \begin{bmatrix} 0 & -v_{MAG_z}(k-1).dt_{meas} & v_{MAG_y}(k-1).dt_{meas} \\ v_{MAG_z}(k-1).dt_{meas} & 0 & -v_{MAG_x}(k-1).dt_{meas} \\ -v_{MAG_y}(k-1).dt_{meas} & v_{MAG_x}(k-1).dt_{meas} & 0 \end{bmatrix} \end{aligned} \quad (3.3.15)$$

### ***Extended Kalman Filter Algorithm:***

Here, the EKF steps for ADS Mode-1 are given. Actually these explanations are just a repetition of the algorithm given at Section 3.1.3 for EKF. The first two steps are running each sampling time and when the measurements come from the magnetometer the following steps are executed.

1. *State vector propagation* using Eq. (3.3.2)

$$\hat{x}_{k+1}^- = \Phi_k \hat{x}_k^+ + \Gamma_k u_k + s_k$$

2. *Covariance matrix propagation* using Eq. (3.1.31)

$$P_{k+1}^- = \Phi_k P_k^+ \Phi_k^T + Q$$

3. *Kalman Gain computation* using Eq. (3.1.33)

$$K_k = P_k^- H_k^T [H_k P_k^- H_k^T + R_k]^{-1}$$

4. *Innovation computation* using Eq. (3.1.35)

$$e_k = \tilde{y}_k - H \hat{x}_{k+1}^-$$

5. *State Update* using Eq. (3.1.36)

$$\hat{x}_{k+1}^+ = \hat{x}_{k+1}^- - K_k [\tilde{y}_k - H_k \hat{x}_{k+1}^-]$$

6. *Covariance Update* using Eq. (3.1.37)

$$P_{k+1}^+ = [I - K_k H_k] P_{k+1}^-$$

### ***Simulation Results:***

The simulation of the Kalman Filter Based Satellite ADS is run for Mode-1 for 20 minutes at 1 Hz sampling time and the results that show the performance of the estimation are given in the following figures. In this simulation sampling time for the magnetometer measurements is also taken as 1 Hz.

The real and estimated body angular rates and estimation errors can be seen in the following Figure 3-2. These results show that the estimation error does not exceed  $0.2^\circ/\text{sec}$  for all three components of the angular rates.

In order to point out the performance of the Mode-1, Monte Carlo analysis is also performed to the system. The results of the Monte Carlo analysis provides to determine the statically distribution characteristics of the estimation error. The mean  $\mu_{\hat{x}}$  and standard deviation  $\sigma_{\hat{x}}$  of the estimation errors are computed recursively between the estimation convergence time (150 sec) and simulation end time (1200 sec) for each simulation. In total, 20 simulations are run to determine the estimation performance. The results obtained for each simulation are given in the Figure 3-3. The results given in the Table 3-5 are obtained by computing the mean values of  $\mu_{\hat{x}}$  and  $\sigma_{\hat{x}}$  obtained at the end time for each simulation.

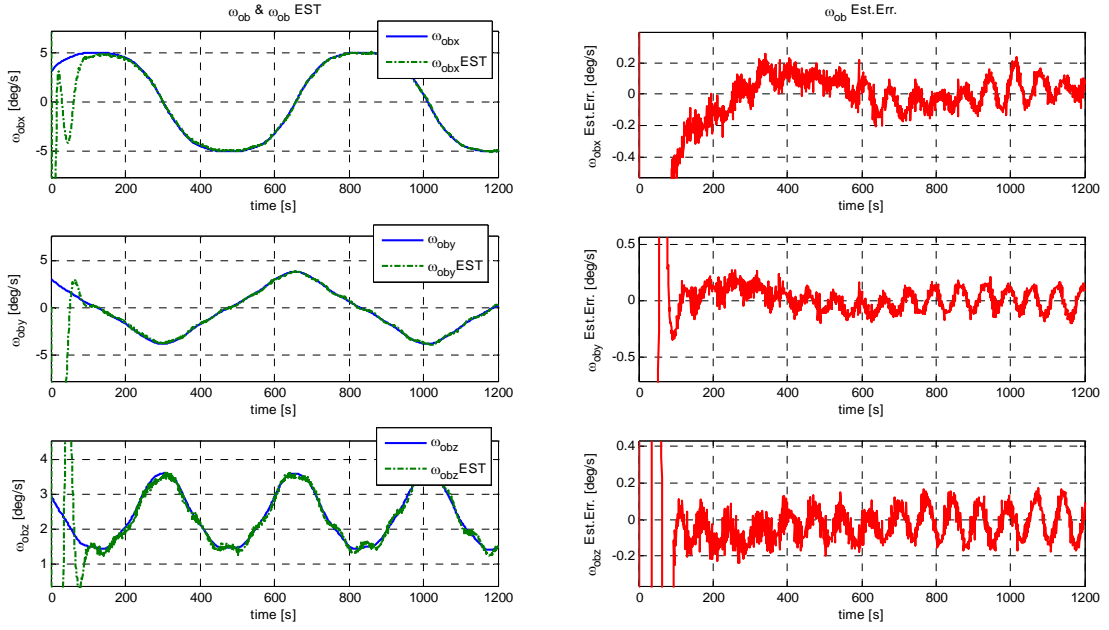


Figure 3-2: Mode-1 Real and Estimated Angular Rates

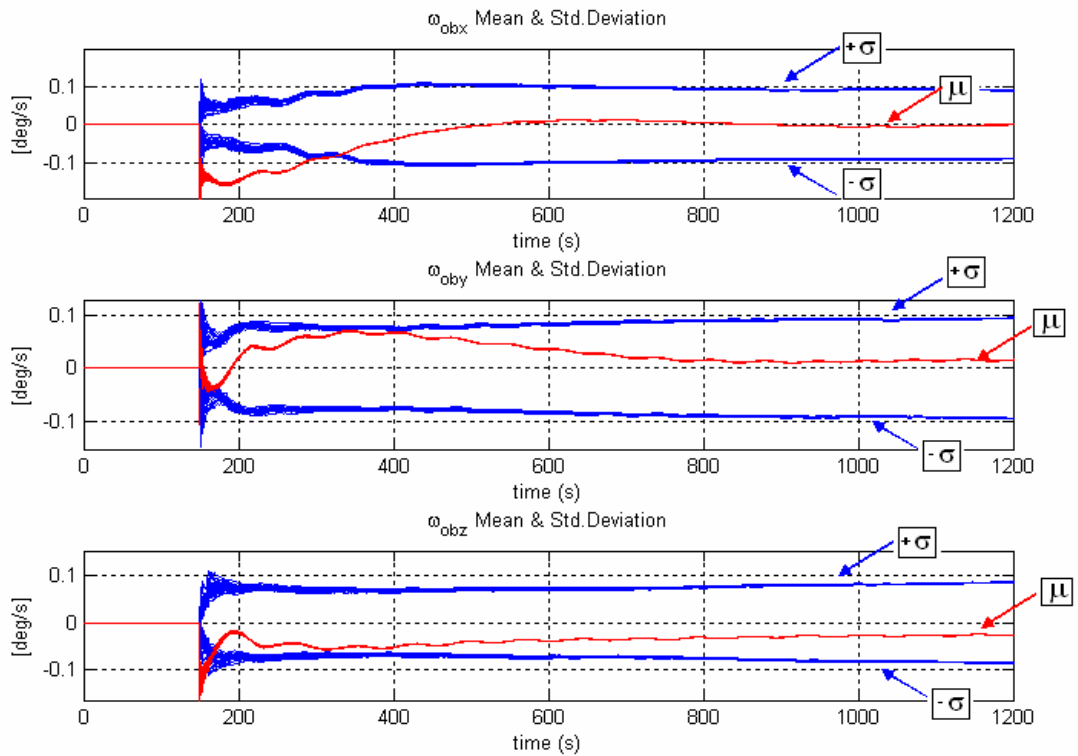


Figure 3-3: Mode-1 Std. Dev. and Mean of the Angular Rate Estimation Error

**Table 3-5: Mode-1 Statistical Results of the Estimation Error**

	$\mu_{\hat{x}} (^{\circ}/\text{sec})$	$\sigma_{\hat{x}} (^{\circ}/\text{sec})$
$\hat{\omega}_{OB\_X}^B \text{ err.}$	0.000	0.090
$\hat{\omega}_{OB\_Y}^B \text{ err.}$	0.016	0.094
$\hat{\omega}_{OB\_Z}^B \text{ err.}$	-0.026	0.085

Consequently, from the results of Mode-1 given above, it is observed that the estimated parameters converge to the real one with an acceptable accuracy and this convergence time is approximately 150 seconds. The estimation error after the convergence is in the band interval of  $\pm 0.2^{\circ}/\text{sec}$ . Regarding to the statistical computations, some amount of bias is seen on the estimation of  $\omega_{OB\_Y}^B$  and  $\omega_{OB\_Z}^B$ ; however, the standard deviation for all three components of the  $\omega_{OB}^B$  is about approximately  $0.09^{\circ}/\text{sec}$  and these results shows that Mode-1 perform a successful estimation for detumbling phase of the satellite.

### 3.4 Coarse Full State Estimation

In this section, three EKF based estimators are presented that estimate the inertially referenced body angular rates ( $\omega_{IB}^B$ ) and the attitude (quaternions  $q$ ) of the satellite by using rate gyroscope, magnetometer and sun sensor measurements for suitable coarse attitude determination. These sensor combinations do not require too much power.

All of the three estimators use rate gyros as the inertial sensor while for Mode-2 rate gyro is the only sensor available. Mode-3 includes a magnetometer used as a reference sensor in addition to rate gyros. This latter mode is suitable for the eclipse periods of the satellite. Mode-4 may be used when sun sensor is available. Thus, Mode-4 fuses the measurements from the rate gyros and Sun sensor.

The detailed explanations about these three modes are given in the following sections. First, the system model which is common for all these modes are explained. Then, the measurements models related to the particular ADS modes are given. Finally the simulation results are presented.

***System Model:***

The dynamic and kinematics model given in Eq. (2.1.3) and Eq. (2.1.6) can be rewritten as follows:

$$\dot{\omega}_{IB}^B = I^{-1}(-\tilde{\omega}_{IB}^B I \omega_{IB}^B + \tau^B) \quad (3.3.16)$$

$$\dot{q} = \frac{1}{2} \Omega_{OB}^B q \quad (3.3.17)$$

The discrete-time system model which will be used in the EKF is formulated as follows:

$$\hat{x}_{k+1}^- = \begin{bmatrix} \omega_{IB}^B & q \end{bmatrix}^T = \Phi_k \hat{x}_k^+ + \Gamma_k u_k + s_k \quad (3.3.18)$$

with,  $\Phi_k = (I + F_k \cdot dt)$ ;  $F_k = \partial f_k(\hat{x}_k^+, k) / \partial \hat{x}_k^+$ ;  $\Gamma_k = I^{-1} \cdot dt$  and  $s_k = N(0, Q)$  where  $Q$  is the discrete zero mean system noise covariance matrix as before.

***Measurement Model:***

**Rate gyros** measure directly the inertial referenced body angular rates  $\omega_{IB}^B$ , so the measurement model in discrete-time can be defined as follows:

$$\tilde{y}_{RG}(k) = \tilde{\omega}_{IB_{meas}}^B(k) = h_{RG}(x_k, v_k, k) = H_{RG}(k)x(k) + m_{RG}(k) \quad (3.3.19)$$

with  $x(k) = [\omega_{IB}^B(k) \quad q(k)]^T$  is the state vector,  $H_{RG}(k)$  is the measurement matrix for rate gyros  $H_{RG}(k) = \partial h_{RG}(\hat{x}_{k+1}^-, k) / \partial \hat{x}_{k+1}^-$ . Here,  $m_{RG}(k) = N(0, R_{RG})$  is the discrete zero mean measurement noise with  $R_{RG}$  covariance matrix of the rate gyros. Then the measurement matrix  $H_{RG}$  is:

$$H_{RG} = [I_{3 \times 3} \quad 0_{3 \times 4}] \quad (3.3.20)$$

**Magnetometer** measures directly the magnitude of the magnetic field with respect to the satellite body axis frames (see Section 2.4.3). Magnetic field direction vector expressed in orbital reference frame ( $MAG^O$ ) are computed by using the IGRF model and the measurement model defined in body frame are created by using the rotation matrix from orbit to body.

$$\begin{aligned} \tilde{y}_{MAG}(k) &= MAG_{meas} = C_O^B \cdot MAG^O + v_{MAG} \\ &= h_{MAG}(x_k, v_k, k) = H_{MAG}(k)x(k) + m_{MAG}(k) \end{aligned} \quad (3.3.21)$$

where,  $m_{MAG}(k) = N(0, R_{MAG})$  is the discrete zero mean measurement noise with  $R_{MAG}$  covariance matrix of the magnetometer. The  $H_{MAG}$  is extracted by the linearization of the measurement model as follows:

$$H_{MAG} = [0_{3 \times 3} \quad H1_{MAG} \quad H2_{MAG} \quad H3_{MAG} \quad H4_{MAG}] \quad (3.3.22a)$$

$$H1_{MAG} = 2 \begin{bmatrix} \hat{q}_1 & \hat{q}_2 & \hat{q}_3 \\ \hat{q}_2 & -\hat{q}_1 & \hat{q}_4 \\ \hat{q}_3 & -\hat{q}_4 & -\hat{q}_1 \end{bmatrix} MAG^O \quad (3.3.22b)$$

$$H2_{MAG} = 2 \begin{bmatrix} -\hat{q}_2 & \hat{q}_1 & -\hat{q}_4 \\ \hat{q}_1 & \hat{q}_2 & \hat{q}_3 \\ \hat{q}_4 & \hat{q}_3 & -\hat{q}_2 \end{bmatrix} MAG^O \quad (3.3.22c)$$

$$H3_{MAG} = 2 \begin{bmatrix} -\hat{q}_3 & \hat{q}_4 & \hat{q}_1 \\ -\hat{q}_4 & -\hat{q}_3 & \hat{q}_1 \\ \hat{q}_1 & \hat{q}_2 & \hat{q}_3 \end{bmatrix} MAG^O \quad (3.3.22d)$$

$$H4_{MAG} = 2 \begin{bmatrix} \hat{q}_4 & \hat{q}_3 & -\hat{q}_2 \\ -\hat{q}_3 & \hat{q}_4 & \hat{q}_1 \\ \hat{q}_2 & -\hat{q}_1 & \hat{q}_4 \end{bmatrix} MAG^O \quad (3.3.22e)$$

**Sun sensor** measures the Sun position vector defined in the satellite body axis frames and the unit Sun position vector expressed in orbital reference frame ( $S^O$ ) is computed by using the Sun position model (see Section 2.4.2). The measurement model defined in body frame are formed by using the rotation matrix from orbit to body as follows

$$\begin{aligned} \tilde{y}_{SUN}(k) &= S_{meas} = C_O^B \cdot S^O + v_{SUN} \\ &= h_{SUN}(x_k, v_k, k) = H_{SUN}(k)x(k) + m_{SUN}(k) \end{aligned} \quad (3.3.23)$$

As seen from this last equation, measurement models of the Sun sensor and magnetometer have the same structure. So, the measurement matrix  $H_{SUN}$  can be expressed by rearranging the  $H_{MAG}$  as follows:

$$H_{SUN} = [0_{3 \times 3} \quad H1_{SUN} \quad H2_{SUN} \quad H3_{SUN} \quad H4_{SUN}] \quad (3.3.24a)$$

$$H1_{SUN} = 2 \begin{bmatrix} \hat{q}_1 & \hat{q}_2 & \hat{q}_3 \\ \hat{q}_2 & -\hat{q}_1 & \hat{q}_4 \\ \hat{q}_3 & -\hat{q}_4 & -\hat{q}_1 \end{bmatrix} S^O \quad (3.3.24b)$$

$$H2_{SUN} = 2 \begin{bmatrix} -\hat{q}_2 & \hat{q}_1 & -\hat{q}_4 \\ \hat{q}_1 & \hat{q}_2 & \hat{q}_3 \\ \hat{q}_4 & \hat{q}_3 & -\hat{q}_2 \end{bmatrix} S^O \quad (3.3.24c)$$

$$H3_{SUN} = 2 \begin{bmatrix} -\hat{q}_3 & \hat{q}_4 & \hat{q}_1 \\ -\hat{q}_4 & -\hat{q}_3 & \hat{q}_1 \\ \hat{q}_1 & \hat{q}_2 & \hat{q}_3 \end{bmatrix} S^O \quad (3.3.24d)$$

$$H4_{SUN} = 2 \begin{bmatrix} \hat{q}_4 & \hat{q}_3 & -\hat{q}_2 \\ -\hat{q}_3 & \hat{q}_4 & \hat{q}_1 \\ \hat{q}_2 & -\hat{q}_1 & \hat{q}_4 \end{bmatrix} S^o \quad (3.3.24e)$$

***Extended Kalman Filter Algorithm:***

The EKF used for ADS Mode-2, Mode-3 and for Mode-4 has the same structure with the steps given in Section 3.3 which is based on the algorithm explained in section 3.1.3. The main difference between these ADS modes are the measurement matrix and the measurement noise covariance matrix that is related to the sensors used. In the following equations the measurement and noise covariance matrix for each coarse ADS modes are listed respectively.

$$R_{MOD\_2} = I_{3 \times 3} \cdot R_{RG} \quad (3.3.25)$$

$$H_{MOD\_2} = H_{RG} \quad (3.3.26)$$

$$R_{MOD\_3} = \begin{bmatrix} I_{3 \times 3} \cdot R_{RG} & 0_{3 \times 3} \\ 0_{3 \times 3} & I_{3 \times 3} \cdot R_{MAG} \end{bmatrix} \quad (3.3.27)$$

$$H_{MOD\_3} = \begin{bmatrix} H_{RG} \\ H_{MAG} \end{bmatrix} \quad (3.3.28)$$

$$R_{MOD\_4} = \begin{bmatrix} I_{3 \times 3} \cdot R_{RG} & 0_{3 \times 3} \\ 0_{3 \times 3} & I_{3 \times 3} \cdot R_{SUN} \end{bmatrix} \quad (3.3.29)$$

$$H_{MOD\_4} = \begin{bmatrix} H_{RG} \\ H_{SUN} \end{bmatrix} \quad (3.3.30)$$

***Simulation Results:***

The Satellite ADS simulation is run at 5 Hz sampling time for 300 seconds at each coarse attitude determination modes. Results obtained for each mode are given separately in the following sections. The measurement sampling time for the each sensor also is selected as 5 Hz.

## Mod-2 Results

ADS Mode-2 use only rate gyros measurement to estimate the state vector. The real and estimated states and estimation errors are given respectively in the following Figure 3-4, Figure 3-5 and Figure 3-6.

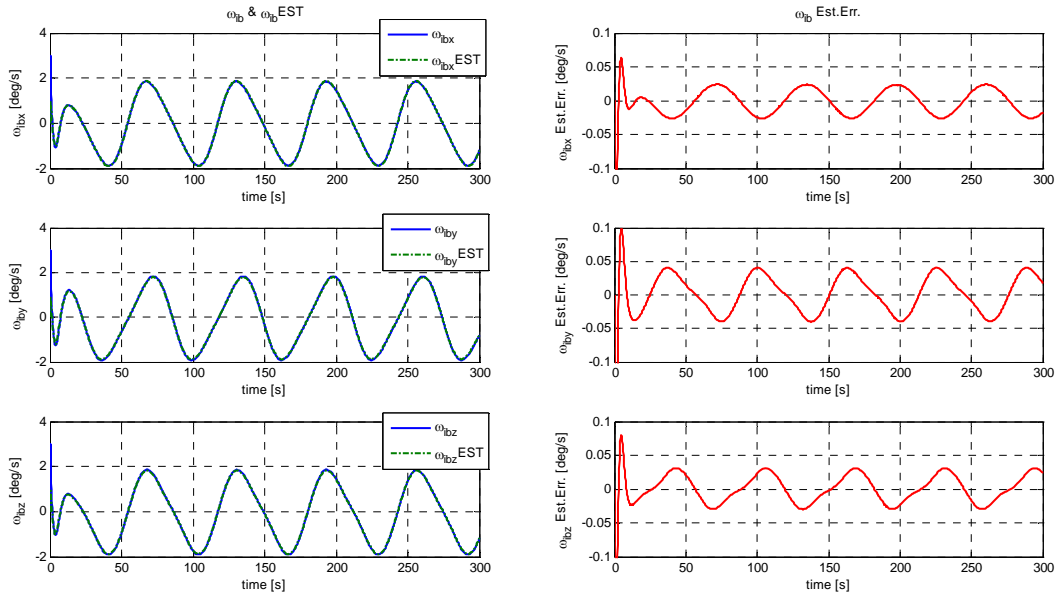


**Figure 3-4: Mode-2 Real and Estimated Angular Rates**

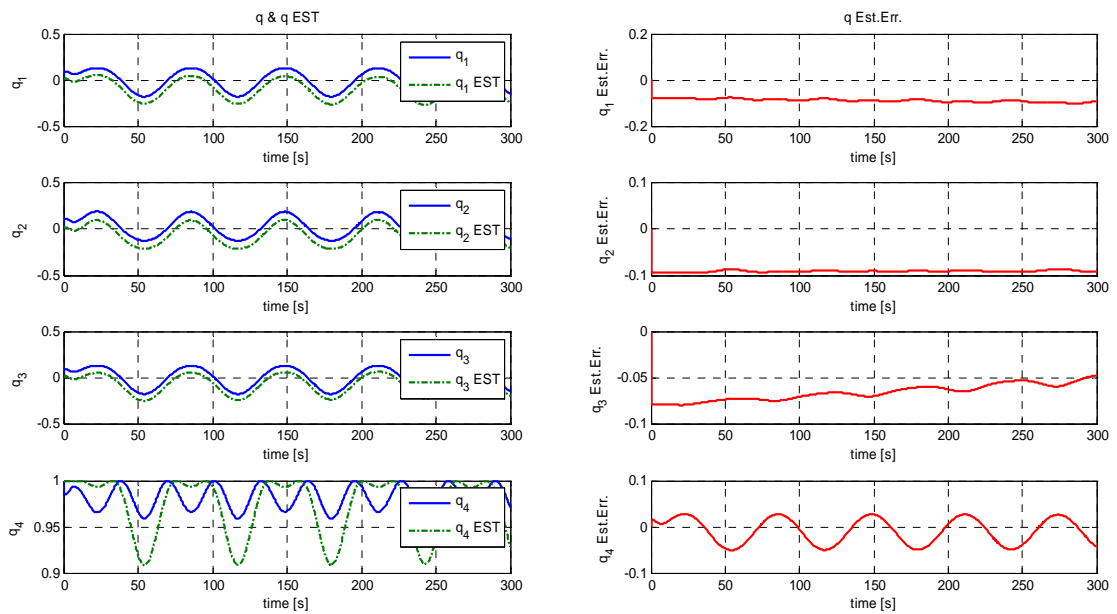


**Figure 3-5: Mode-2 Real and Estimated Quaternions**

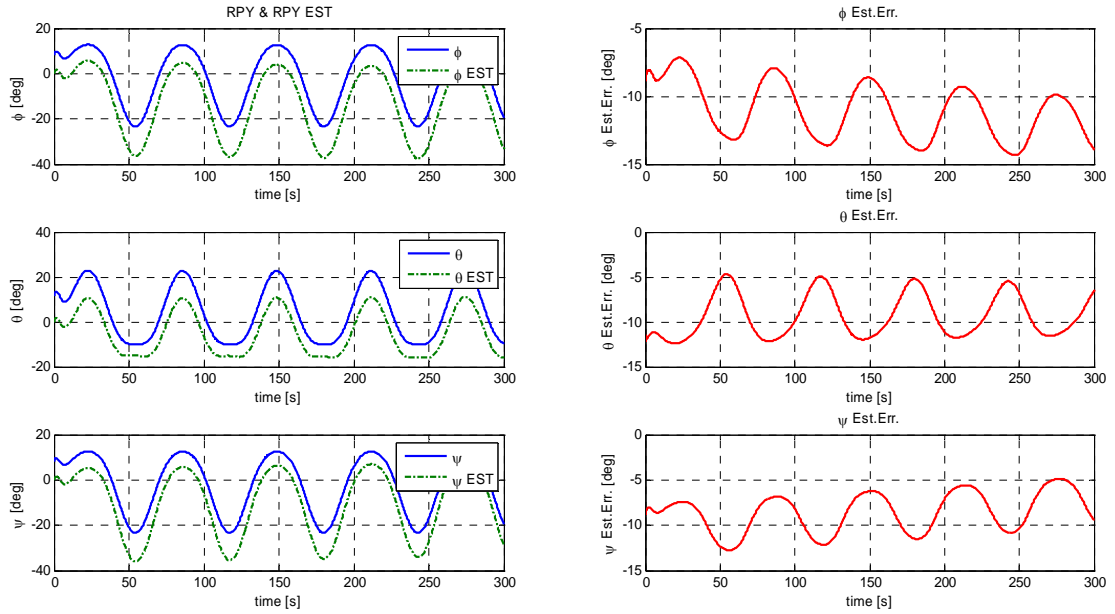


**Figure 3-6: Mode-2 Real and Estimated RPY Angles**

Regarding to the Mod-2's estimation results, it can be clearly seen that it is not possible to accurately estimate the attitude by using only rate gyros measurements when the initial values of the real and estimated states are different. Therefore Monte Carlo analysis is applied only to the estimated angular rates for this Mode-2. The statistical results are taken by repeating the simulation 20 times for Mode-2. The mean  $\mu_{\hat{x}}$ , and the standard deviation  $\sigma_{\hat{x}}$  of the estimation errors are given in the Figure 3-7, Figure 3-8 and Table 3-6.

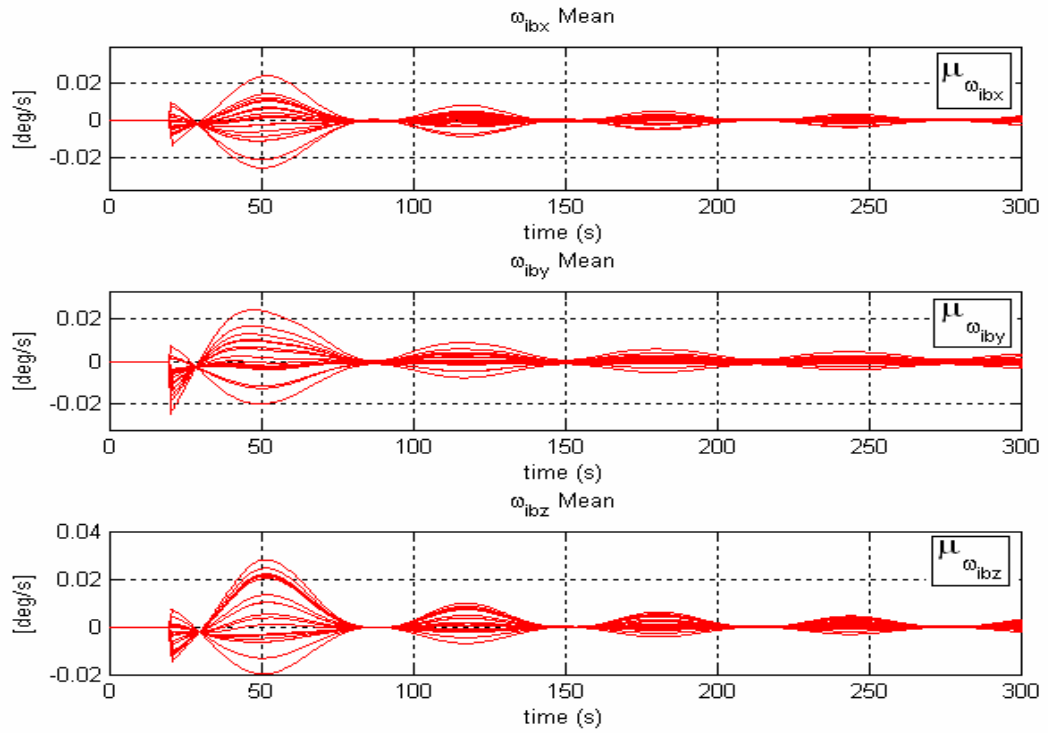


**Figure 3-7: Mode-2 Mean of the Angular Rate Estimation Error**

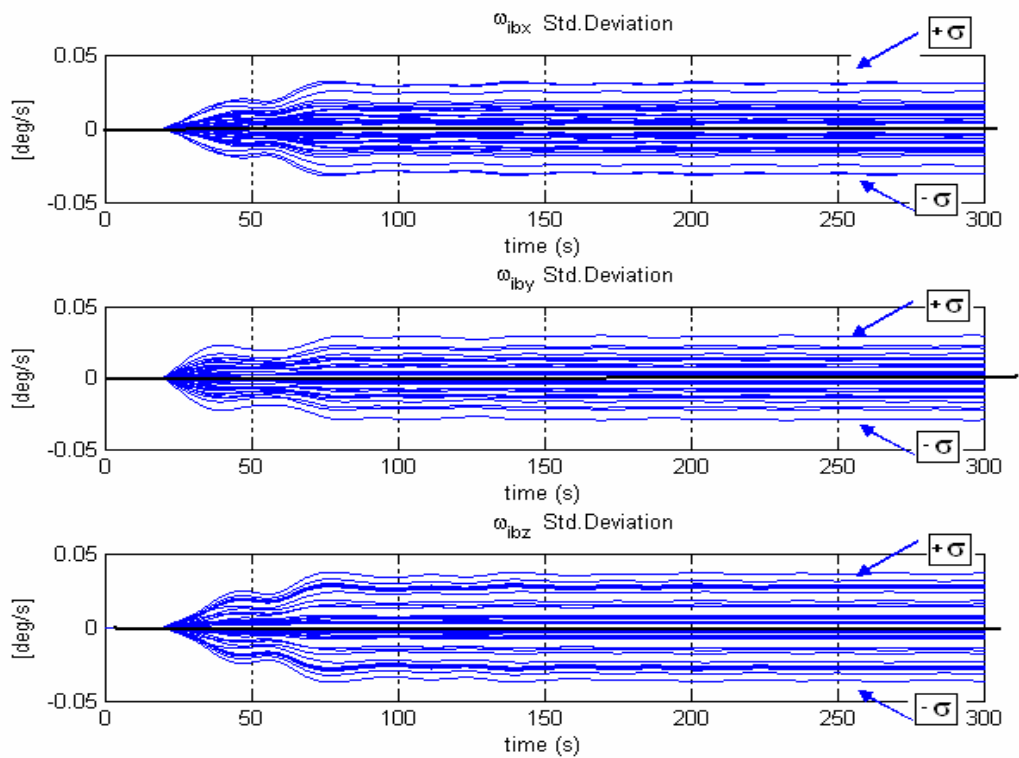


**Figure 3-8: Mode-2 Standard Deviation of the Angular Rate Estimation Error**

**Table 3-6: Mode-2 Statistical Results of the Estimation Error**

	$\mu_{\hat{x}}$ ( $^{\circ}/\text{sec}$ )	$\sigma_{\hat{x}}$ ( $^{\circ}/\text{sec}$ )
$\hat{\omega}_{IB\_X}^B \text{ err.}$	0.000	0.0125
$\hat{\omega}_{IB\_Y}^B \text{ err.}$	0.000	0.0097
$\hat{\omega}_{IB\_Z}^B \text{ err.}$	0.000	0.0163

Consequently, Mode-2 shows a good estimation performance for only angular rate estimation. It is observed that the accurate attitude estimation can not be realized without using a reference sensor. The only possibility to get also good attitude estimation in Mode-2, is to have the same initial values for real and estimated states. Regarding to the results, it is seen that the convergence time for angular rate estimation is approximately 5 seconds. The angular rate estimation error is in the band interval of  $\pm 0.03^{\circ}/\text{sec}$ . From the statistical computations, standard deviation of the estimation error is obtained approximately  $0.015^{\circ}/\text{sec}$ .

### Mod-3 Results

ADS Mode-3 use rate gyros as an inertial sensor and magnetometer as a reference sensor in the estimation of the angular rate and attitude of the satellite. In order to examining the performance of Mode-3, a motion profile containing sinusoidal part followed by a fixed attitude part is used. The initial attitude angles are given as  $\phi = \theta = \psi = 20^{\circ}$ . The real and estimated states and estimation errors under this defined motion profile are given respectively in the following Figure 3-9, Figure 3-10 and Figure 3-11.

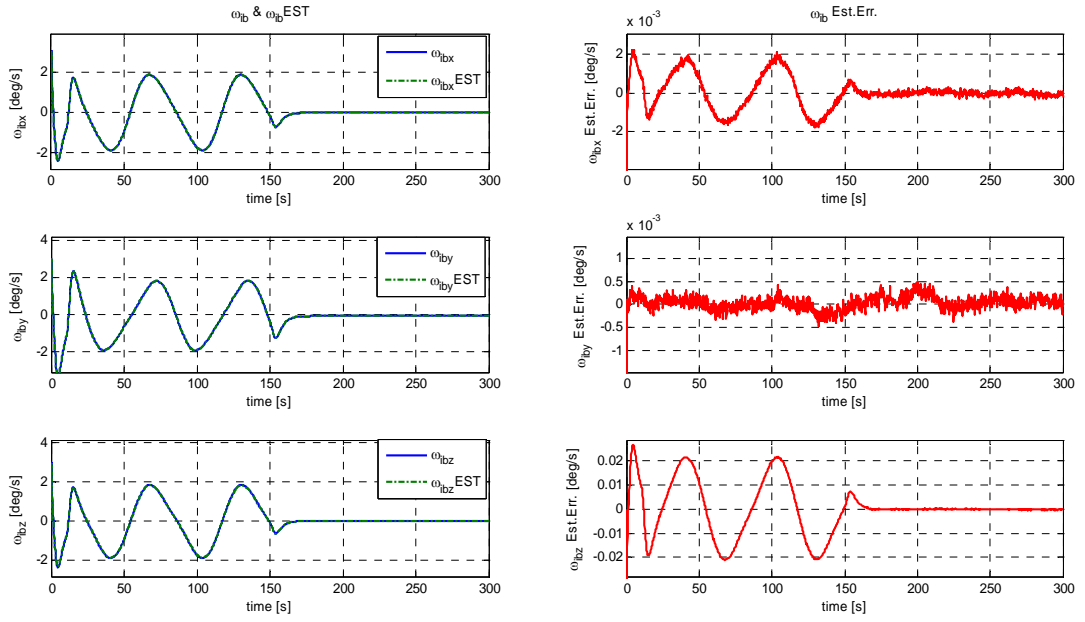


**Figure 3-9: Mode-3 Real and Estimated Angular Rates**

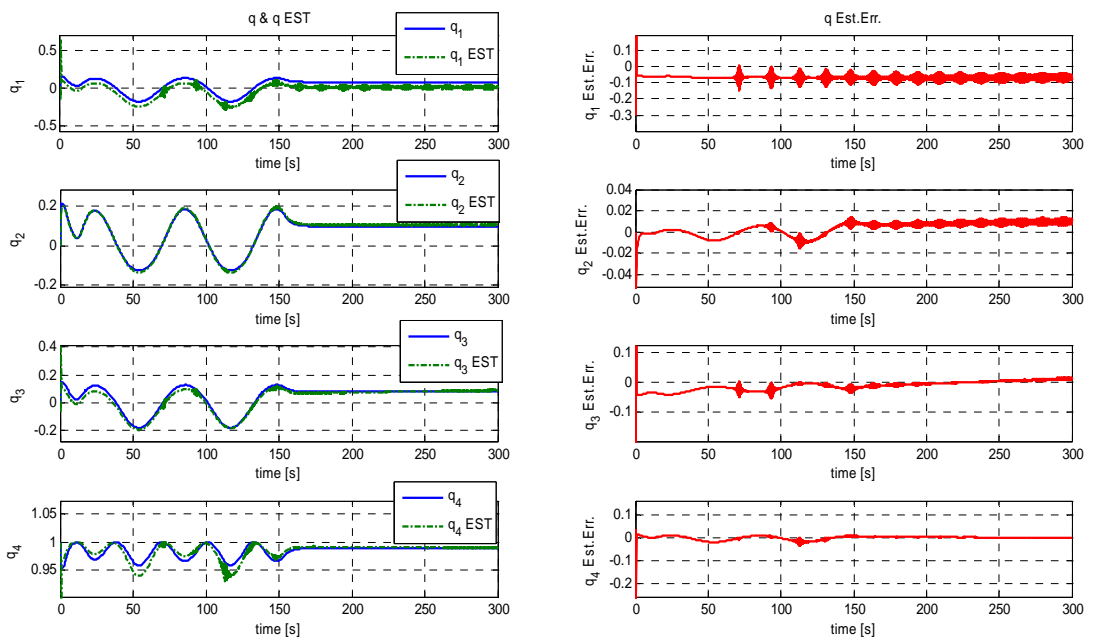


**Figure 3-10: Mode-3 Real and Estimated Quaternions**

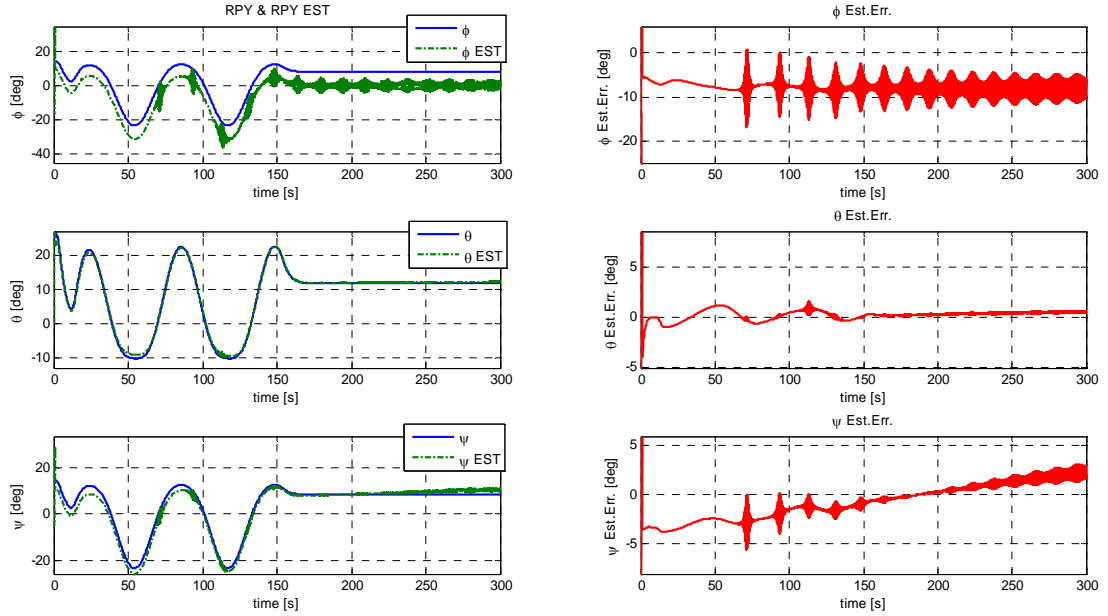


**Figure 3-11: Mode-3 Real and Estimated RPY Angles**

Regarding to the Mod-3's simulation results, it is seen that the performance of the attitude estimation is not successful. The only relatively satisfactory estimation is obtained in pitch angle  $\theta$ , but during the attitude hold motion the estimation start to diverge from the real values. This divergence can be seen also in the yaw angle  $\psi$ . The roll angle  $\phi$  estimation obtained is very noisy. The inaccuracy of attitude estimation has a negative effect on the angular rate estimation. Since the pitch angle estimation is better compared to the other attitude angles' estimation, the  $\hat{\omega}_{IB\_Y}^B$  also is stable. However different estimation error behaviors are obtained for the others angular rates during the sinusoidal changing attitude and fixed attitude profiles.

Monte Carlo analysis is applied and the statistical results are calculated during simulations. Each simulation is repeated 20 times for Mode-3. The mean  $\mu_{\hat{x}}$  and the standard deviation  $\sigma_{\hat{x}}$  values of the estimation errors are given in the following figures and Table 3-7.

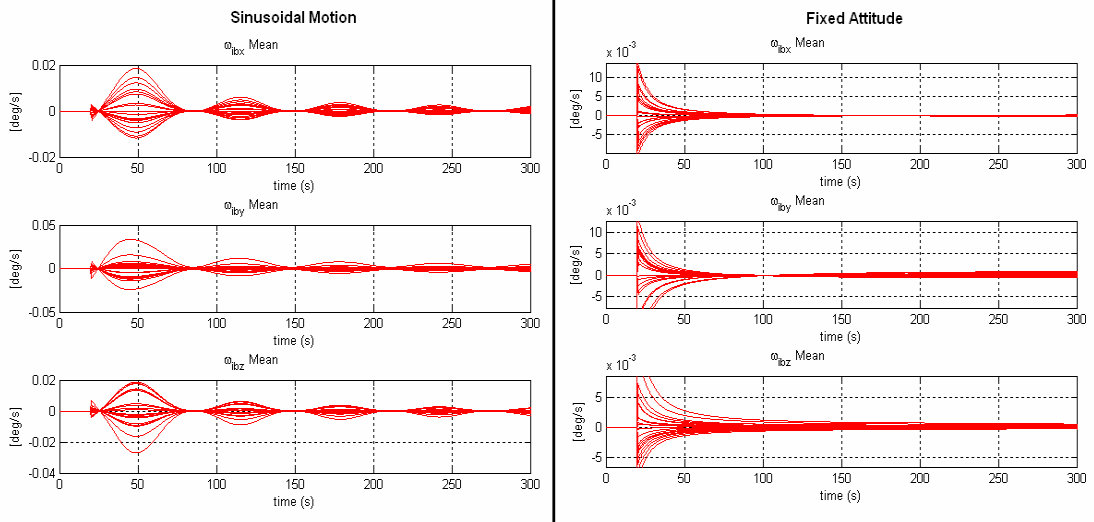


**Figure 3-12: Mode-3 Mean of the Angular Rates Estimation Error**

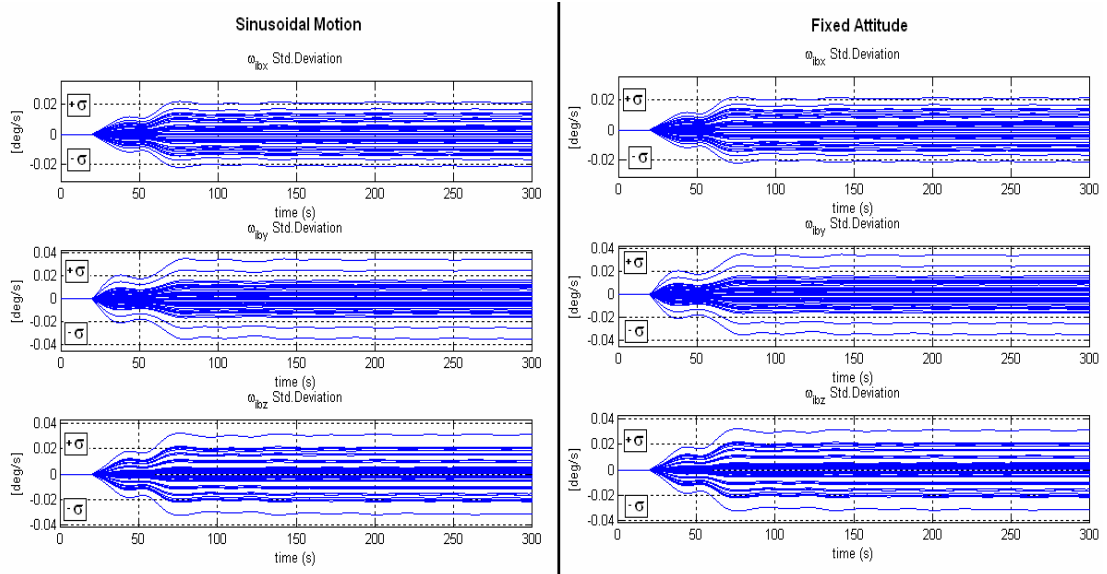


**Figure 3-13: Mode-3 Standard Deviation of the Angular Rates Estimation Error**

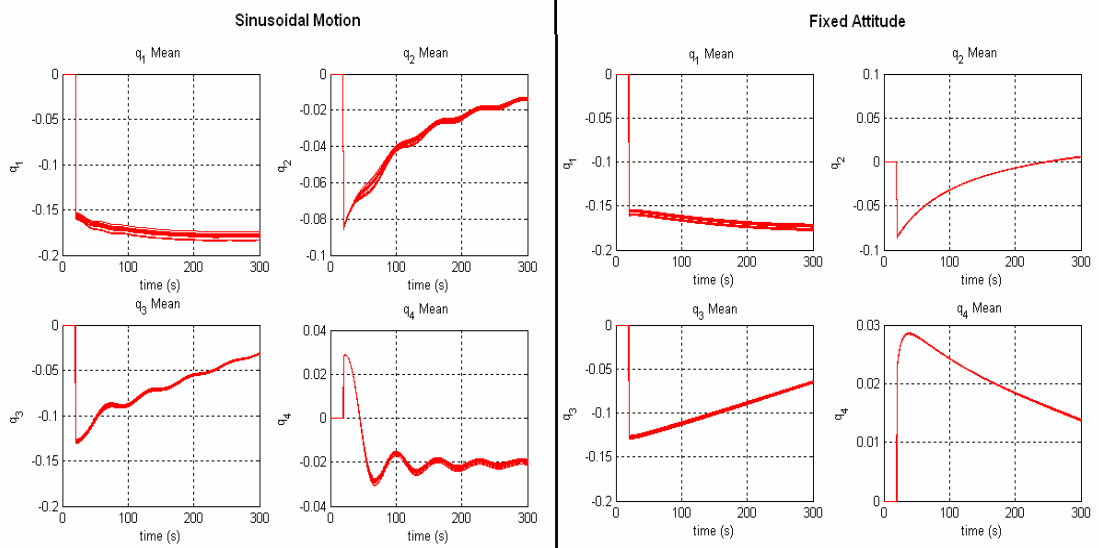


**Figure 3-14: Mode-3 Mean of the Quaternions Estimation Error**

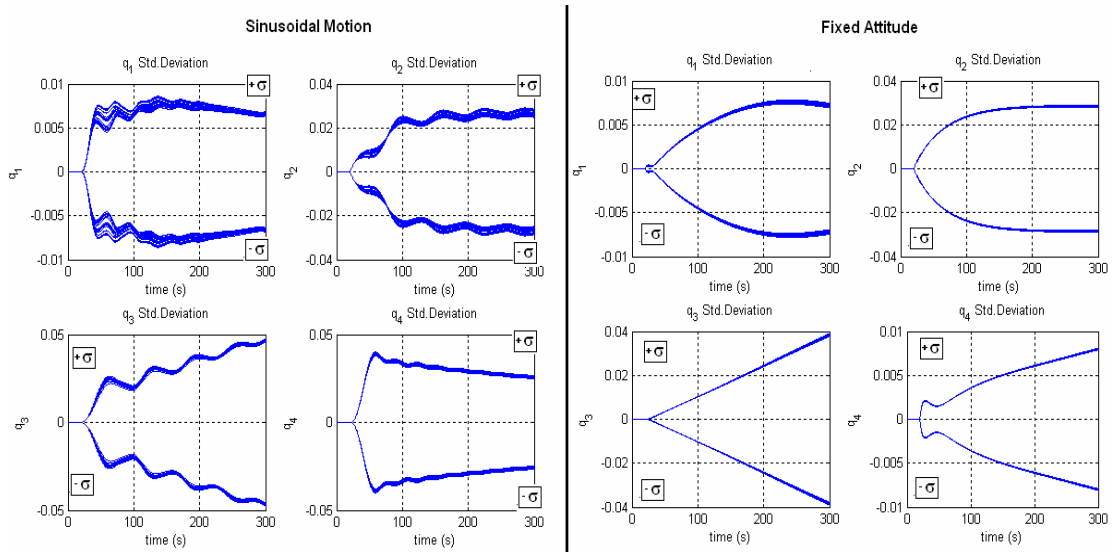


**Figure 3-15: Mode-3 Standard Deviation of the Quaternions Estimation Error**

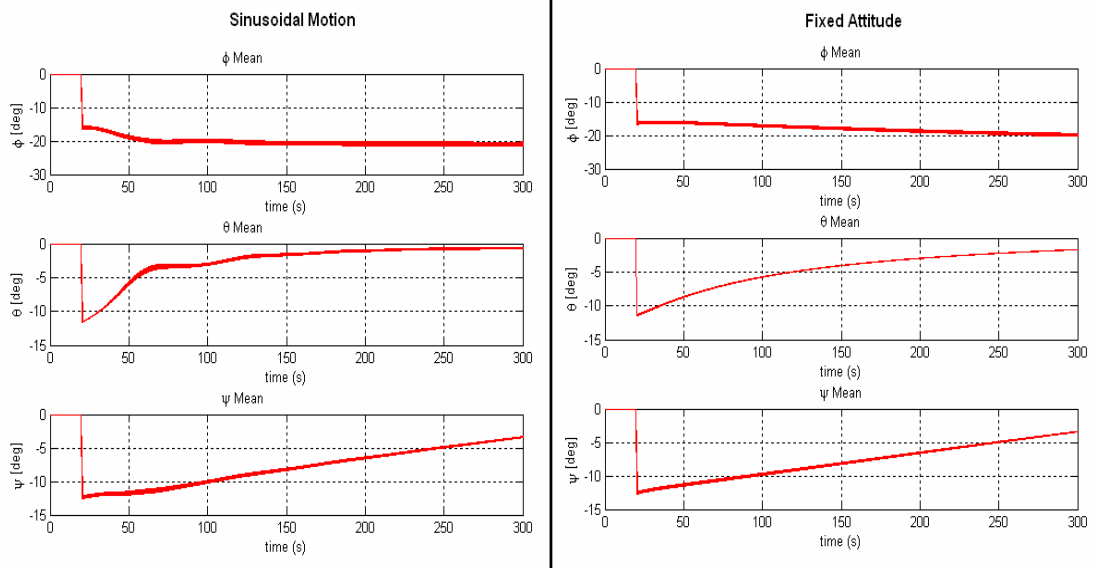


**Figure 3-16: Mode-3 Mean of the RPY Angles Estimation Error**

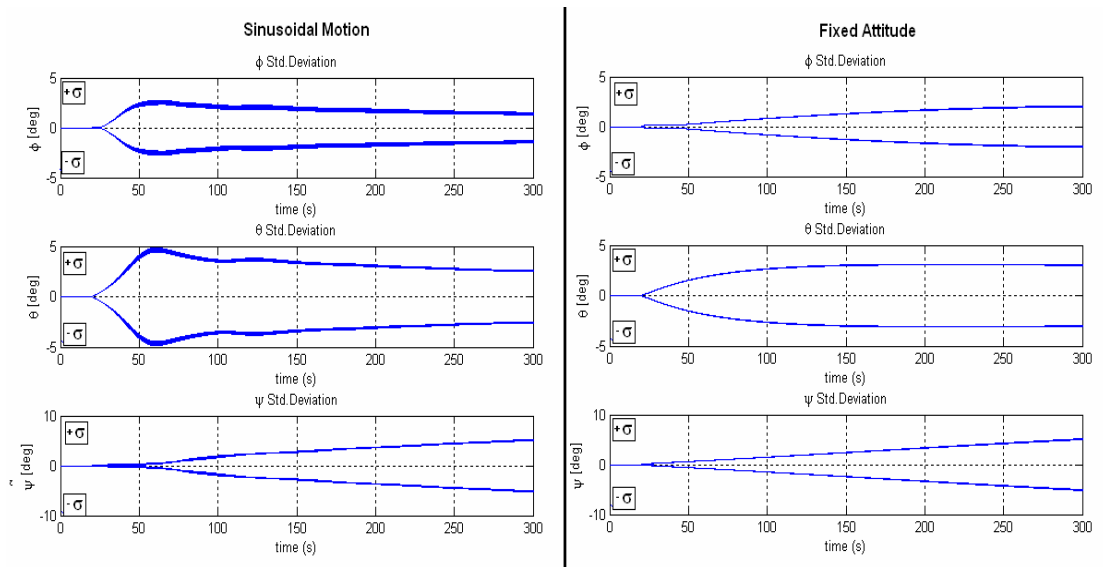


**Figure 3-17: Mode-3 Standard Deviation of the RPY Angles Estimation Error**

**Table 3-7: Mode-3 Statistical Results of the Estimation Error**

	Sinusoidal Motion		Fixed Attitude	
	$\mu_{\hat{x}}$	$\sigma_{\hat{x}}$	$\mu_{\hat{x}}$	$\sigma_{\hat{x}}$
$\hat{X}_{err}$				
$\hat{\omega}_{IB\_X}^B \text{ err. } (^{\circ}/\text{sec})$	0.000	0.0082	0.000	0.0006
$\hat{\omega}_{IB\_Y}^B \text{ err. } (^{\circ}/\text{sec})$	0.000	0.0095	0.000	0.0007
$\hat{\omega}_{IB\_Z}^B \text{ err. } (^{\circ}/\text{sec})$	0.000	0.0108	0.000	0.0005
$\hat{q}_{1err}$	-0.1785	0.0067	-0.1728	0.0072
$\hat{q}_{2err}$	-0.0138	0.0268	0.0057	0.0283
$\hat{q}_{3err}$	-0.0317	0.0467	-0.0645	0.0381
$\hat{q}_{4err}$	-0.0199	0.0256	0.0139	0.0080
$\hat{\phi}_{err} (^{\circ})$	-20.8956	1.4281	-19.6820	2.0353
$\hat{\theta}_{err} (^{\circ})$	-0.6059	2.5354	-1.7041	3.0326
$\hat{\psi}_{err} (^{\circ})$	-3.3871	5.1887	-3.3795	5.0734

Consequently, Mode-3 results point out that the magnetometer is not sufficient to obtain a successful attitude estimation performance. The results of the Monte Carlo analysis also show the estimation performance statistically and it is seen that magnetometer measurements provide better attitude estimation for the pitch and yaw angles. The reason of the bias problem on the roll angle estimation may be the type of the orbit selected for the hypothetical satellite and as this satellite navigates in a nearly polar orbit, the magnetic field measurements may cause accuracy problems on this roll axis which is nearly parallel to the polar axis of the Earth. It can be also expressed that one reference sensor is not sufficient to preserve the convergence in case of the attitude hold motion.

#### **Mod-4 Results**

ADS Mode-4 uses rate gyros as inertial sensors and a Sun sensor as the reference sensor. Sinusoidal changing attitude and fixed attitude motion profiles are used again. The initial attitude angles are given as  $\phi = \theta = \psi = 20^{\circ}$ . The real and estimated states

and estimation errors under this defined motion profile are given respectively in the Figure 3-18, Figure 3-19 and Figure 3-20.

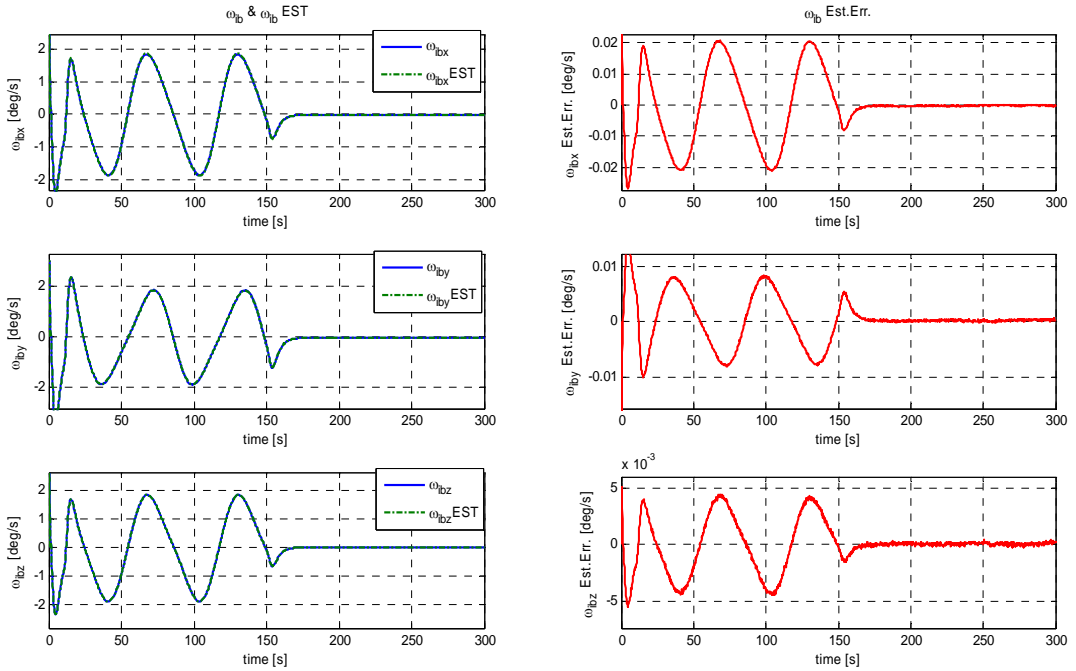


**Figure 3-18: Mode-4 Real and Estimated Angular Rates**

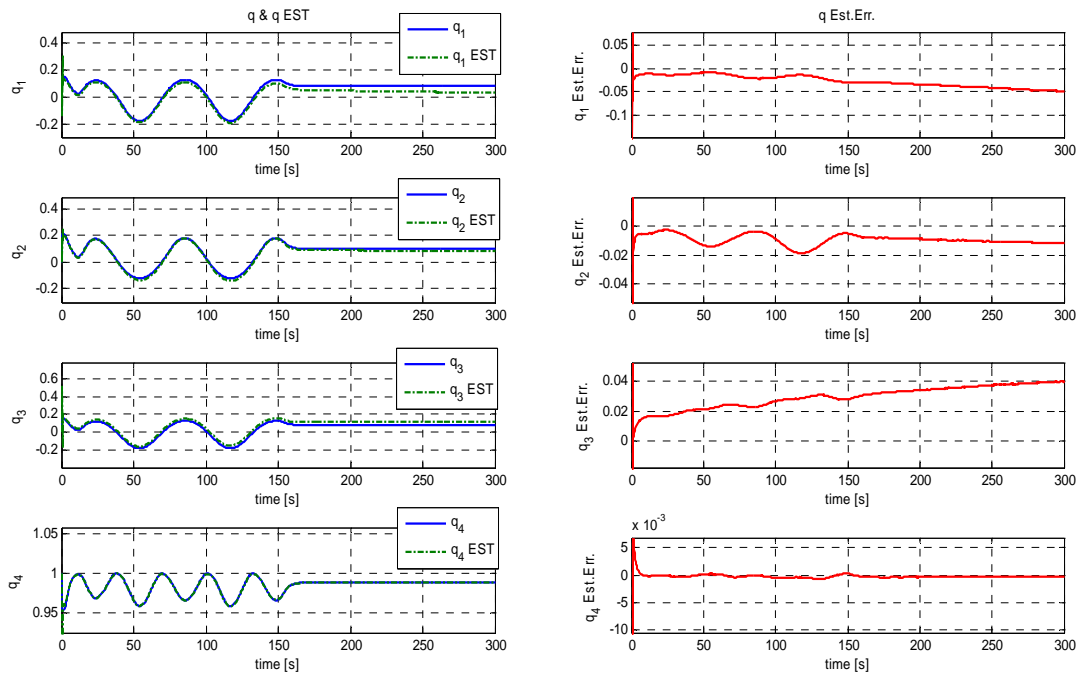


**Figure 3-19: Mode-4 Real and Estimated Quaternions**

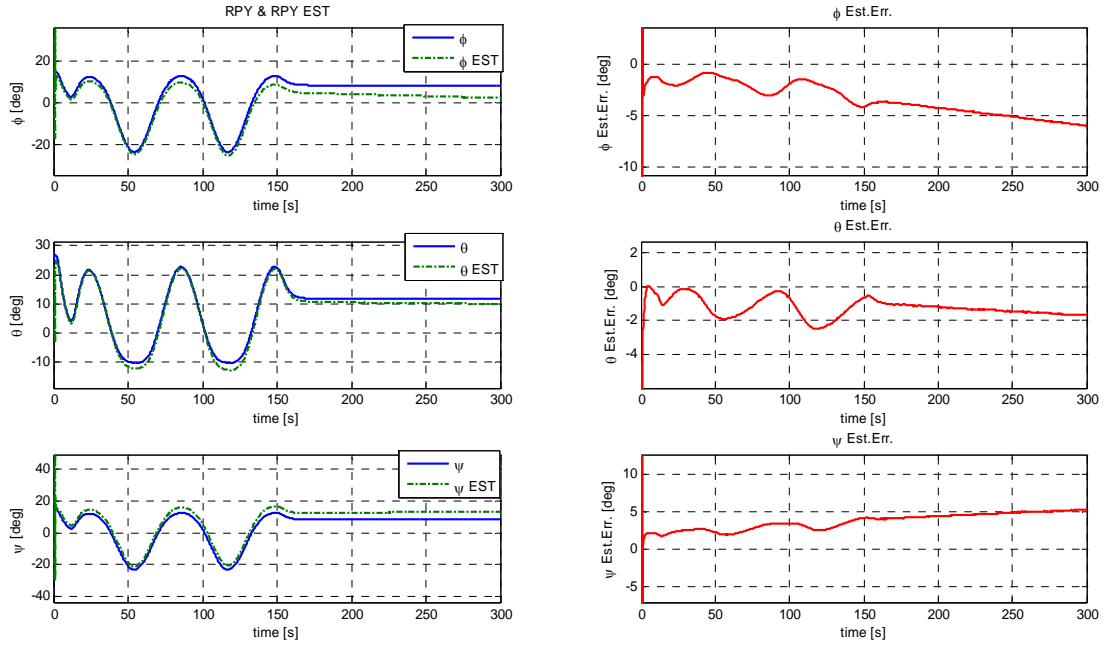


**Figure 3-20: Mode-4 Real and Estimated RPY Angles**

The results of Mode-4 show that by using Sun sensor as a reference source, a sufficient performance for coarse attitude estimation is obtained, since Sun sensors are more accurate sensors than magnetometers. However, the divergence problem for the attitude hold motion can be seen also in Mode-4. This problem can be resolved by using more than one reference sensor in ADS. This situation is studied in Mode-5 below.

Statistical results also are taken by running the Monte Carlo analysis 20 times for Mode-4. The mean  $\mu_{\hat{x}}$  and the standard deviation  $\sigma_{\hat{x}}$  of the estimation errors are given in the following Figure 3-21 to Figure 3-26 and Table 3-8.

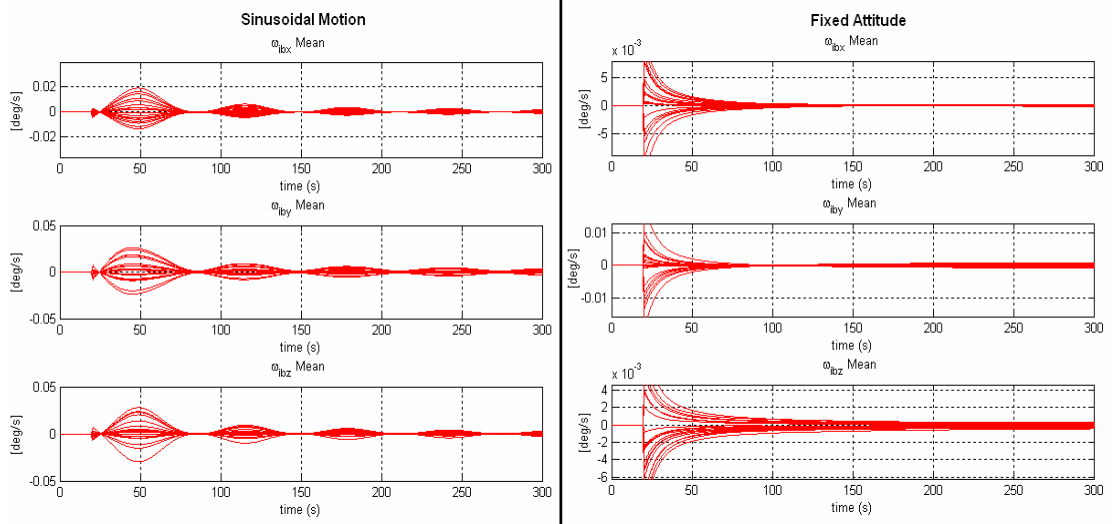


Figure 3-21: Mode-4 Mean of the Angular Rates Estimation Error

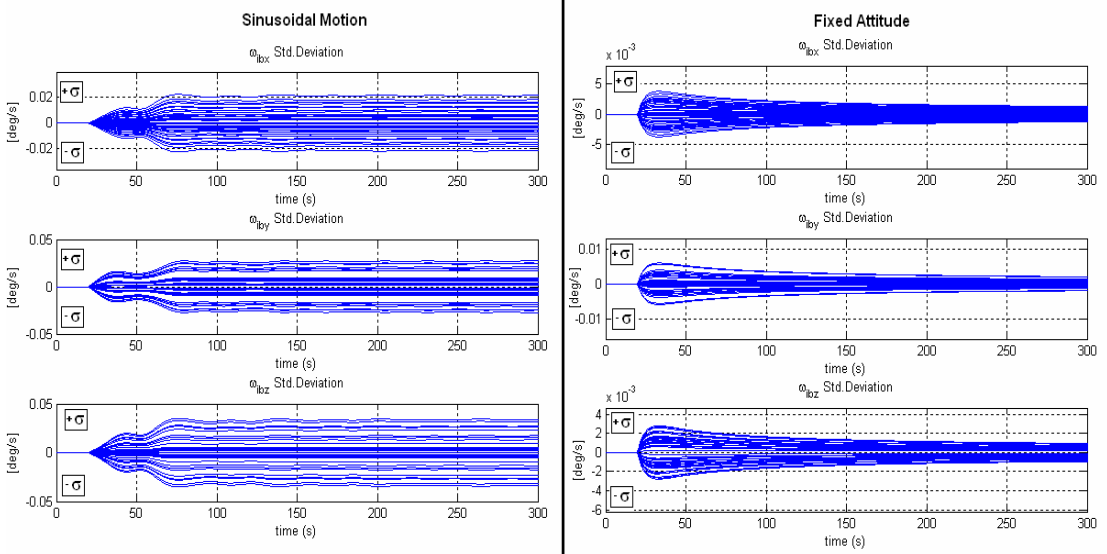
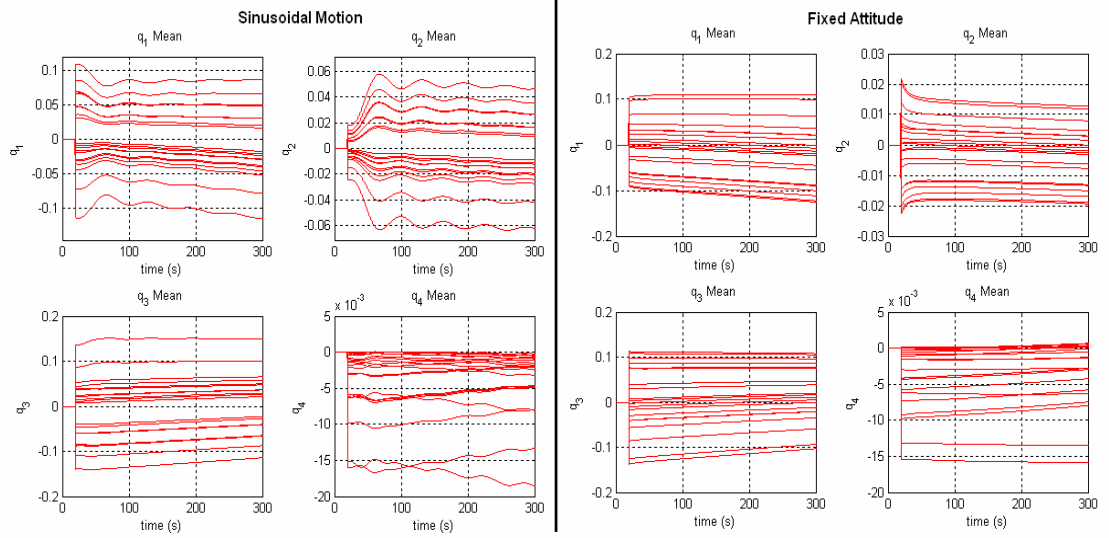
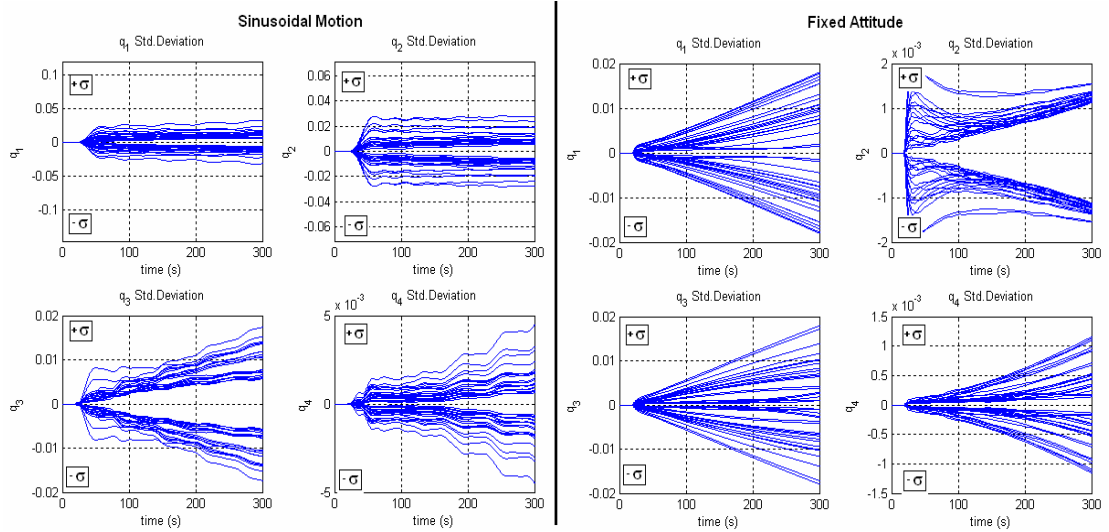


Figure 3-22: Mode-4 Standard Deviation of the Angular Rates Estimation Error



**Figure 3-23: Mode-4 Mean of the Quaternions Estimation Error**



**Figure 3-24: Mode-4 Standard Deviation of the Quaternions Estimation Error**

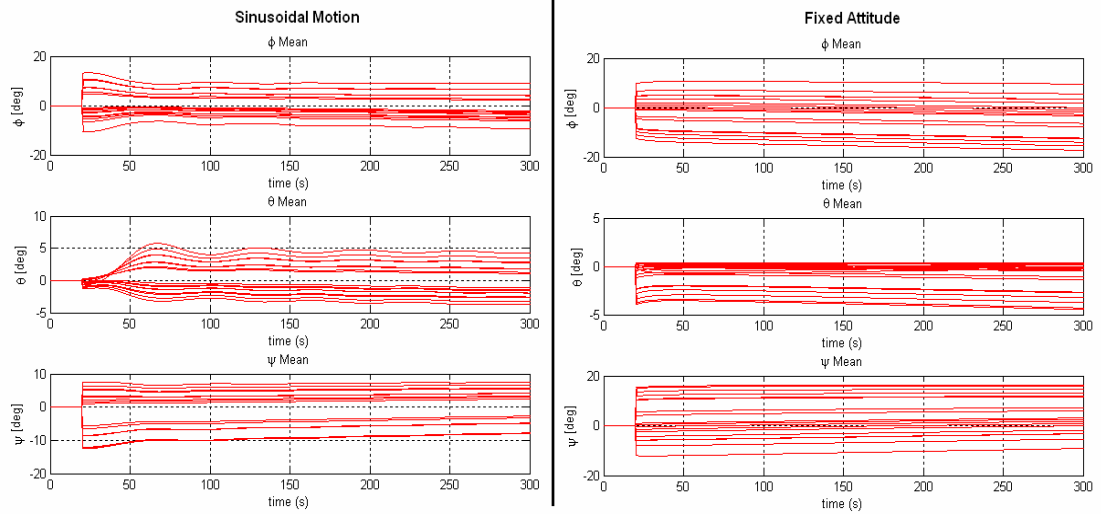


**Figure 3-25: Mode-4 Mean of the RPY Estimation Error**

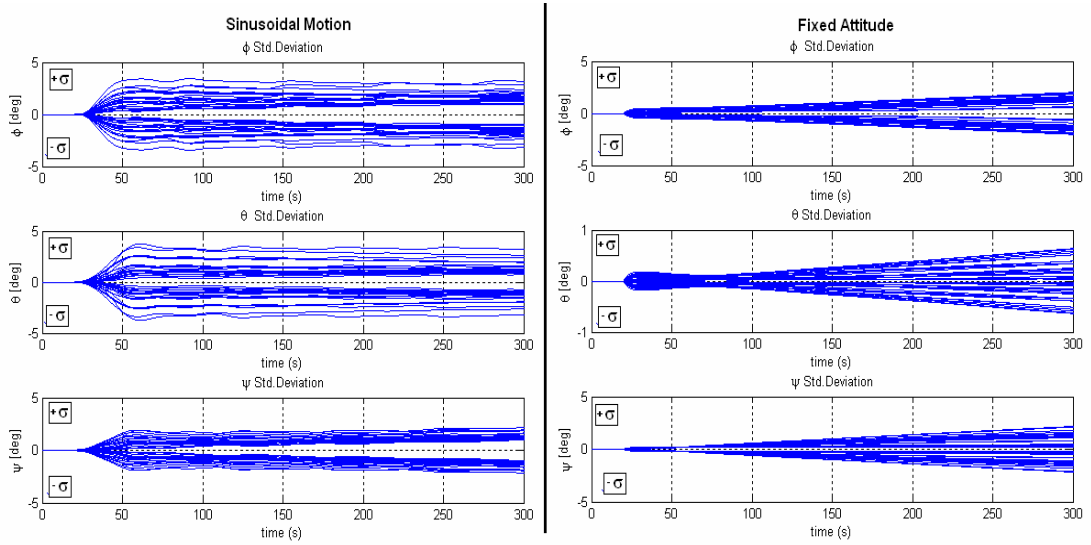


**Figure 3-26: Mode-4 Standard Deviation of the RPY Estimation Error**

**Table 3-8: Mode-4 Statistical Results of the Estimation Error**

	Sinusoidal Motion		Fixed Attitude	
	$\mu_{\hat{x}}$	$\sigma_{\hat{x}}$	$\mu_{\hat{x}}$	$\sigma_{\hat{x}}$
$\hat{X}_{err}$				
$\hat{\omega}_{IB\_X}^B \text{ err. } (^{\circ}/\text{sec})$	0.000	0.0091	0.000	0.0006
$\hat{\omega}_{IB\_Y}^B \text{ err. } (^{\circ}/\text{sec})$	0.000	0.0115	0.000	0.0007
$\hat{\omega}_{IB\_Z}^B \text{ err. } (^{\circ}/\text{sec})$	0.000	0.0117	0.000	0.0005
$\hat{q}_{1err}$	-0.0046	0.0131	-0.0219	0.0107
$\hat{q}_{2err}$	-0.0022	0.0122	-0.0037	0.0013
$\hat{q}_{3err}$	0.0040	0.0099	0.0171	0.0072
$\hat{q}_{4err}$	-0.0044	0.0017	-0.0035	0.0006
$\hat{\phi}_{err} (^{\circ})$	-0.3304	1.9001	-2.8894	1.4371
$\hat{\theta}_{err} (^{\circ})$	-0.6710	1.5964	-1.1922	0.3186
$\hat{\psi}_{err} (^{\circ})$	0.3708	1.4419	2.5908	1.0659

As a result, Mode-4 provides a successful attitude estimation performance for coarse state estimation.

Consequently, regarding to the simulations results obtained for Mod-2, Mode-3 and Mode-4, it can be stated that rate gyros are sufficient to estimate the body angular rates, but for the attitude estimation a reference sensor is necessary. Magnetometer does not provide a sufficiently accurate attitude determination due its noisy measurements. Sun sensor is a more accurate sensor then magnetometer and therefore the estimation performance obtained by using this sensor is better. However, the divergence problem for the attitude hold motion may not be prevented by using an accurate reference sensor alone. The reason of this insufficiency may be the lack of the attitude knowledge for the some type of the rotations; observability problems may occur depending on the rotation and measurement axis and this may cause the divergence problems. In the following sections, more than one reference sensor cases will be examined.

### 3.5 Accurate Full State Estimation

In this section, two EKF based estimators are presented to be used for more accurate attitude determination. The first EKF, Mode-5, fuses the rate gyros with magnetometer and Sun sensor measurements. The second one, Mode-6, uses star sensor measurements instead of sun sensor.

In the following sections, first the common system model is given; then, the measurements models related to the ADS modes are presented. Finally the application of the EKF steps is repeated.

#### *System Model:*

The system model used in EKF for Mode-5 and Mode-6 is the common system that explains in the previous Section 3.4. The dynamic and kinematics model of the satellite can be seen in the Eqs. (3.3.16, 3.3.17, 3.3.18).

#### *Measurement Model:*

The measurements model (the rate gyros, magnetometer and sun sensor models) used in EKF for the Mode-5 and Mode-6 can be seen with details in previous Section 3.4. Here the additional sensor used is the star sensor and its measurement model is given in the equations listed below.

**Star Sensor** selected for the ADS gives directly the attitude measurements, the measured quaternions as outputs. The measurements model in discrete-time can be defined as follows:

$$\tilde{y}_{ST}(k) = q_{meas}(k) = h_{ST}(x_k, v_k, k) = H_{ST}(k)x(k) + m_{ST}(k) \quad (3.3.31)$$

with  $x(k) = [\omega_{IB}^B(k) \quad q(k)]^T$  is the state vector,  $H_{ST}(k)$  is the measurement matrix for star sensor  $H_{ST}(k) = \partial h_{ST}(\hat{x}_{k+1}^-, k) / \partial \hat{x}_{k+1}^-$ . Here,  $m_{ST}(k) = N(0, R_{ST})$  is the discrete zero mean measurement noise with  $R_{ST}$  covariance matrix of the rate gyros. After linearization of the measurement equation, measurement matrix  $H_{ST}$  is obtained as follows:

$$H_{ST} = [0_{4 \times 3} \quad I_{4 \times 4}] \quad (3.3.32)$$

***Extended Kalman Filter Algorithm:***

The EKF used for ADS Mode-5 and Mode-6 has the same structure with the steps given in Section 3.3 which is based on the algorithm explained in Section 3.1.3. The main difference between these accurate ADS modes are the measurement matrix and the measurement noise covariance matrix that is related to the sensors used. Following equations gives the measurement and noise covariance matrix for each accurate ADS modes respectively.

$$R_{MOD\_5} = \begin{bmatrix} I_{3 \times 3} \cdot R_{RG} & 0_{3 \times 3} & 0_{3 \times 3} \\ 0_{3 \times 3} & I_{3 \times 3} \cdot R_{MAG} & 0_{3 \times 3} \\ 0_{3 \times 3} & 0_{3 \times 3} & I_{3 \times 3} \cdot R_{SUN} \end{bmatrix} \quad (3.3.33)$$

$$H_{MOD\_5} = \begin{bmatrix} H_{RG} \\ H_{MAG} \\ H_{SUN} \end{bmatrix} \quad (3.3.34)$$

$$R_{MOD\_6} = \begin{bmatrix} I_{3 \times 3} \cdot R_{RG} & 0_{3 \times 4} \\ 0_{4 \times 3} & I_{4 \times 4} \cdot R_{ST} \end{bmatrix} \quad (3.3.35)$$

$$H_{MOD\_6} = \begin{bmatrix} H_{RG} \\ H_{ST} \end{bmatrix} \quad (3.3.36)$$

### Simulation Results:

The Satellite ADS simulation sampling time and measurement sampling time for the each sensor is selected as 5 Hz. Results are obtained by running the simulations during 300 seconds and these results are given separately in the following sub-sections.

### Mod-5 Results

ADS Mode-5 use rate gyro, magnetometer and sun sensor measurements in the estimation of the angular rates and attitude of the satellite. As applied in previous sections, a motion profile containing the sinusoidal and fixed attitude is tested. The initial attitude angles are given as  $\phi = \theta = \psi = 20^\circ$ . The real and estimated states and estimation errors are given respectively in the following Figure 3-27, Figure 3-28 and Figure 3-29.

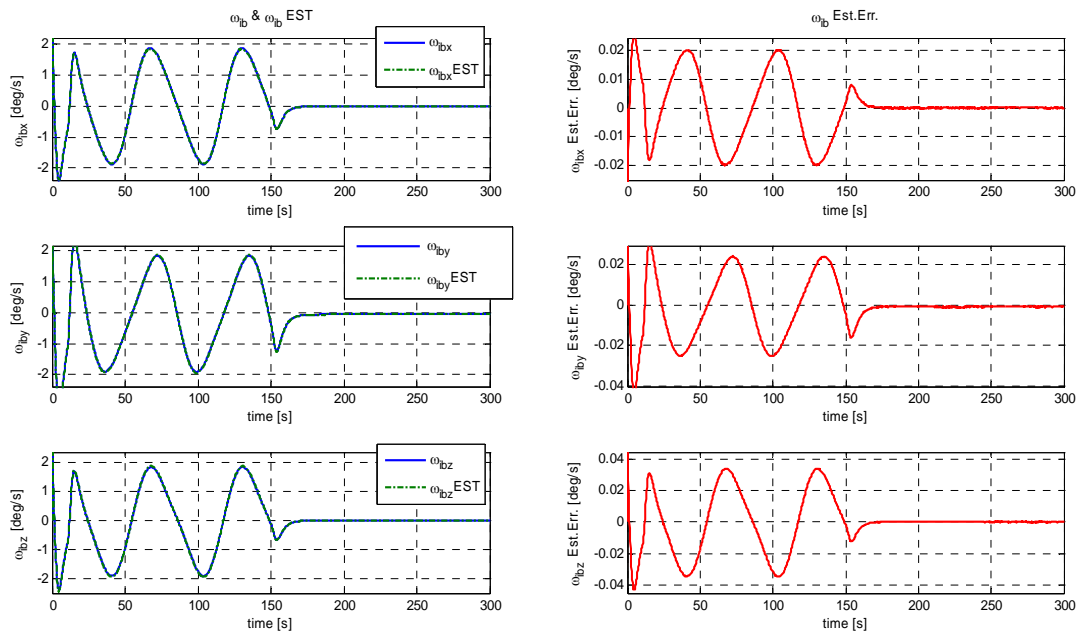
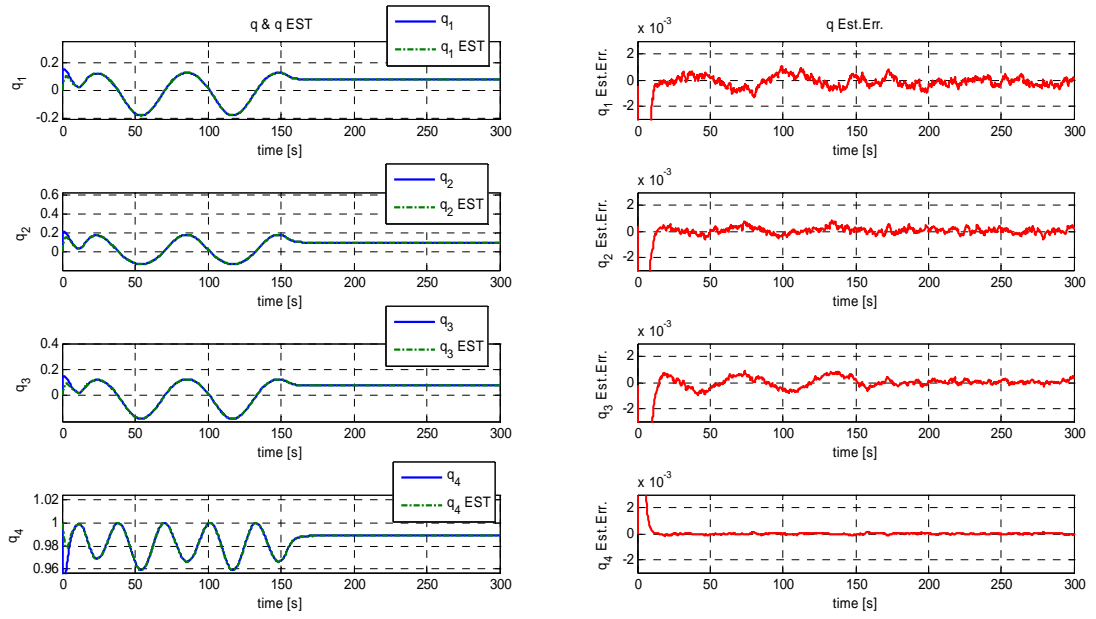
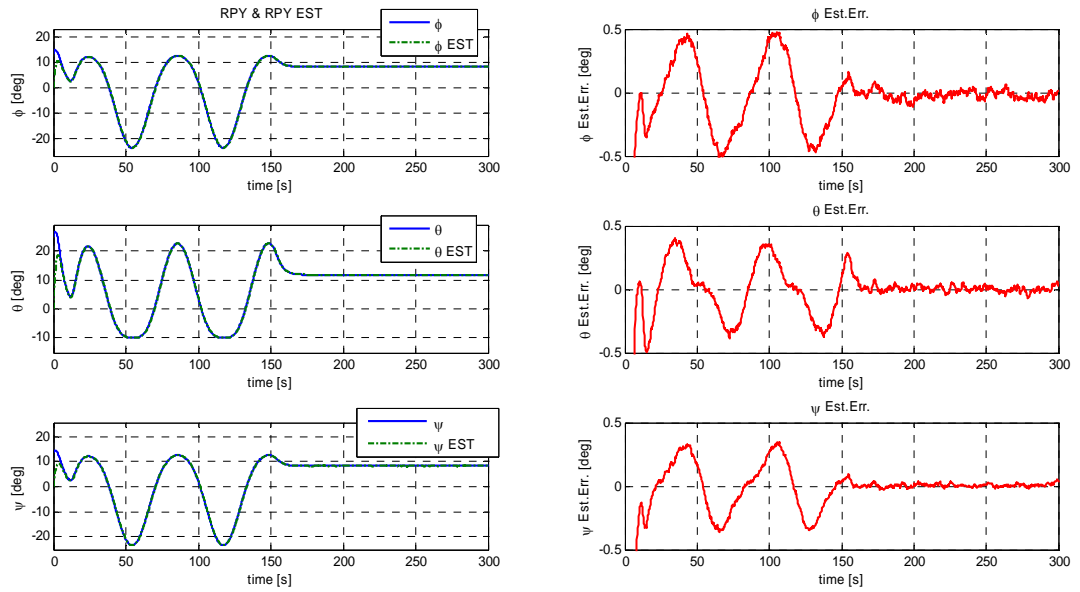


Figure 3-27: Mode-5 Real and Estimated Angular Rates



**Figure 3-28: Mode-5 Real and Estimated Quaternions**



**Figure 3-29: Mode-5 Real and Estimated RPY Angles**

In this mode a very accurate attitude determination is achieved by using two reference sensors. The accuracy and the divergence problem on the estimation, seen in Mod-3 and Mod-4, are not observed in this mode due to two reference sensors.

Statistical results are taken by running Monte Carlo simulation 20 times. The mean  $\mu_{\hat{x}}$  and the standard deviation  $\sigma_{\hat{x}}$  of the estimation errors are given in the Figure 3-30 to Figure 3-35 and Table 3-9.

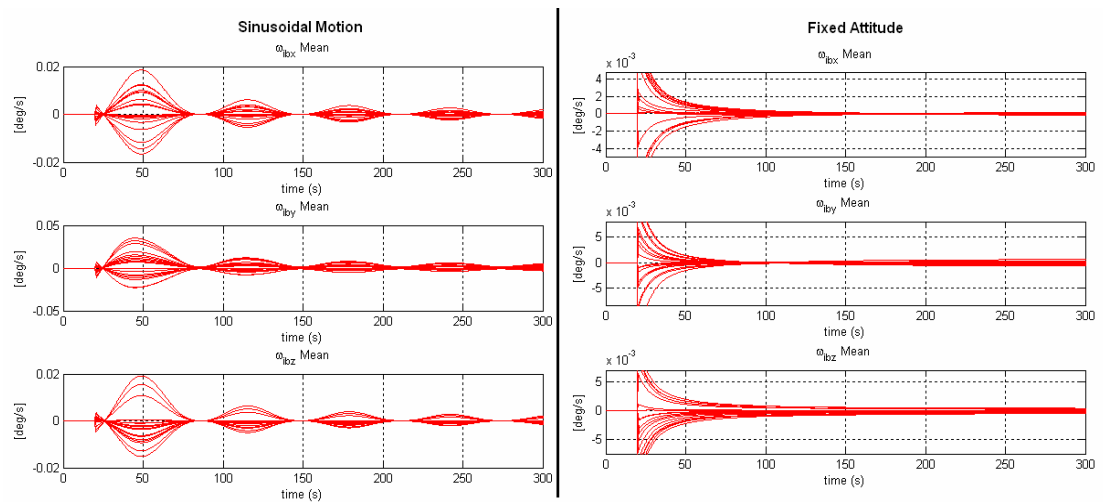


**Figure 3-30: Mode-5 Mean of the Angular Rates Estimation Error**

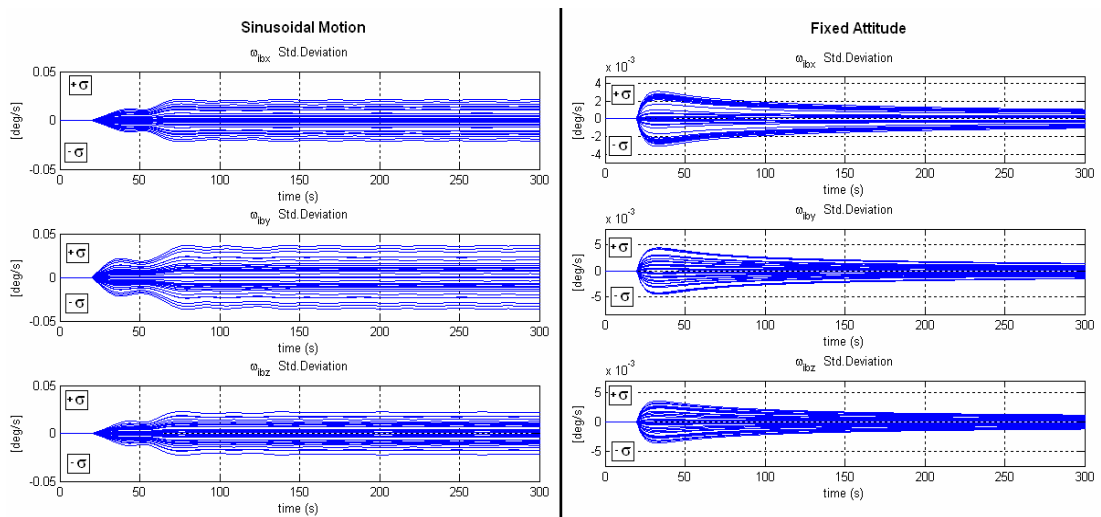


**Figure 3-31: Mode-5 Standard Deviation of the Angular Rates Estimation Error**

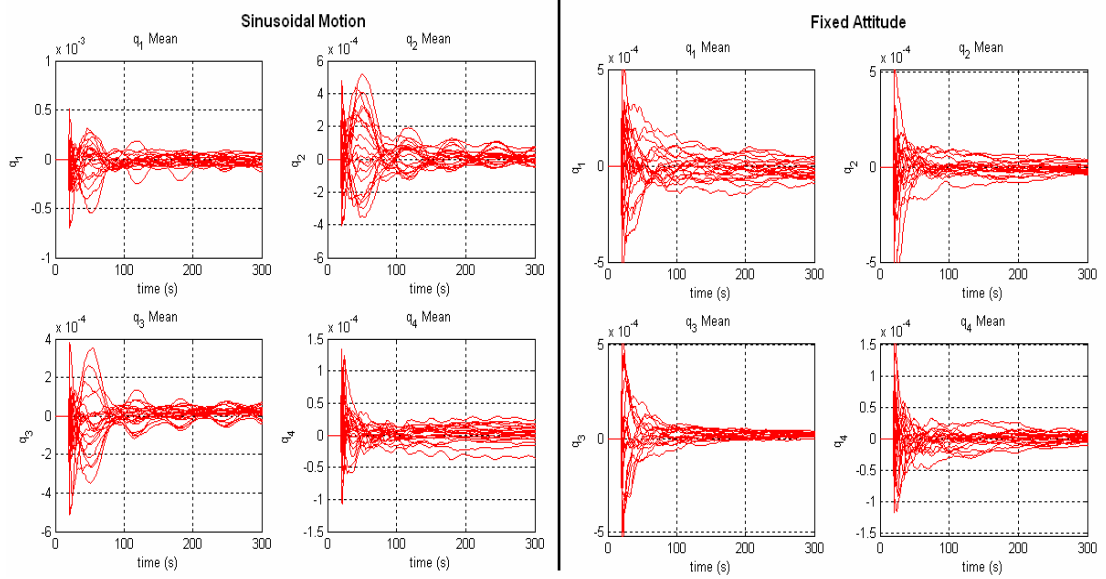


**Figure 3-32: Mode-5 Mean of the Quaternions Estimation Error**

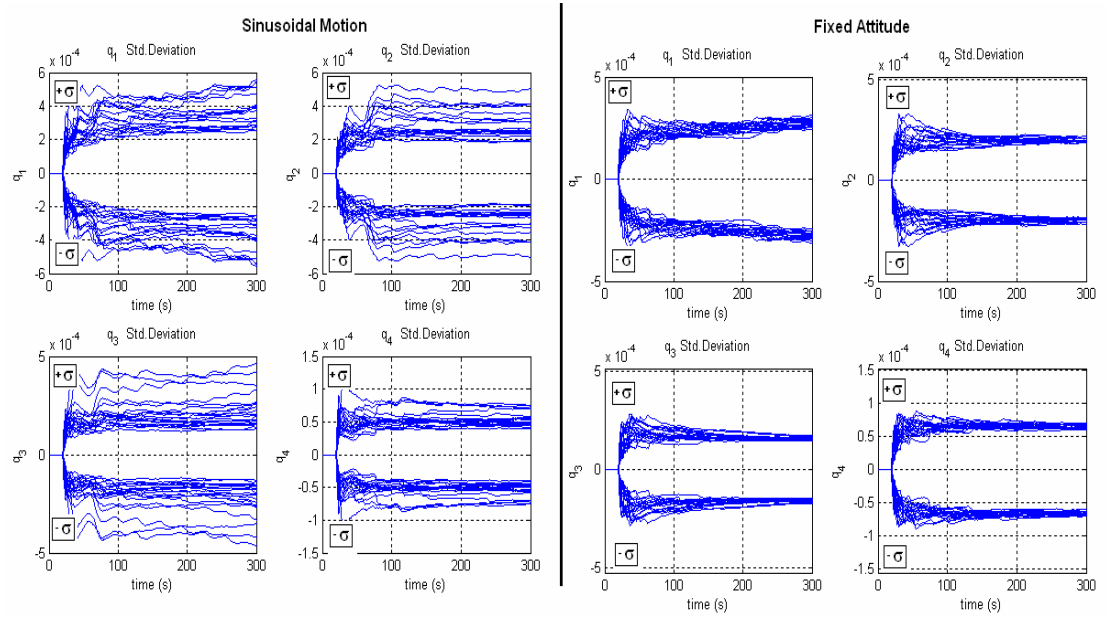


**Figure 3-33: Mode-5 Standard Deviation of the Quaternions Estimation Error**

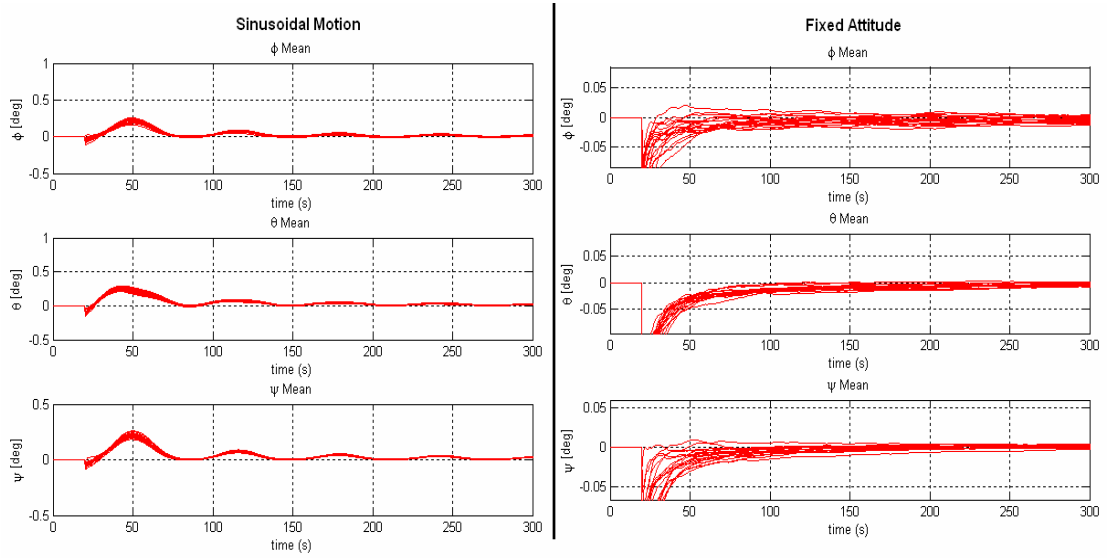


**Figure 3-34: Mode-5 Mean of the RPY Estimation Error**

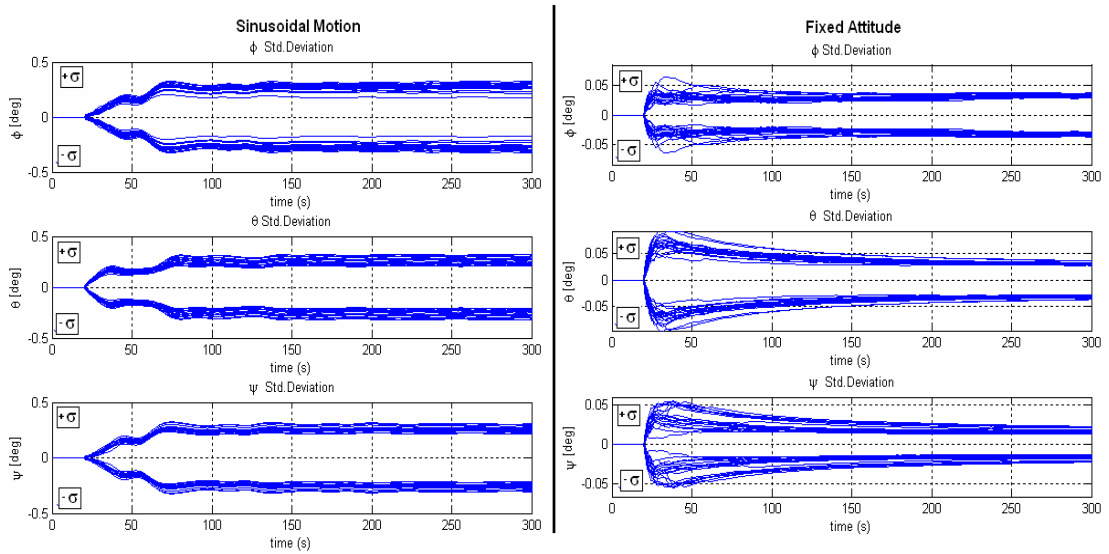


**Figure 3-35: Mode-5 Standard Deviation of the RPY Estimation Error**

**Table 3-9: Mode-5 Statistical Results of the Estimation Error**

$\hat{X}_{err}$	Sinusoidal Motion		Fixed Attitude	
	$\mu_{\hat{x}}$	$\sigma_{\hat{x}}$	$\mu_{\hat{x}}$	$\sigma_{\hat{x}}$
$\hat{\omega}_{IB\_X}^B err. (^{\circ}/sec)$	0.000	0.0103	0.000	0.0006
$\hat{\omega}_{IB\_Y}^B err. (^{\circ}/sec)$	0.000	0.0160	0.000	0.0007
$\hat{\omega}_{IB\_Z}^B err. (^{\circ}/sec)$	0.000	0.0075	0.000	0.0007
$\hat{q}_{1err}$	0.000	0.0004	0.000	0.0003
$\hat{q}_{2err}$	0.000	0.0003	0.000	0.0002
$\hat{q}_{3err}$	0.000	0.0002	0.000	0.0002
$\hat{q}_{4err}$	0.000	0.0001	0.000	0.0001
$\hat{\phi}_{err} (^{\circ})$	0.0204	0.2696	-0.0054	0.0327
$\hat{\theta}_{err} (^{\circ})$	0.0240	0.2611	-0.0045	0.0311
$\hat{\psi}_{err} (^{\circ})$	0.0257	0.2597	0.0015	0.0181

Consequently, Mod-5 results show that the accurate full state estimation is obtained by using one inertial and two reference sensors. Second reference sensor prevents the divergence in the estimation by using Mode-3 and Mode-4 that occurs in the case of the attitude hold maneuver. Mode-5 attitude estimation error is in the band interval of  $\pm 0.5^{\circ}$  for a sinusoidal motion defined in simulations. This error values decrease when the satellite does an attitude hold maneuver and this value is approximately  $\pm 0.05^{\circ}$ .

### Mod-6 Results

ADS Mode-6 use rate gyro and star sensor measurements for the accurate full state estimation. In his part same motion profile is used as before. The initial attitude angles are  $\phi = \theta = \psi = 20^{\circ}$ . The real and estimated states and estimation errors under this defined motion profile are given respectively in the following Figure 3-36, Figure 3-37 and Figure 3-38.

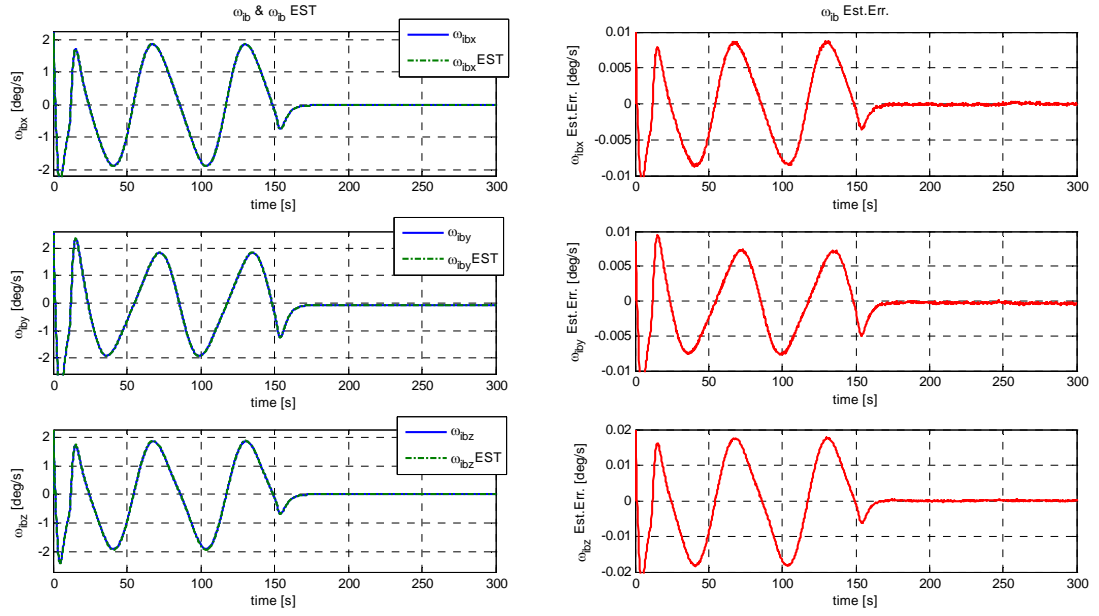


**Figure 3-36: Mode-6 Real and Estimated Angular Rates**

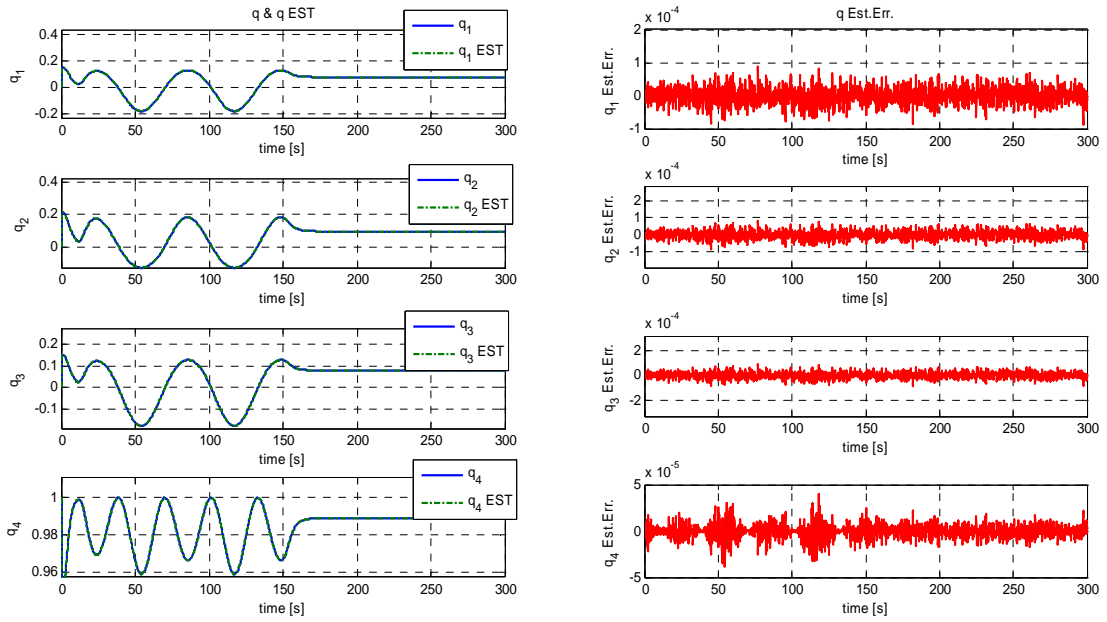


**Figure 3-37: Mode-6 Real and Estimated Quaternions**

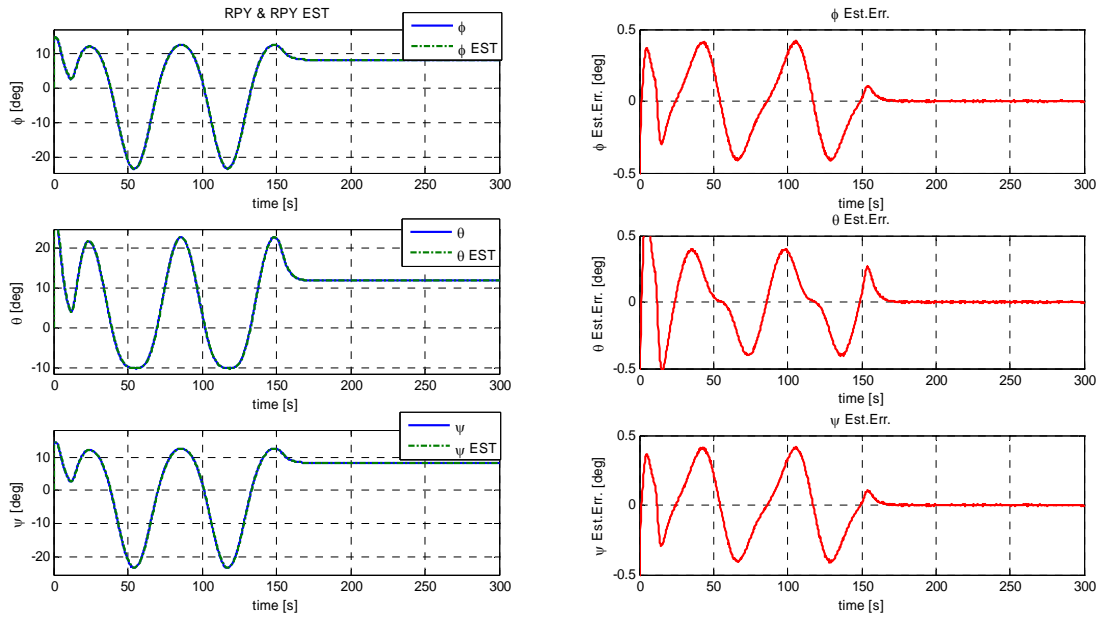


**Figure 3-38: Mode-6 Real and Estimated RPY Angles**

Consequently, the simulation results obtained for Mod-6 demonstrates extremely accurate attitude determination since one inertial sensor and one very accurate reference sensor, which both has a linear measurement models, are used together in ADS. It means that since satellite's states are measured directly by accurate sensors, good state estimation is obtained. The results of the Monte Carlo analysis are given in the figures Figure 3-39 to Figure 3-44 and in Table 3-10 for sinusoidal attitude and fixed attitude profiles.

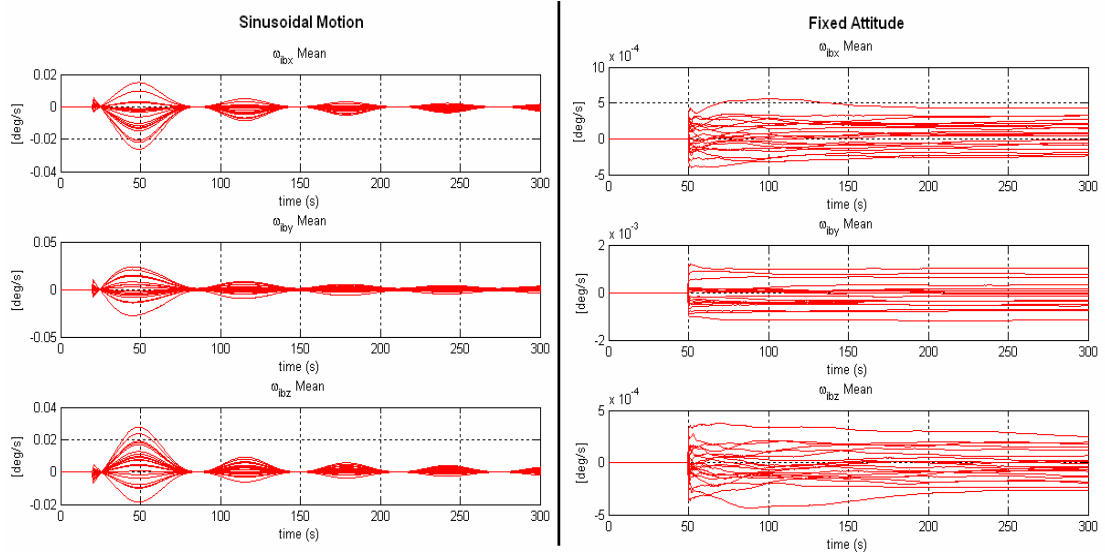


**Figure 3-39: Mode-6 Mean of the Angular Rates Estimation Error**

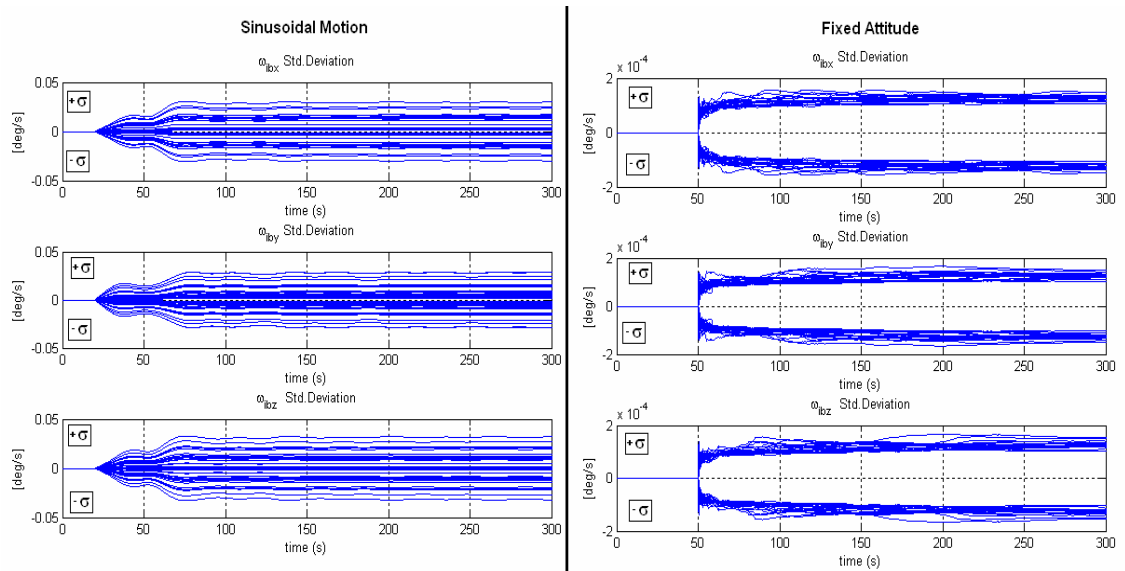


**Figure 3-40: Mode-6 Standard Deviation of the Angular Rates Estimation Error**

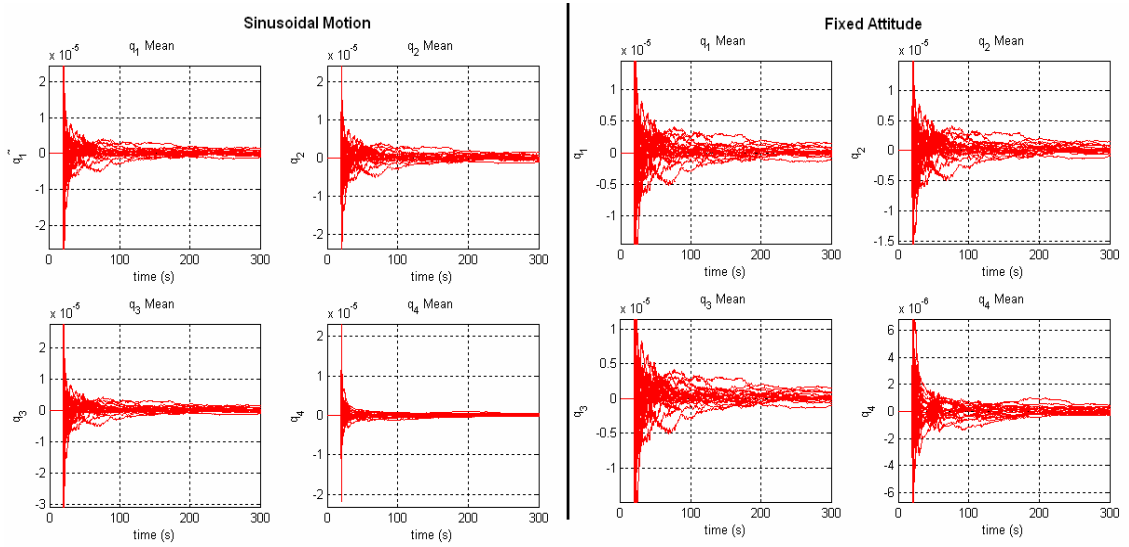


**Figure 3-41: Mode-6 Mean of the Quaternions Estimation Error**

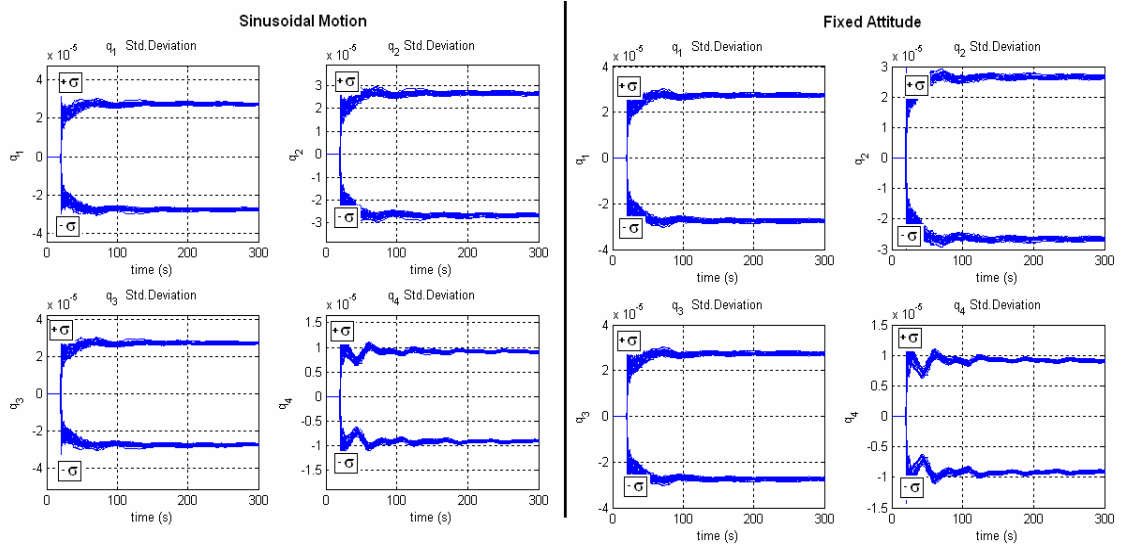


**Figure 3-42: Mode-6 Standard Deviation of the Quaternions Estimation Error**

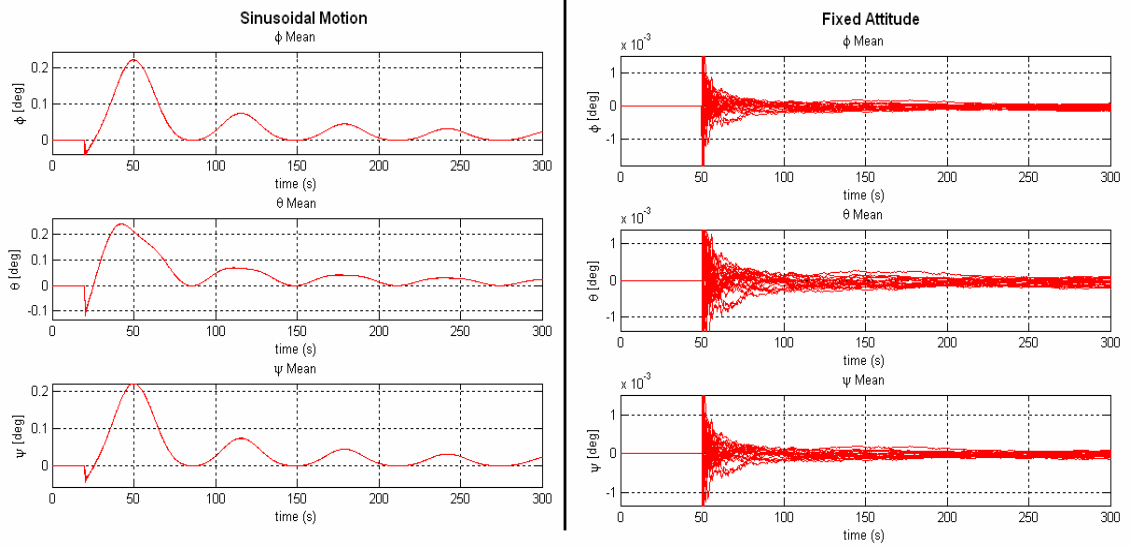


**Figure 3-43: Mode-6 Mean of the RPY Angles Estimation Error**

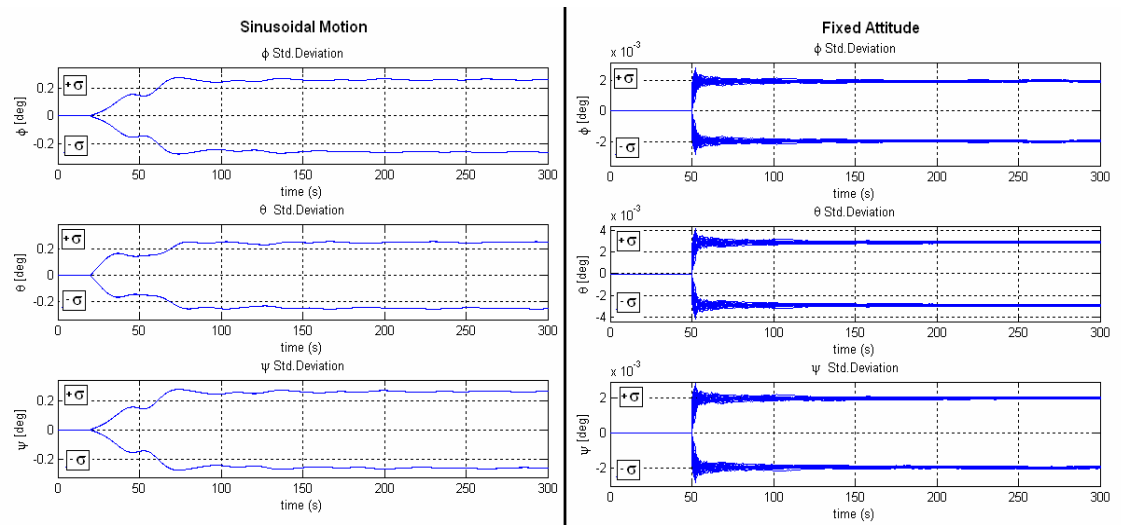


**Figure 3-44: Mode-6 Standard Deviation of the RPY Angles Estimation Error**

**Table 3-10: Mode-6 Statistical Results of the Estimation Error**

	Sinusoidal Motion		Fixed Attitude	
	$\mu_{\hat{x}}$	$\sigma_{\hat{x}}$	$\mu_{\hat{x}}$	$\sigma_{\hat{x}}$
$\hat{X}_{err}$				
$\hat{\omega}_{IB\_X}^B \text{ err. } (^{\circ}/\text{sec})$	0.000	0.0105	0.000	0.0007
$\hat{\omega}_{IB\_Y}^B \text{ err. } (^{\circ}/\text{sec})$	0.000	0.0116	0.000	0.0007
$\hat{\omega}_{IB\_Z}^B \text{ err. } (^{\circ}/\text{sec})$	0.000	0.0128	0.000	0.0006
$\hat{q}_{1err}$	0.000	3e-5	0.000	2.5e-5
$\hat{q}_{2err}$	0.000	3e-5	0.000	2.0e-5
$\hat{q}_{3err}$	0.000	3e-5	0.000	2.5e-5
$\hat{q}_{4err}$	0.000	1e-5	0.000	1e-5
$\hat{\phi}_{err} (^{\circ})$	0.0228	0.2641	-0.0016	0.0020
$\hat{\theta}_{err} (^{\circ})$	0.0226	0.2506	-0.0037	0.0029
$\hat{\psi}_{err} (^{\circ})$	0.0227	0.2628	-0.0017	0.0020

As a result, Mode-6 provides very accurate attitude estimation. Attitude estimation error is in the band interval of  $\pm 0.4^{\circ}$  for a sinusoidal motion. This error values decrease to  $\pm 0.005^{\circ}$  for an attitude hold maneuver. Monte Carlo analysis show that the standard deviation values of the attitude estimation is approximately  $\pm 0.26^{\circ}$  for sinusoidal motion profile and approximately  $\pm 0.003^{\circ}$  for attitude hold maneuver profile and the mean values of the errors shows that there is no divergence problem on the state estimation.

Regarding to the results of the Mode-5 and Mode-6, it can be concluded that highly accurate full state estimation can be achieved by using one inertial and more than one reference sensors. These reference sensors give the components of the direction vector as measurement; however the rotation of the satellite about that direction is unknown and as a result the divergence problem occurs on estimation and estimation error increases. In order to resolve this observability problem, it is necessary to use a second reference sensor; but in that case the mounting location and the direction of the source of the second sensor will become an important parameter that must be

taken into consideration. The divergence problem and bad estimation will occur again when the measured direction vectors of these two sensors become parallel to each other. On the other hand, as seen at Mode-6, it is possible to obtain a perfect full state estimation by using one accurate inertial and one accurate attitude sensor if the measurement model is linear ( $H_{yy} = I$ ), these sensors measure directly the full state. Here, it is suitable to remember the working principal of the star sensor. As mentioned in the section 2.4.4, star sensor measures star coordinates by comparing its measurements with known star directions from its star catalog.

### 3.6 A Multimode Attitude Determination System

This section presents *ADS mode selection* module and gives the performance of the ADS during the orbit navigations. Here the motivation is to generate an ADS which uses various sensors according to their availability. For this reason *sensor flag logic* is created for each sensor that is based on the availability of the sensor. This flag logic gives *one* as output when sensor is available at its measurement frequency and it gives *zeros* for other cases.

A sub-module named ADS mode selection is prepared that selects suitable Kalman Filter algorithm depending on the sensors activity and it sends the ADS Mode knowledge as output to the Kalman Filter Module. Here, sun sensor and star sensor availability are related to the satellite orbital position. For instance, sun sensor flag is zero when the satellite is in the Earth eclipse and on the contrary star sensor flag is zero for the cases that sensor is exposed to the sun light.

This autonomous ADS simulation is run for 1 orbital time period (approximately 100 minutes) at 5 Hz (sampling time  $\equiv dt$ ). Different measurements rates are appointed to each sensor: measurement sampling rate for the rate gyros is 0.2 sec. ( $dt \times 1$ ), for magnetometer it is 1 sec ( $dt \times 5$ ), for sun sensor it is 0.4 sec ( $dt \times 2$ ), and finally for star sensor it is 0.6 sec ( $dt \times 3$ ). The graphics that show the sensor flag values and the selected ADS mode values is given at the following Figure 3-45.

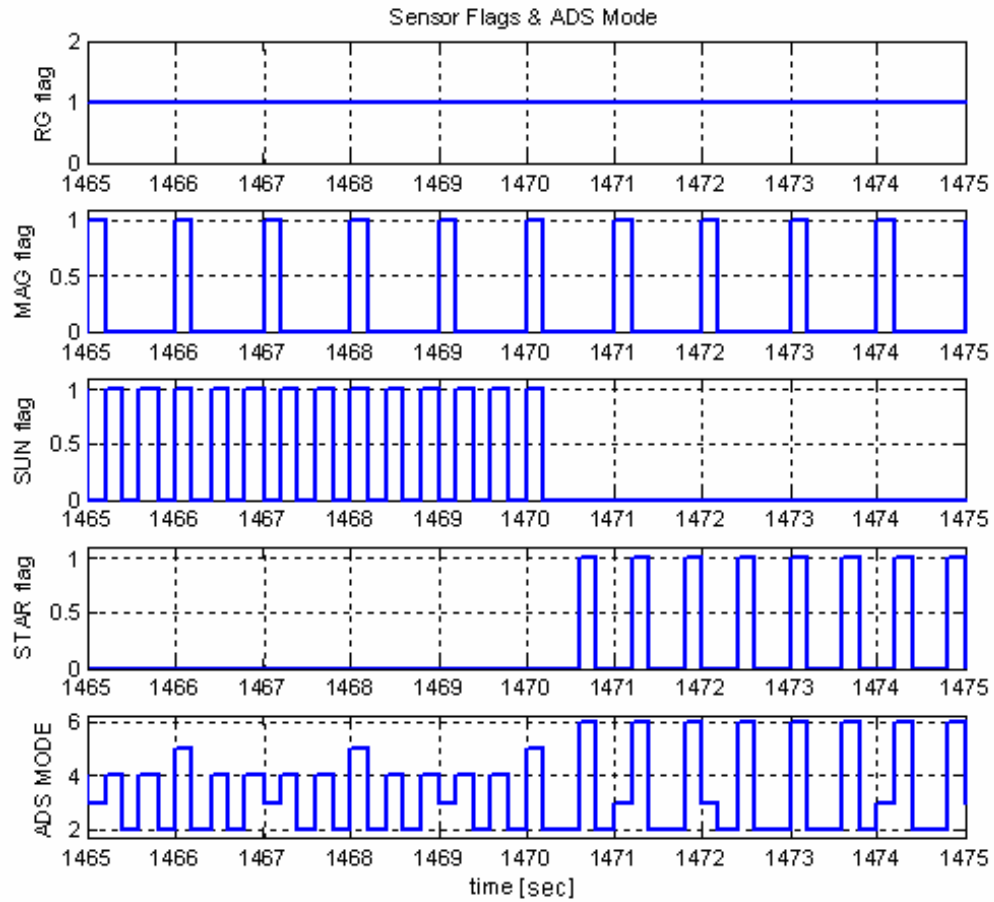


**Figure 3-45: Sensor Flags and Selected ADS Mode**

Regarding to the selected ADS mode number, related Kalman Filter algorithms is run; then the estimated state  $\hat{x}$  values and the system covariance matrix  $P$  are conserved between the mode transition, and they are used as initial inputs to the next ADS mode. The working principal of this module is simulated on the following figures. The Figure 3-46 shows the selection of the ADS mode and related KF algorithms when rate gyro and magnetometer give measurements. The second Figure 3-47 shows the situation and mode transition phases when Sun sensor becomes active and give a measurement. From these figures, it can be seen that the outputs  $\hat{x}$  and  $P$  are used as initial inputs to the next selected ADS mode.

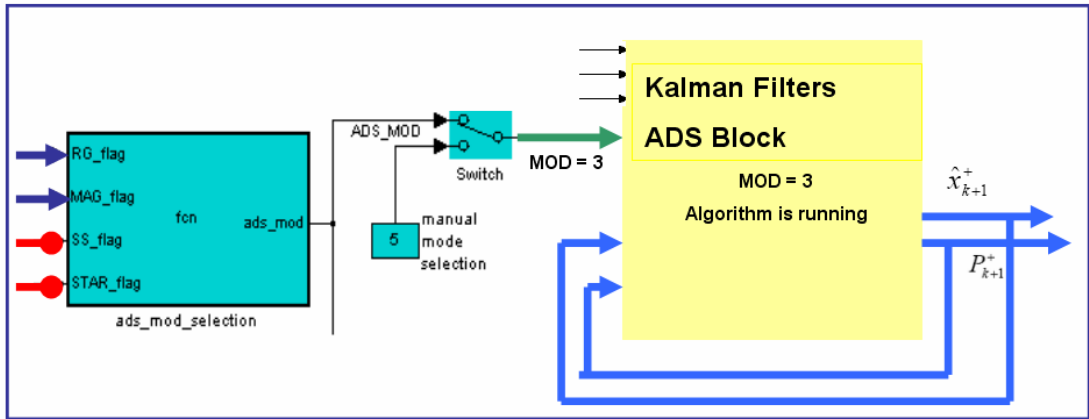


Figure 3-46: Mode Selection Scenario-1

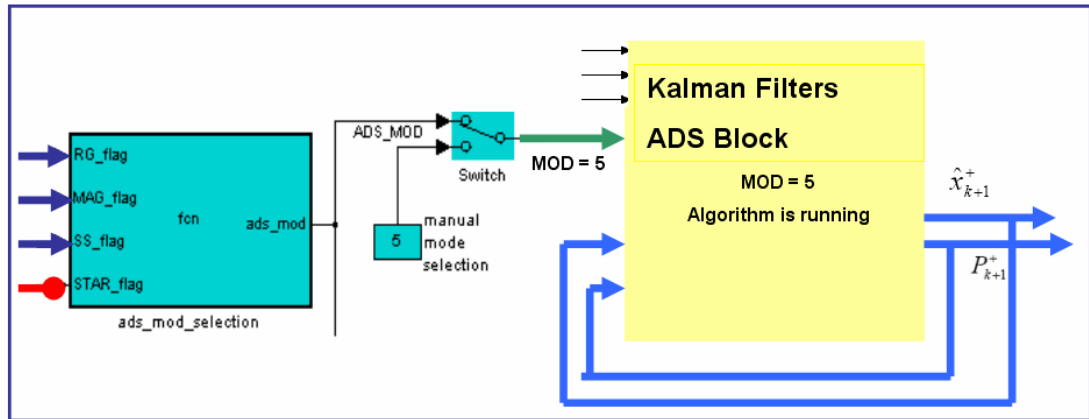
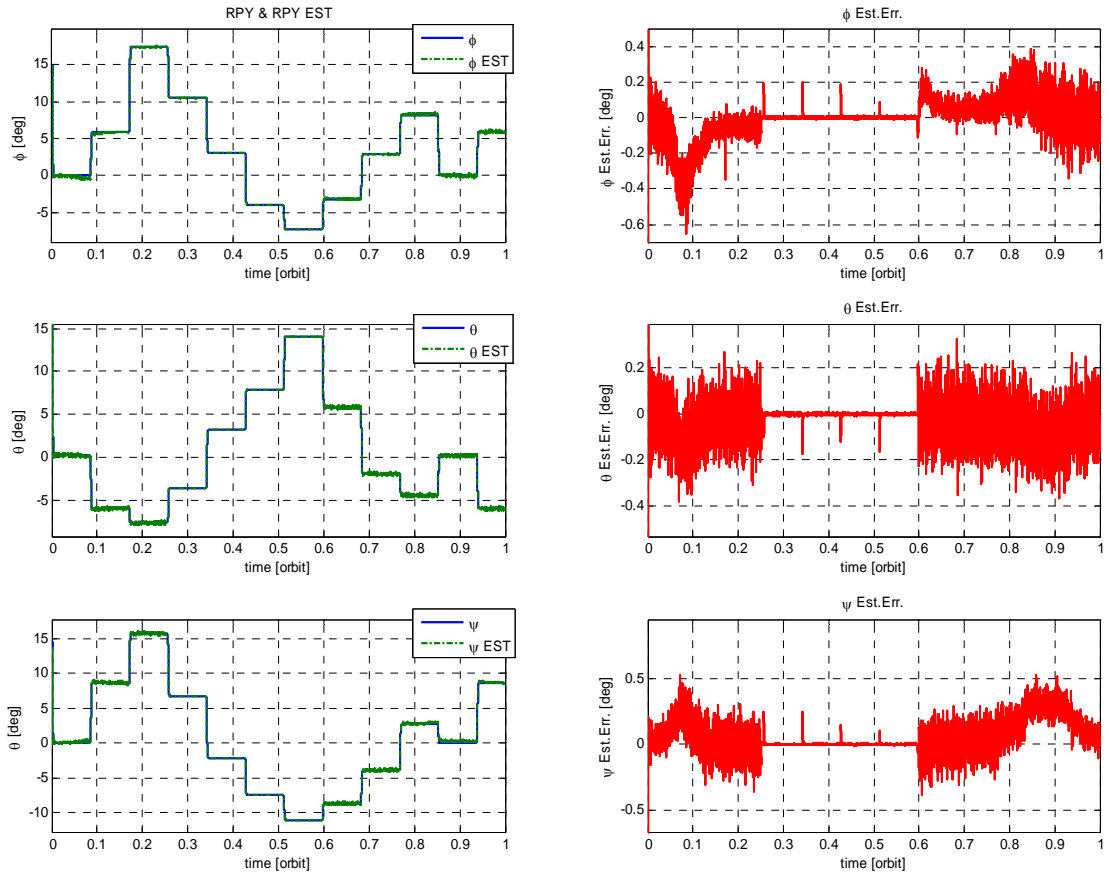


Figure 3-47: Mode Selection Scenario-2

In order to determine the performance of the autonomous ADS during one orbital period time, a motion profile scenario that contains several attitude maneuvers is formed. In the Figure 3-48 the simulation results of the attitude estimation are given for this motion profile.



**Figure 3-48: Attitude Estimation Performance For Several Successive Maneuvers**

Regarding to the results, it can be concluded that the successful attitude determination is obtained by the multimode ADS. For this kind of motion profile that contains successive attitude maneuvers, the attitude estimation error is approximately  $\pm 0.2^\circ$  when star sensor is not used. When the star sensor is available, the estimation error decreases to approximately  $\pm 0.01^\circ$ . Actually, these numbers do not show the estimation performance clearly. Note that Monte Carlo simulation results given in the previous sections are the true performance of each mode. However by using a multimode AS, the initial convergence problem is alleviated.

### **3.7 Conclusion**

In this third section, *Kalman Filter Based Attitude Determination System* is presented and it is shown that to increase the attitude determination accuracy different reference sensors shall be used. A multimode attitude determination is also demonstrated successfully.

## CHAPTER 4

### ATTITUDE DETERMINATION FOR THE SATELLITE ATTITUDE CONTROL TEST SETUP

This chapter presents the Kalman filter based attitude determination system prepared for the satellite control test setup. Here, the main objective is to generate a cost-effective, relatively accurate and stable attitude determination system by using only an Inertial Measurement Unit (IMU) including 3 axis rate gyros and 3 axis accelerometer. For this purpose two different Kalman filters are prepared; the first one is based on extended Kalman filter and the second one is based on unscented Kalman filter algorithms.

In the following sections the information about the satellite test setups, the details about the rotational motion model test setup, the sensor measurement models used, the attitude determination system structure and the results and of the estimation algorithms are given and discussed respectively.

In this thesis, a test setup model is created named Satellite Attitude Determination and Control Test Setup (SACoTS) and the following sections contain its rotational motion model, its sensor measurement models and the attitude determination algorithms prepared specially for SACoTS depending on the sensors used.

#### **4.1 SACoTS Simulation Model**

In this section, rotational motion model of a ground based satellite test setup is derived. Basically the dynamics and kinematics equations are similar to the satellite's motion equations that given in Section 3.1. However there are some differences because of the gravity and the environment effects. The main difference is the torque

acting on the system due to the eccentricity between the center of gravity (CG) and center of rotation (CR). The air bearing table has a 3 axis rotational freedom on a one point called CR and in reality the CG never coincides with the CR due to the mass distribution which is not uniform on the air bearing table. The second difference is to the environmental characteristics. The disturbance torques level caused by the space environment has some differences with the disturbance level existing on the ground, in a laboratory environment. These two differences are taken in to consideration on the SACoTS simulation model. The axis frames used in the SACoTS are given in the following Figure 4-1.

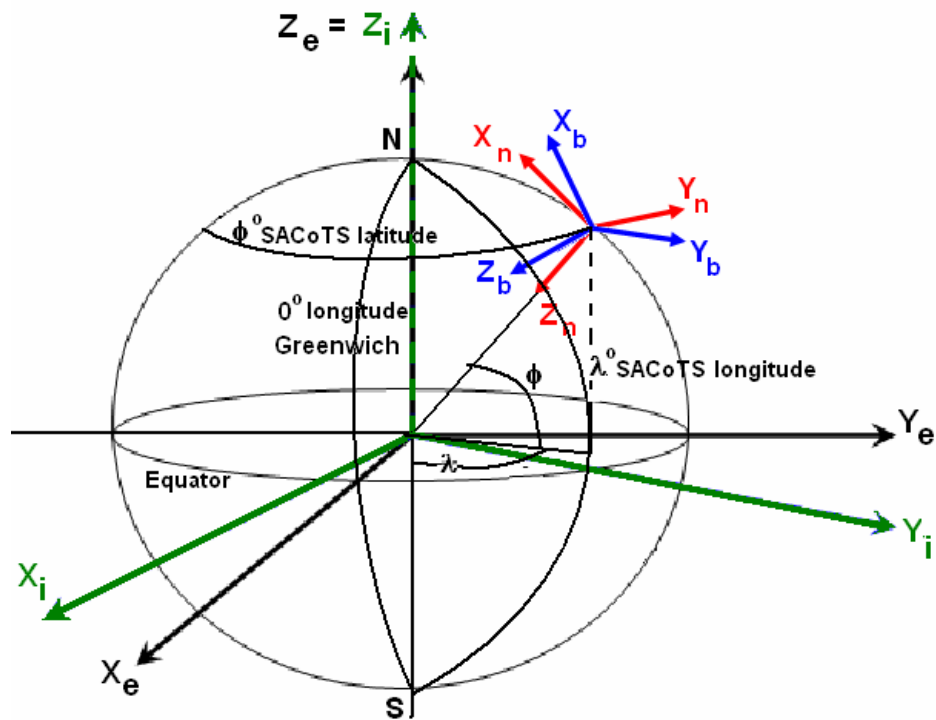


**Figure 4-1: Axis Frames used for SACoTS**

Here,  $X_i, Y_i, Z_i$  is the Earth-Centered Inertial (ECI) Reference Frame,  $X_e, Y_e, Z_e$  is the Earth-Centered Earth fixed (ECEF) Reference Frame,  $X_b, Y_b, Z_b$  is the SACoTS Body Axis Reference Frame that is fixed on the SACoTS and  $X_n, Y_n, Z_n$  is the Navigation Reference Frame fixed on the SACoTS that coincide with the center of the Body Reference Frame. This navigation frame can also be considered as the

orbital referenced frame that used on the satellite system but there is only one difference between them; in SACoTS condition, this navigation frame is fixed on the Earth, on the laboratory.

The dynamics model of the SACoTS is derived by using the Euler's equations of motion and the kinematics model is expressed by using the quaternions representation. The dynamic equations of this system can be reformulated as follows:

$$\dot{\omega}_{IB}^B = I^{-1} \left( -\tilde{\omega}_{IB}^B I \omega_{IB}^B + \tau_{INT}^B + \tau_{EXT}^B \right) \quad (4.1.1)$$

where  $\tilde{\omega}_{IB}^B$  is the dyadic form of the angular rates,  $I$  is the inertial matrix,  $\tau_{INT}^B$  and  $\tau_{EXT}^B$  are the internal and external torques acting to the system.  $\tau_{INT}^B$  occurs due to eccentricity between the CG and CR of the air bearing table. The aerodynamics and other unknown torques can be classified as external torque sources.  $\tau_{INT}^B$  can be defined as follows:

$$\vec{\tau}_{INT}^B = \vec{\tau}_{ecc} = \vec{r}_{ecc} \times M \vec{g} \quad (4.1.2)$$

where  $\vec{r}_{ecc}$  is the distance vector between the CG and CR,  $M$  is the total mass and  $\vec{g}$  is the gravity vector.

SACoTS kinematics model defined by quaternions representation is given as follows. In this kinematics model the angular rates of the body are expressed with respect to the navigation axis frame because the attitude of the air bearing table will be defined in this navigation frame. The turn rate of the Earth and the coordinates of the SACoTS in terms of longitude and latitude are used in the attitude expressions as follows:

$$\dot{q} = \frac{1}{2} \Omega_{NB}^B q \quad (4.13)$$

$$\omega_{NB}^B = \omega_{IB}^B - C_N^B \omega_{IE}^N \quad (4.14)$$

where  $C_N^B$  is the direction cosine matrix from navigation frame to body frame and  $\omega_{IE}^N$  is the Earth turn rate expressed in navigation frame. This expression can be written by using the latitude value of the SACoTS as follows:

$$\omega_{IE}^N = [\omega_E \cos \Phi \quad 0 \quad -\omega_E \sin \Phi]^T \quad (4.1.5)$$

where  $\omega_E$  is the Earth turn rate and  $\Phi$  is the latitude of the SACoTS.

The dynamic and kinematics models of the SACoTS are formed in Matlab Simulink by using the equations given below and the block diagram of these models can be seen in the Figure 4-2. The physical properties of the SACoTS are given in the following Table 4-1.

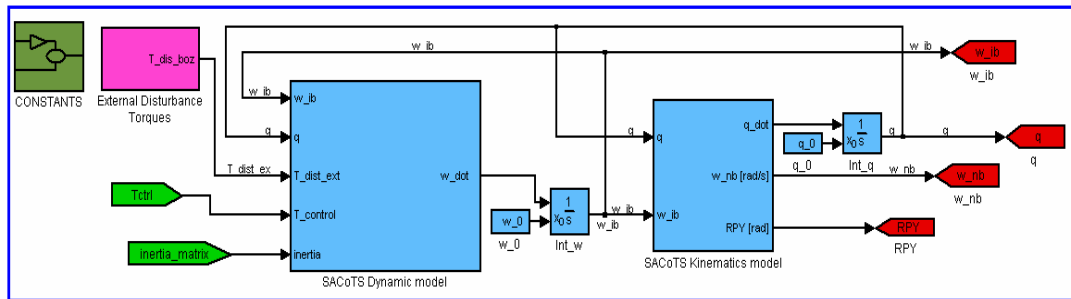


**Figure 4-2: SACoTS Rotational Motion Model**

**Table 4-1: SACoTS Parameters**

Mass (m):	150 kg
Inertia Matrix (I):	$I = \begin{bmatrix} 12 & 0.8 & 0.95 \\ 0.8 & 15 & 1.05 \\ 0.95 & 1.05 & 20 \end{bmatrix} \text{ kg.m}^2$
CoG/CoR eccentricity (r_ecc):	$r\_ecc = \begin{bmatrix} 10^{-8} \\ 10^{-8} \\ 10^{-8} \end{bmatrix} \text{ m}$

## 4.2 SACoTS Sensor Measurements Models

In this section, explanations about the mathematical model of the sensors used on SACoTS are given. The main sensor of this test setup is an *Inertial Measurement Unit (IMU)* that contains 3 axis rate gyros and 3 axis accelerometers. In SACoTS simulations, the same rate gyroscopes measurement model given in the Section 2.4.1 is used. Therefore, this section represents only the 3 axis accelerometer measurement model. The specifications of the sensor used on this system are given at the end of this section.

A vehicle that moves on the Earth is exposed also to the gravitational force. For this reason the total force acting on a vehicle can be expressed as follows:

$$\vec{F} = m\vec{a} = m\vec{g} + m\vec{f} \quad (4.2.1)$$

where,  $\vec{g}$  is the gravitational acceleration and  $\vec{f}$  is the acceleration produced by forces other than gravitational field. An accelerometer is insensitive to the gravitational acceleration and therefore, it gives an output proportional to the non-gravitational force per unit mass  $\vec{f}$  to which the sensor is exposed along its sensitive axis. This force is called as *specific force* exerted on the sensor. For instance, taking the case of an accelerometer that is falling freely within gravitational field. In this situation the output of the sensor will be zeros because the specific force is equal to zero,  $\vec{a} = \vec{g}$ . Conversely, in the case where the sensor is held stationary, the specific force is not zero and the sensor will give only the gravitational force  $\vec{f} = -\vec{g}$  as output. It is clear therefore, that knowledge of gravitational field is essential to enable the measurement provided by the accelerometer to be related to the inertial acceleration. Furthermore, the output of the sensor is related also to the attitude of the vehicle for the 3 axis measurements because the accelerometers sense  $\vec{g}$  depending on their measurement axis.

In addition to this, the accelerometer will also measure the Coriolis force and centrifugal force when the vehicle has an angular rate and angular acceleration if the

sensor is not mounted on the mass center of the vehicle. The measurement errors occurred by these kinds of forces are called as *methodical errors* and the other errors caused by the sensor such as noises, biases, are called as *instrumental errors*. These errors are listed in the following Table 4-2 as follows:

**Table 4-2: Accelerometer Error Parameters**

a. Methodical Errors
a.1. Angular Rate Effect
a.2. Angular Acceleration Effect
b. Instrumental Errors
b.1. Turn on Bias
b.2. i. Bias Stability
ii. Bias Stability Correlation Time
b.3. i. Random Walk
ii. Random Walk Band Width
b.4. Scale Factor Error
b.5. Alignment Error

The three axis accelerometer measurement equation that gives perfect measurements (without noise) is formulated by considering the methodical error as follows:

$$\vec{z}_{ACC}(t) = \ddot{\vec{r}} + 2\vec{\omega} \times \dot{\vec{r}} + \dot{\vec{\omega}}(t) \times \vec{r}_{ACC} + \vec{\omega}(t)(\vec{\omega}(t) \times \vec{r}_{ACC}) - \vec{g}(C_N^B)^T \vec{k} \quad (4.2.2)$$

where,  $\vec{\omega}(t)$  is the inertial referenced body angular rates,  $\vec{r}_{ACC}$  is the coordinate vector that define the mounting location of the accelerometer with respect to center of mass of the vehicle and it is assumed to be fixed, thus  $\ddot{\vec{r}} + 2\vec{\omega} \times \dot{\vec{r}} = 0$ ,  $C_B^N$  is the direction cosine matrix from body frame to navigation frame and  $\vec{k}$  is the unit vector at the gravitational force direction. The measurement equation in matrix form can be reformulated by adding the instrumental noises as follows:

$$\begin{aligned} z_{ACC}(t) &= \dot{\vec{\omega}} r_{ACC} + \vec{\omega} (\vec{\omega} r_{ACC}) - g(C_N^B)^T [0 \ 0 \ 1]^T + w_{ACC} \\ &= h_{ACC}(x) + w_{ACC} \end{aligned} \quad (4.2.3)$$

Accelerometer instrumental error parameters listed in the Table 4-2 have the same characteristics with error model that given for rate gyroscopes in Section 3.4.1. However, there is only one difference about the conversion from random walk to white noise parameter. The converter that provides the transformation from random walk error to white noise error with  $1\sigma$  standard variation is given by the following equation:

$$RW \equiv y ;$$

$$White\_Noise \equiv z (1\sigma)$$

$$z = y \left( \frac{m/sec}{\sqrt{hr}} \right) = y \left( \frac{m/sec}{\sqrt{3600 sec}} \right) = \frac{y}{60} \frac{m}{sec} \left( \frac{1}{\sqrt{sec}} \right) \quad (4.2.4)$$

$$= \frac{y}{60} \frac{m}{sec^2} \left( \frac{sec}{\sqrt{sec}} \right) = \frac{y}{60} \frac{m}{sec^2} \sqrt{sec} = \frac{y}{60} \frac{1}{\sqrt{Hz}} \left( \frac{m}{sec^2} \right)$$

where, the unit given as  $Hz$  is the bandwidth of the random walk error.

The block diagram of the accelerometer measurement model including all the error types defined above is given in the following Figure 4-3.

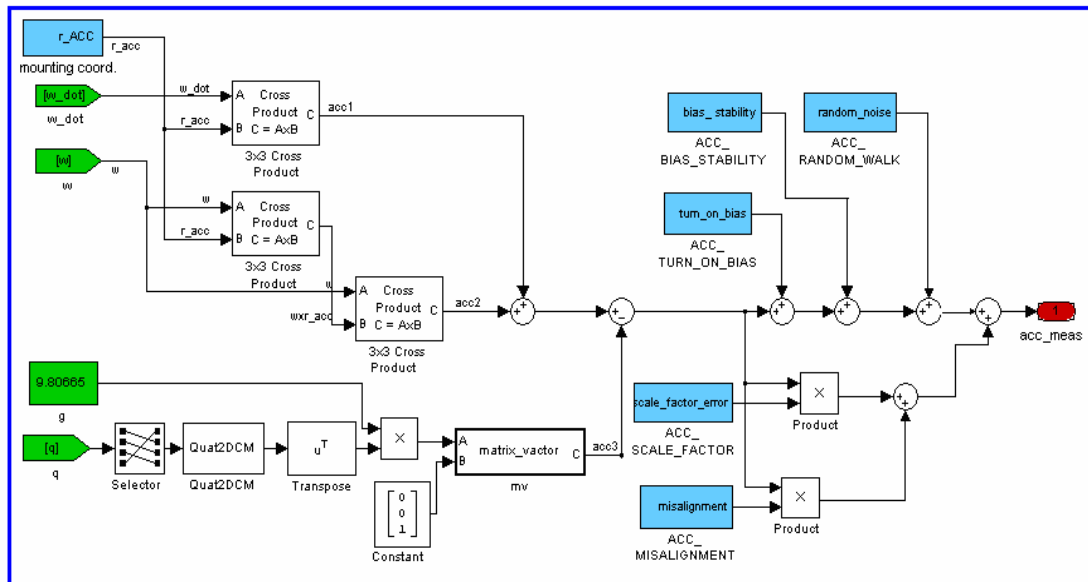


Figure 4-3: Block Diagram of the Accelerometer Measurement Model

IMU selected for the attitude determination system of the SACoTS is the product of the Crossbow Inc. called VG700AB which is a combination of the 3 axis fiber optic gyros and 3 axis MEMS (Micro Electromechanical Sensor) accelerometers. The specification sheet of this product is given in the Appendix C. The values of the error determined depending on the specification document of the product are listed in the following Table 4-3.

**Table 4-3: The Specifications of the IMU**

<b>PARAMETERS</b>	<b>RATE GYROS</b>	<b>ACCELEROMETERS</b>
Turn on Bias	$20^\circ / hr (3\sigma)$	$12 mg (3\sigma)$
Bias Stability	$20^\circ / hr (3\sigma)$	$12 mg (3\sigma)$
Bias Stability Correlation Time	20 s	20 s
Random Walk	$0.4^\circ / \sqrt{hr}$	$1 (m/s) / \sqrt{hr}$
Random Walk Band Width	100 Hz	100 Hz
Scale Factor Error	%2	%1
Alignment Error	1mrad	1mrad
Resolution	$0.025^\circ / s$	$0.6 mg$
Range	$\pm 200^\circ / s$	$\pm 4 g$

### 4.3 SACoTS Attitude Determination System and Algorithms

This sub-chapter presents Kalman filter based Attitude Determination System (ADS) of the Satellite Attitude Control Test Setup. The objective of this system is to obtain attitude knowledge of the test setup by processing the IMU measurements. The block diagram of the ADS constituted for a SACoTS is given in the Figure 4-4.

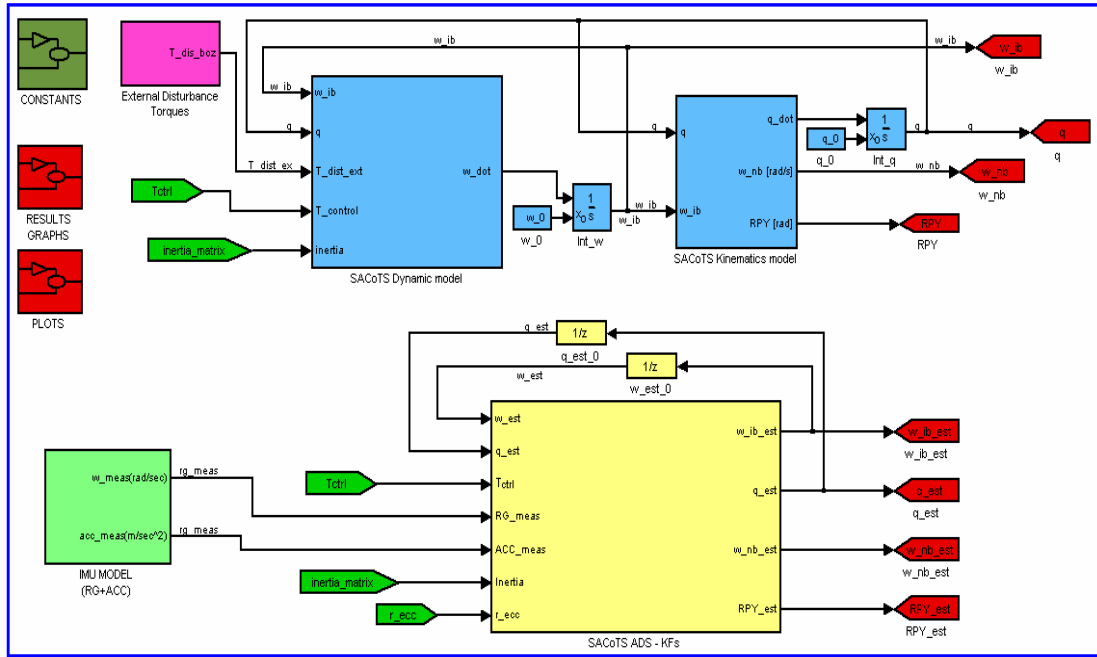


**Figure 4-4: SACoTS Attitude Determination System Block Diagram**

Two separate Kalman filters are implemented: Extended Kalman filter (EKF) algorithm and Unscented Kalman Filter (UKF) algorithm.

The following sections contain the detailed explanations about UKF algorithms, the results of the EKF, UKF and their comparison (The EKF's explanations can be seen in the Section 3.1.3).

### 4.3.1 Unscented Kalman Filter

This section contains the explanations about UKF. The structure of this unscented filter is based to estimate a fixed number of parameters which have Gaussian distribution characteristics than to estimate an arbitrary nonlinear function [4][5].

The UKF is presented for discrete-time nonlinear systems and measurement models. The equations that define the system state vector and measurements are given as follows:

$$x(k/k+1) = f(x(k/k), u(k+1), k+1) + w(k) \quad (4.3.1a)$$

$$y(k+1) = h(x(k+1), u(k+1), k+1) + v(k) \quad (4.3.1b)$$

where  $f(x(k/k), u(k+1), k+1)$  is the process model,  $x(k)$  is the state vector of the system at time step  $k$ ,  $u(k+1)$  is the input vector and  $w(k)$  is the process noise. In the measurement equation  $y(k+1)$  is the observation vector,  $h(x(k+1), u(k+1), k+1)$  is the observation model,  $v(k)$  is the measurement noise.

The noises  $w(k)$  and  $v(k)$  added to the system and measurement model respectively are assumed as Gaussian uncorrelated white noises. The expression of their covariances can be formulated as follows:

$$E[w(i) w^T(j)] = \delta_{ij} Q(i) \quad (4.3.2a)$$

$$E[v(i) v^T(j)] = \delta_{ij} R(i) \quad (4.3.2b)$$

$$E[w(i) v^T(j)] = 0 \quad (4.3.2c)$$

The Kalman filter update equations for the estimated state vector  $x(k+1/k+1)$  and for the covariance matrix  $P(k+1/k+1)$  are given by the following expressions:

$$\hat{x}(k+1/k+1) = \hat{x}(k+1/k) + K(k) \nu(k) \quad (4.3.3)$$

$$P(k+1/k+1) = P(k+1/k) - K(k+1) P_{\nu\nu}(k+1/k) K^T(k+1) \quad (4.3.4)$$

where  $\nu(k)$  is the innovation process given by;

$$\nu(k+1) = y(k+1) - \hat{y}(k+1) = y(k+1) - h(\hat{x}(k/k+1), u(k+1), k+1) \quad (4.3.5)$$

The covariance matrix expression of the innovation process  $\nu(k)$  is given by;

$$P_{\nu\nu}(k+1/k) = P_{zz}(k+1/k) + R(k+1) \quad (4.3.6)$$

where  $P_{zz}(k+1/k)$  is the covariance matrix of the measurements and  $R(k+1)$  is the covariance matrix of the measurement errors.

The equation that gives the Kalman filter gain is formulated as follows:

$$K(k+1) = P_{xz}(k+1/k)P_{\nu\nu}^{-1}(k+1/k) \quad (4.3.7)$$

where  $P_{xz}(k+1/k)$  is the cross-correlation matrix between the state vector and measurement vector.

The prediction of the system covariance matrix is given by;

$$P(k+1/k) = \Phi(k)P(k/k)\Phi^T(k) + Q(k) \quad (4.3.8)$$

where  $\Phi(k)$  is the Jacobian matrix of the system equation

The basic steps of the developed UKF are listed in the following part. The estimated state vector  $\hat{x}(k/k)$  and system covariance matrix  $P(k/k)$  are computed at time step  $k$  by using the equations given above. The objective of the UKF algorithm is to obtain the propagated values of  $\hat{x}(k+1/k)$ ,  $P(k+1/k)$  and calculate the Kalman gain  $K(k+1)$ . The UKF algorithm's steps are listed below:

1. Computation of the translated sigma  $\sigma$  points by using  $P(k/k)$  matrix

$$\sigma(k/k) \leftarrow 2n \text{ columns from } \pm\sqrt{(n+\kappa)P(k/k)} \quad (4.3.9)$$

$$X_0(k/k) = \hat{x}(k/k) \quad (4.3.10)$$

$$X_i(k/k) = \sigma_i(k/k) + \hat{x}(k/k) \quad (4.3.11)$$

## 2. Computation of the weights

$$W_0 = \frac{\kappa}{n + \kappa} \quad (4.3.12a)$$

$$W_i = \frac{1}{2(n + \kappa)} \quad (4.3.12b)$$

## 3. Computation of the predicted mean

$$X_i(k+1/k) = f(X_i(k/k), u(k), k) \text{ for } 0 \leq i \leq 2n \quad (4.3.13)$$

$$\hat{x}(k+1/k) = \sum_{i=0}^{2n} W_i X_i(k+1/k) \quad (4.3.14)$$

## 4. Computation of the predicted covariance

$$P(k+1/k) = \sum_{i=0}^{2n} W_i [X_i(k+1/k) - \hat{x}(k+1/k)][X_i(k+1/k) - \hat{x}(k+1/k)]^T \quad (4.3.15)$$

## 5. Computation of the predicted observations

$$Y_i(k+1/k) = h(X_i(k+1/k), u(k), k) \quad (4.3.16a)$$

$$\hat{y}(k+1/k) = \sum_{i=0}^{2n} W_i Y_i(k+1/k) \quad (4.3.16b)$$

## 6. Computation of the observation's covariance

$$P_{yy}(k+1/k) = W_0 [Y_0(k+1/k) - \hat{y}(k+1/k)][Y_0(k+1/k) - \hat{y}(k+1/k)]^T + W_i \sum_{i=1}^{2n} [Y_i(k+1/k) - Y_0(k+1/k)][Y_i(k+1/k) - Y_0(k+1/k)]^T \quad (4.3.17)$$

7. Finally, computation of the cross correlation matrix

$$P_{xy}(k+1/k) = W_0 [X_0(k+1/k) - \hat{x}(k+1/k)] [Y_0(k+1/k) - \hat{y}(k+1/k)]^T + W_i \sum_{i=1}^{2n} [X_i(k+1/k) - X_0(k+1/k)] [Y_i(k+1/k) - Y_0(k+1/k)]^T \quad (4.3.18)$$

The filter gain is then computed by substituting eqn. (4.3.16), (4.3.17) and (4.3.18) into (4.3.7). The state vector  $\hat{x}(k+1/k+1)$  is updated by using Eq. (4.3.3) with Kalman gain and innovation values. The covariance matrix of the innovation process is computed by using eqn. (4.3.6) and (4.3.17).

The values of the weights, it means that the selection of the  $\kappa$  value affects directly the estimation performance. The appropriate choice of the  $\kappa$  reinforces the estimation performance since the magnitude of the higher order errors are reduced, consequently the estimation error can be diminished by tuning the  $\kappa$  parameter [5]. The following Section 4.3.2 contains the implementations and the results of the EKF and UKF on the SACoTS in order to estimate the full state (angular rates and attitude) by using the IMU as a main sensor.

### 4.3.2 Full State Estimation of SACoTS

In this section, two types of Kalman filter used in the SACoTS Attitude Determination System are presented. Basically, two different full state estimation modes are prepared depending on the structure of the EKF and UKF algorithms. First EKF is applied to the system. Next UKF is implemented in order to obtain more accurate estimation performance. A summary of these modes, sensors and filter types used are given in the following Table 4-4.

**Table 4-4: SACoTS ADS Modes**

SACoTS ADS Modes	Sensors	Estimated State Vector	Kalman Filter
Mode-S1	RG + ACC	$\hat{x} = [\hat{\omega}_{IB}^B \quad \hat{q}]^T$	EKF
Mode -S2	RG + ACC	$\hat{x} = [\hat{\omega}_{IB}^B \quad \hat{q}]^T$	UKF

Monte Carlo analysis is implemented to the SACoTS system in order to determine the performance of the EKF and UKF by pointing out the statistical distribution characteristics of the estimation error of the angular rates and attitude. This Monte Carlo analysis is applied to the system given at Figure 4-4 after that estimation converged (approx. 10sec). Then, the mean values  $\mu_x$ , and the standard deviation values  $\sigma_x$  of the estimation error are obtained by running the system 5 minutes and 20 times for related ADS mode. A motion profile containing the sinusoidal and fixed attitude are selected for the purpose of determining the performance of the filter for both rich and fixed motion. The common system model, the explanation of the ADS modes including sensor measurement models and filter algorithms are given respectively in the following sections.

***System Model:***

System model used in filter is derived from SACoTS motion model. The following equations are used to predict the estimated state vector and covariance matrix.

1. State vector prediction

The system model is used on the prediction of the estimated state. The rotational motion and attitude differential equations in discrete time are given as follows:

$$\hat{x}_{k+1,k} = \hat{x}_{k,k} + \int_k^{k+1} f_k(\hat{x}_{k,k}, k) dt \quad (4.3.19)$$

where,

$$\hat{x} = \begin{bmatrix} \hat{\omega}_{IB}^B & \hat{q} \end{bmatrix}^T \quad (4.3.20)$$

$$\dot{\hat{\omega}}_{IB}^B = I^{-1} \left( -\tilde{\omega}_{IB}^B I \hat{\omega}_{IB}^B + \tau^B \right); \text{ let } \hat{\omega}_{IB}^B \equiv \hat{\omega} \quad (4.3.21a)$$

$$\hat{\omega}_{k+1,k} = \hat{\omega}_{k,k} + \int_k^{k+1} \dot{\hat{\omega}}_{k+1,k} dt \quad (4.3.21b)$$

$$\dot{\hat{q}} = \frac{1}{2} \hat{\Omega}_{NB}^B \hat{q} \quad (4.3.22a)$$

$$\hat{q}_{k+1,k} = \hat{q}_{k,k} + \int_k^{k+1} \dot{\hat{q}}_{k+1,k} dt \quad (4.3.22b)$$

## 2. Covariance matrix prediction

The linearized system model is used on the prediction of the system covariance matrix and this matrix is propagated by adding the system noise covariance matrix as follows:

$$P_{k+1,k} = \Phi_{k+1,k} P_{k,k} \Phi_{k+1,k}^T + Q \quad (4.3.23)$$

where,

$$\Phi_{k+1,k} \approx \left( I + F_{k+1,k} \cdot \Delta t \right) \quad (4.3.24)$$

$$F_{k+1,k} = \frac{\partial f_k \left( \hat{x}_{k+1,k}, k \right)}{\partial \hat{x}_{k+1,k}} \quad (4.3.25)$$

Hereafter this point, the measurement models, steps of the Kalman filters and the results of the simulations are given respectively for each SACoTS ADS mode.

#### 4.3.2.1 SACoTS ADS Mode-s1

This section presents the measurement model used in EKF, the steps of the EKF algorithms and the simulation results. The estimates stated vector is  $\hat{x} = [\hat{\omega}_{IB}^B \quad \hat{q}]^T$  that given in the Eq. (4.320) and the sensor packet is IMU containing 3 axis rate gyros and 3 axis accelerometers.

##### **Measurement Model:**

The measurements equations are derived from the rate gyros and accelerometers models given in the following equations:

$$z_{RG} = \omega + v = h_{RG}(x) + \beta + \eta_v \quad (4.3.26)$$

$$z_{ACC} = \dot{\tilde{\omega}} r_{acc} + \tilde{\omega}(\tilde{\omega} r_{acc}) - gA^T [0 \quad 0 \quad 1]^T + w = h_{ACC}(x) + w \quad (4.3.27)$$

##### **Extended Kalman Filter Algorithm:**

In this section the steps of the EKF algorithms are not given again in order to avoid repetition. The detailed explanations about the EKF steps can be seen at section 3.1.3. Here, the sensor noise covariance matrix and measurement matrix used in EKF are given respectively for rate gyros and accelerometers.

$$R_{MOD\_S1} = \begin{bmatrix} I_{3 \times 3} \cdot R_{RG} & 0_{3 \times 3} \\ 0_{3 \times 3} & I_{3 \times 3} \cdot R_{ACC} \end{bmatrix} \quad (4.3.28)$$

$$H_{RG} = \left. \frac{\partial h_{RG}(x)}{\partial x} \right|_i = \begin{bmatrix} 1 & 0 & 0 \\ 0 & 1 & 0 \\ 0 & 0 & 1 \end{bmatrix} \quad (4.3.29)$$

$$H_{ACC} = \frac{\partial h_{ACC}(x)}{\partial x} \Big|_i = -2 \begin{bmatrix} \hat{q}_3 & \hat{q}_4 & \hat{q}_1 & \hat{q}_2 \\ -\hat{q}_4 & \hat{q}_3 & \hat{q}_2 & -\hat{q}_1 \\ -\hat{q}_1 & -\hat{q}_2 & \hat{q}_3 & \hat{q}_4 \end{bmatrix} \quad (4.3.30)$$

$$z = HX = \begin{bmatrix} H_{RG} & 0_{3 \times 4} \\ 0_{3 \times 3} & H_{ACC} \end{bmatrix} \begin{bmatrix} \hat{\omega}_{(3 \times 1)} \\ \hat{q}_{(4 \times 1)} \end{bmatrix} \rightarrow H_{MOD\_S1} = \begin{bmatrix} H_{RG} & 0_{3 \times 4} \\ 0_{3 \times 3} & H_{ACC} \end{bmatrix} \quad (4.3.31)$$

### Simulation Results:

The SACoTS ADS Mode-s1 simulation is run at 10 Hz sampling time during 5 minutes. The measurement sampling time for the each sensor also is selected as 10 Hz. The real and estimated states and estimation errors are given respectively in the following Figure 4-5, Figure 4-6 and Figure 4-7.

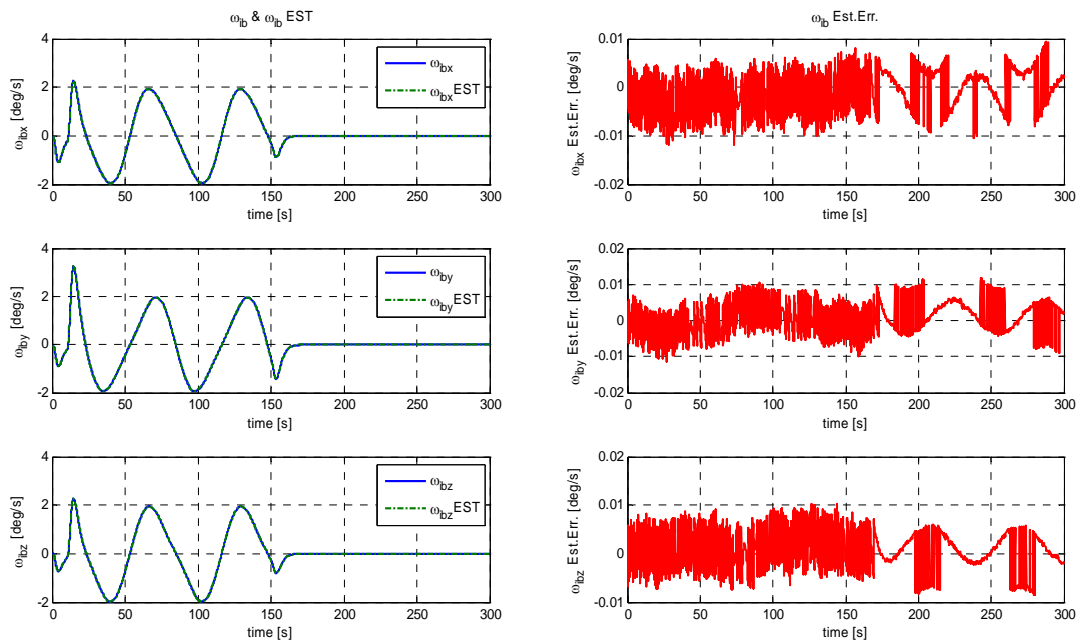
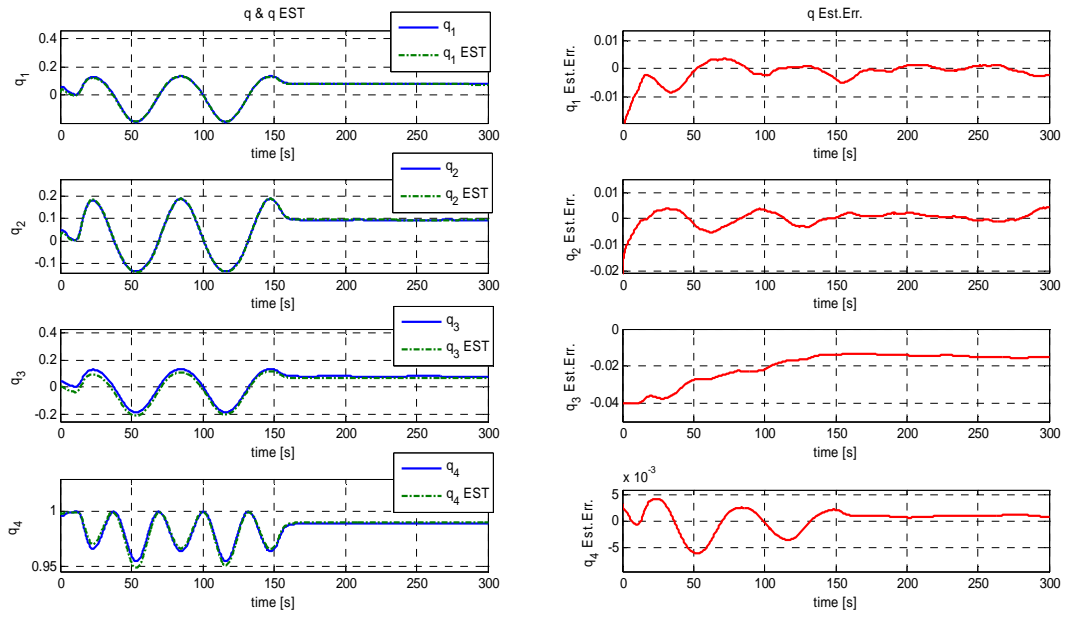
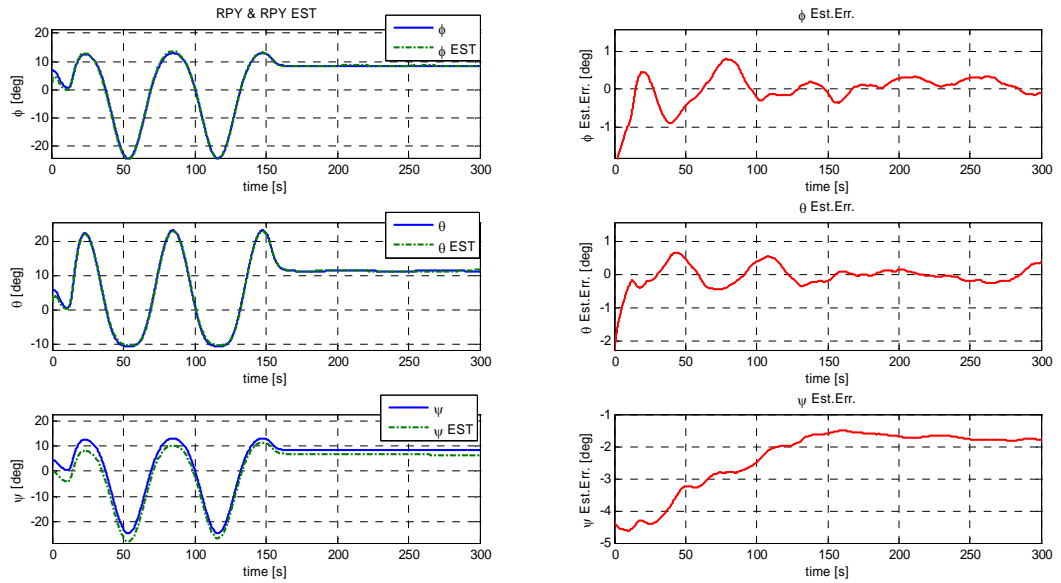


Figure 4-5: Mode-s1 Real and Estimated Angular Rates



**Figure 4-6: Mode-s1 Real and Estimated Quaternions**



**Figure 4-7: Mode-s1 Real and Estimated RPY Angles**

The results of Mode-s1 show that the estimation errors for both roll ( $\phi$ ) and pitch ( $\theta$ ) angles are about  $0.5^\circ$  and it can be accepted as a successful performance for this

level of accuracy and for nonexistence of the divergence problem during the attitude hold maneuver. However, there is a significant bias problem on the third axis, yaw ( $\psi$ ) angle estimation. This bias occurs due to the absence of reference measurement on third axis. As mentioned above in section 4.3, three axis accelerometers are used as a reference sensor by comparing the direction of measured acceleration vector and the direction of the gravity vector; but it is impossible to measure the rotation around the gravity vector. An additional reference sensor mounted on this third axis shall overcome this problem.

The statistical analysis called Monte Carlo analysis also is implemented to the system in order to determine the exact estimation performance of Mod-s1. The statistical results are taken by running simulation 20 times for 5 minutes at 10 Hz. The mean  $\mu_{\hat{x}}$ , and the standard deviation  $\sigma_{\hat{x}}$  of the estimation errors are given in the Figure 4-8 to Figure 4-13 and Table 4-5.

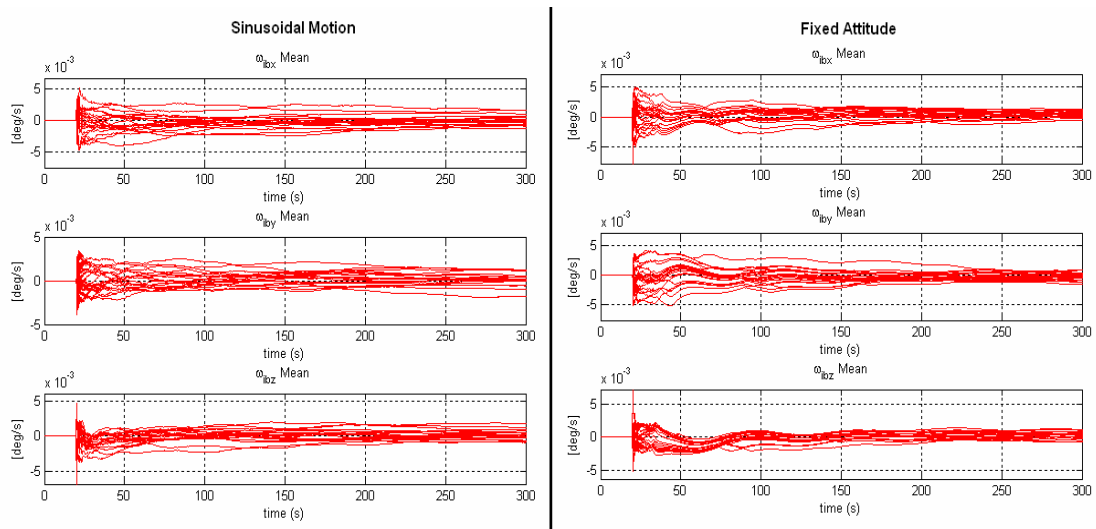


**Figure 4-8: Mode-s1 Mean of the Angular Rate Estimation Error**

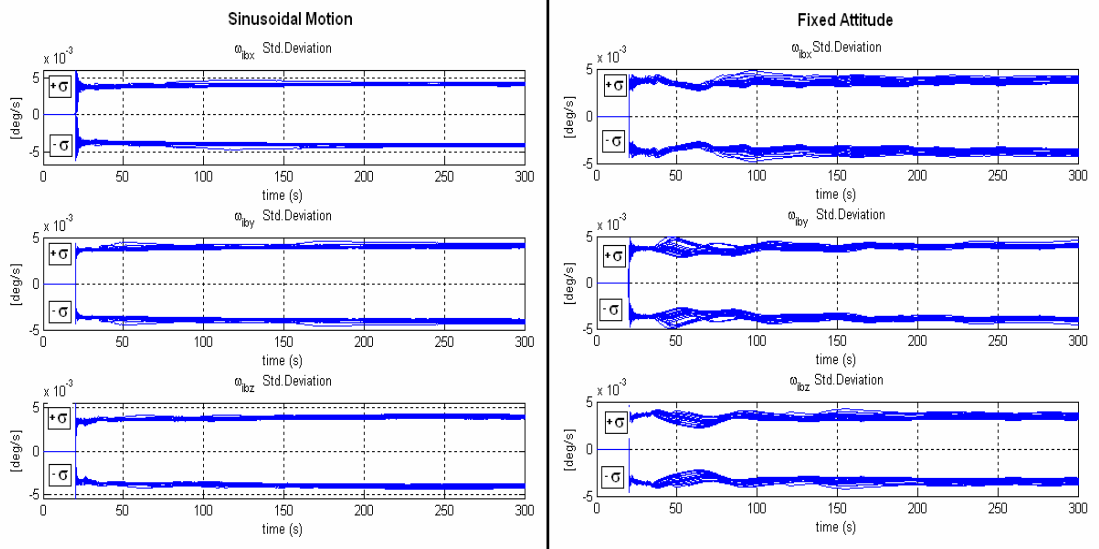


**Figure 4-9: Mode-s1 Standard Deviation of the Angular Rate Estimation Error**

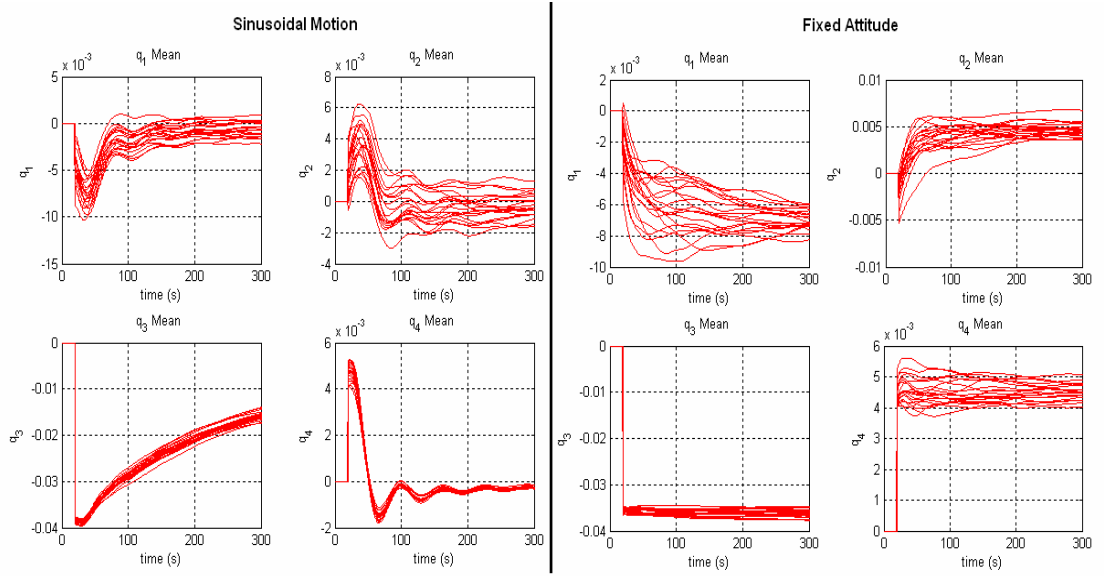


**Figure 4-10: Mode-s1 Mean of the Quaternions Estimation Error**

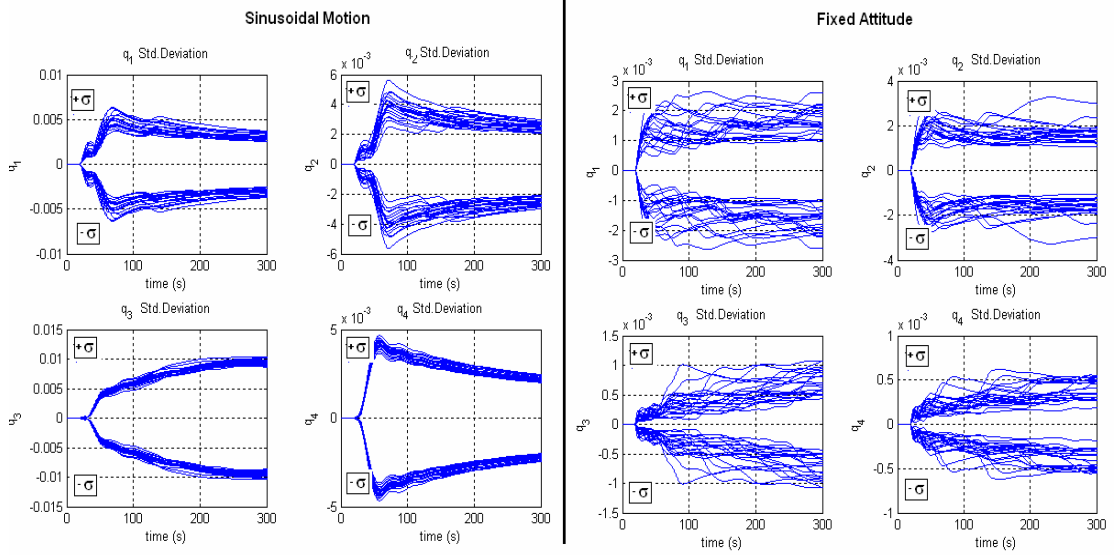


**Figure 4-11: Mode-s1 Standard Deviation of the Quaternions Estimation Error**

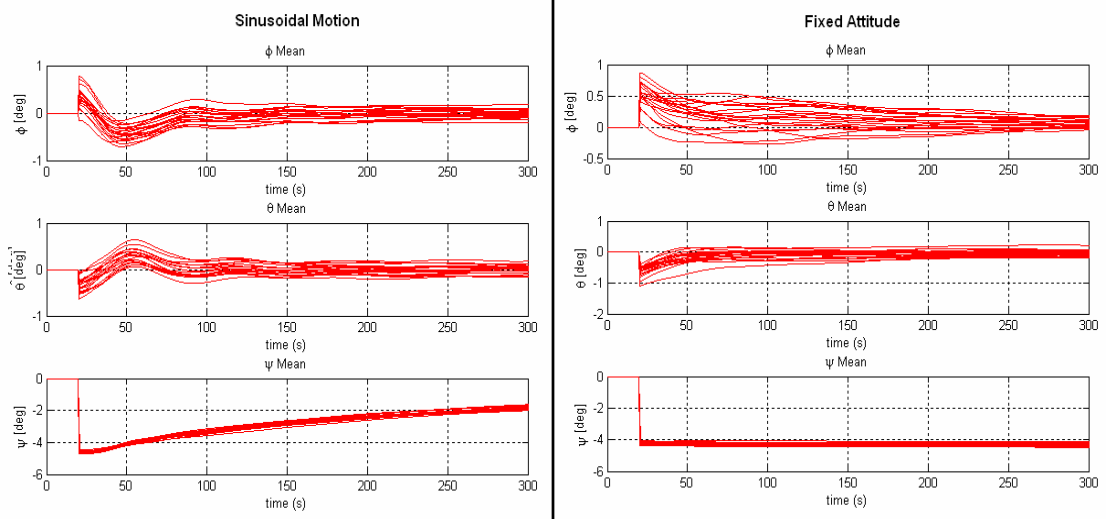


**Figure 4-12: Mode-s1 Mean of the RPY Angles Estimation Error**

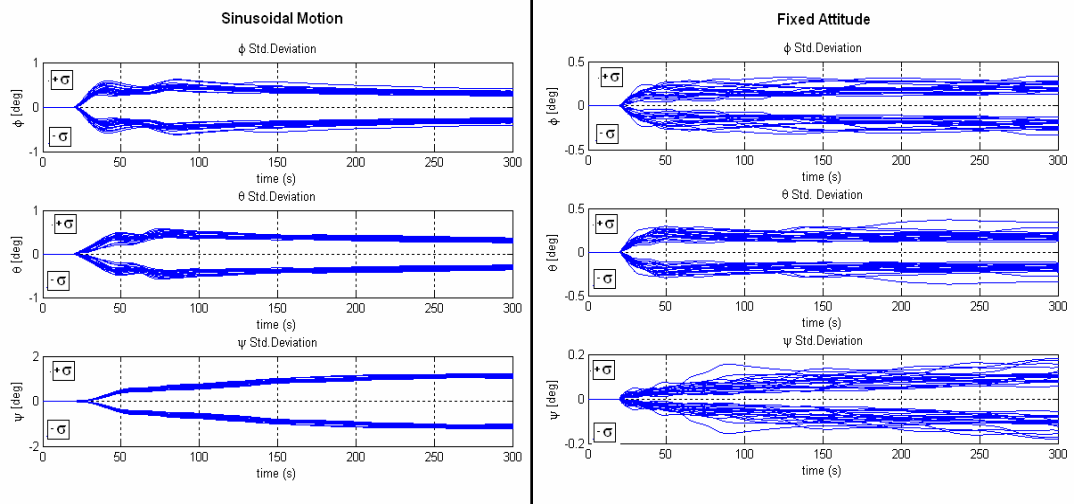


**Figure 4-13: Mode-s1 Standard Deviation of the RPY Angles Estimation Error**

**Table 4-5: Mode-s1 Statistical Results of the Estimation Error**

	<b>Sinusoidal Motion</b>		<b>Fixed Attitude</b>	
$\hat{X}_{err}$	$\mu_{\hat{X}}$	$\sigma_{\hat{X}}$	$\mu_{\hat{X}}$	$\sigma_{\hat{X}}$
$\hat{\omega}_{IB\_X}^B err. (^\circ/sec)$	0.0000	0.0040	0.0005	0.0038
$\hat{\omega}_{IB\_Y}^B err. (^\circ/sec)$	0.0002	0.0040	-0.0004	0.0040
$\hat{\omega}_{IB\_Z}^B err. (^\circ/sec)$	0.0002	0.0040	0.0003	0.0034
$\hat{q}_{1err}$	-0.0006	0.0031	-0.0070	0.0017
$\hat{q}_{2err}$	-0.0003	0.0027	0.0047	0.0017
$\hat{q}_{3err}$	-0.0158	0.0096	-0.0362	0.0007
$\hat{q}_{4err}$	-0.0003	0.0022	0.0045	0.0004
$\hat{\phi}_{err} (^\circ)$	-0.0116	0.3141	0.0683	0.2161
$\hat{\theta}_{err} (^\circ)$	-0.0041	0.3183	-0.0320	0.1933
$\hat{\psi}_{err} (^\circ)$	-1.8384	1.1190	-4.3171	0.1113

Consequently Monte Carlo results point out that the estimation performance for this Mode-s1 is successful by using only IMU, and there are no divergence and instability problems on the estimation. However, it can be clearly observed that there is a substantial error on the yaw ( $\psi$ ) angle estimation since there is no reference sensor

along this third axis. EKF results have different estimation accuracy for different motion types. In order to avoid this problem an additional reference sensor that uses a different kind of reference source can be added to the system. Here it must be stated that the mounting position of this second sensor on the system and the position of the reference source are very important. For example when a sun sensor is selected as a second reference sensor, the light source of this sensor should not be mounted on the same direction with gravity vector, otherwise the absence of the measurement problem will occur again for the third axis measurements.

The bias problem that occurs on the yaw angle estimation is studied to be compensated by using a more complex estimation algorithm called UKF in Mode-s2. The details and the results of this Mode-s2 are given in the following section.

#### 4.3.2.2 *SACoTS ADS Mode-s2*

This section presents the measurement model used in UKF, the steps of the UKF algorithm and the estimation performance of this filter. Here, again the subject is to estimate state vector  $\hat{x} = [\hat{\omega}_{IB}^B \quad \hat{q}]^T$  by using IMU measurements.

##### ***Measurement Model:***

UKF is an algorithm that provides to use nonlinear measurement models in the filter (See Section 4.4.1). These linear and nonlinear sensor measurement equations are derived for each sigma point that is used in UKF. The rate gyros and accelerometer measurement models and UKF predicted observations expression are listed again in the following equations

$$\begin{aligned}
 z(k+1, k) &= \begin{bmatrix} z_{RG}(k+1, k) \\ z_{ACC}(k+1, k) \end{bmatrix} \\
 &= \begin{bmatrix} h_{RG}(\hat{X}_i(k+1, k), u(k), k) \\ h_{ACC}(\hat{X}_i(k+1, k), u(k), k) \end{bmatrix} = h(\hat{X}_i(k+1, k), u(k), k)
 \end{aligned} \tag{4.3.32}$$

$$\hat{z}(k+1/k) = \sum_{i=0}^{2n} W_i Z_i(k+1/k) \quad (4.3.33)$$

where,  $\hat{X}_i(k+1, k)$  are the sigma point derived from  $X_i(k/k) = \sigma_i(k/k) + \hat{x}(k/k)$  Eq. (4.3.11).

***Unscented Kalman Filter Algorithm:***

The details about the UKF formulization is given in the Section 4.3.1 and for this reason, here only the sensor noise covariance matrix is given by the following equation:

$$R_{MOD\_S2} = \begin{bmatrix} I_{3 \times 3} R_{RG} & 0_{3 \times 3} \\ 0_{3 \times 3} & I_{3 \times 3} R_{ACC} \end{bmatrix} \quad (4.3.34)$$

***Simulation Results:***

The SACoTS ADS simulation is run at 10 Hz sampling time during 5 minutes for Mode-s2. The real and estimated states and estimation errors are given respectively in the following Figure 4-14, Figure 4-15 and Figure 4-16.

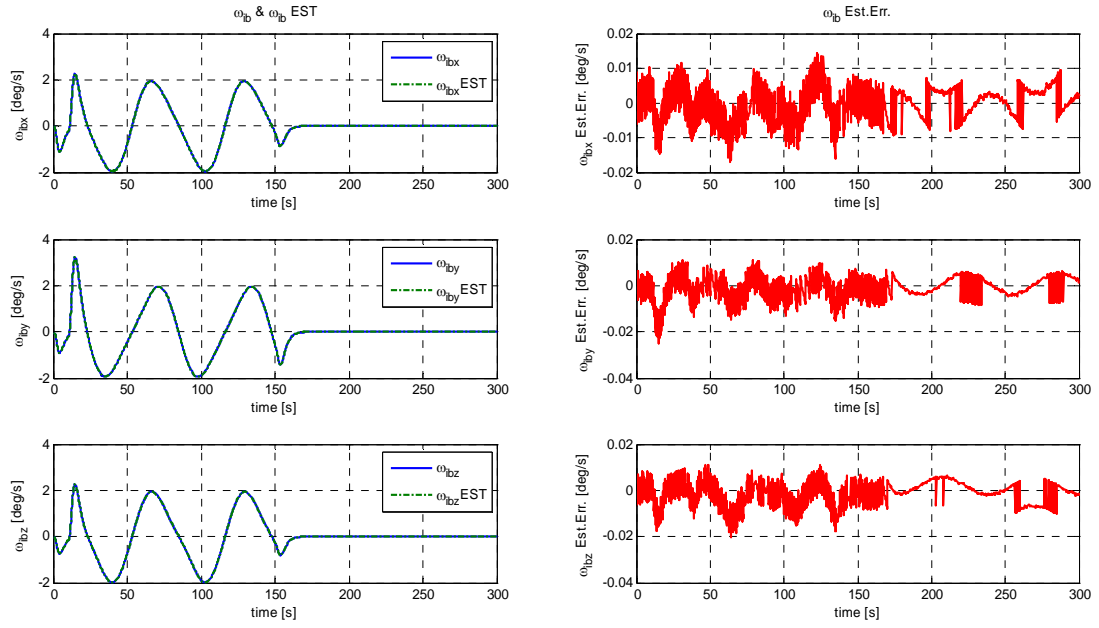


**Figure 4-14: Mode-s2 Real and Estimated Angular Rates**

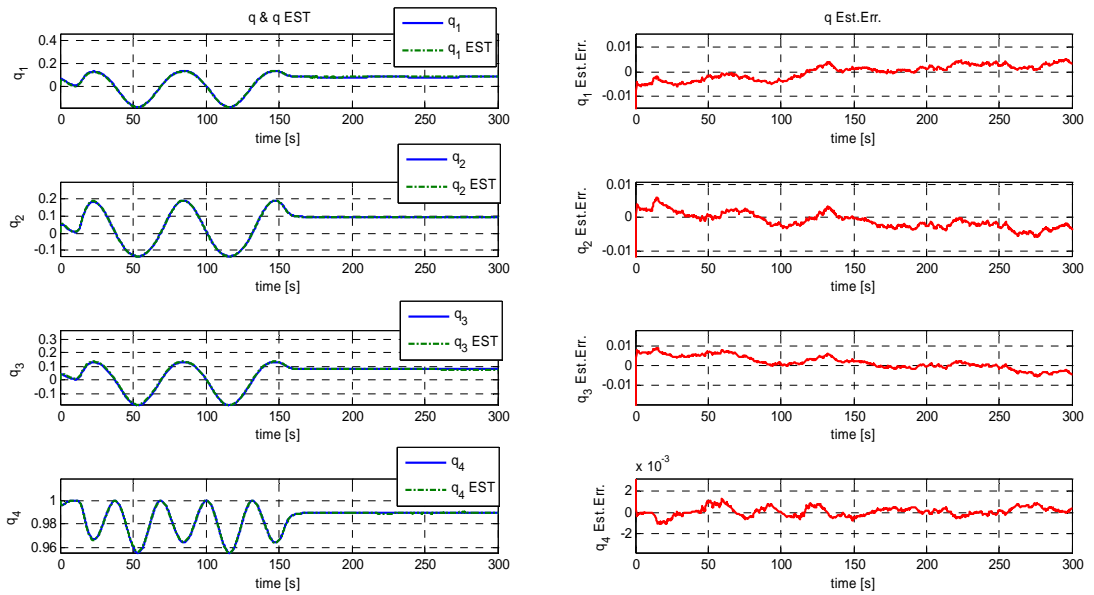


**Figure 4-15: Mode-s2 Real and Estimated Quaternions**

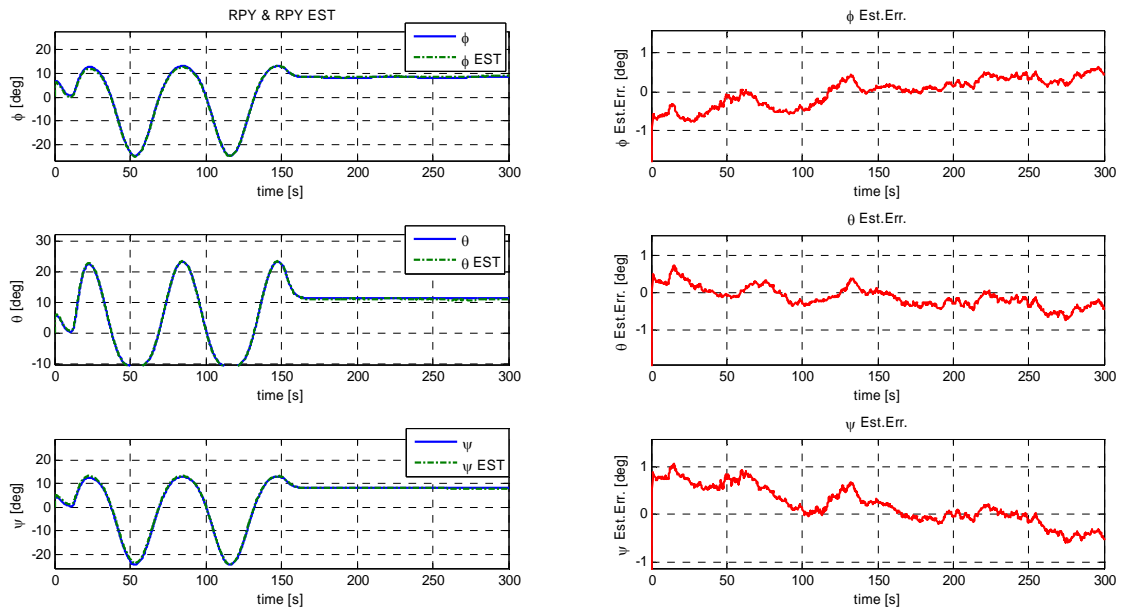


**Figure 4-16: Mode-s2 Real and Estimated RPY Angles**

Regarding to the Mod-s2 simulation results, it can be seen that UKF has a successful estimation performance since there is no divergence or high level accuracy problem on the estimation. Furthermore, UKF does not display a large error in the yaw angle  $\psi$  estimation. Here one additional advantage of the UKF also is obtained from the simulation results: Since the UKF uses nonlinear system model and nonlinear measurement model on the computations, the estimation error signal does not show different behaviors for different maneuver types. Here, the same orders of errors are obtained for both sinusoidal and attitude hold maneuver and these values are approximately  $0.5^\circ$  for each attitude angles.

Monte Carlo analysis is implemented to the system and the statistical results are taken by running simulation 20 times for Mode-s2. The mean  $\mu_{\hat{x}}$  and the standard deviation  $\sigma_{\hat{x}}$  of the estimation errors are given in the figures Figure 4-17 to Figure 4-22 and Table 4-6.

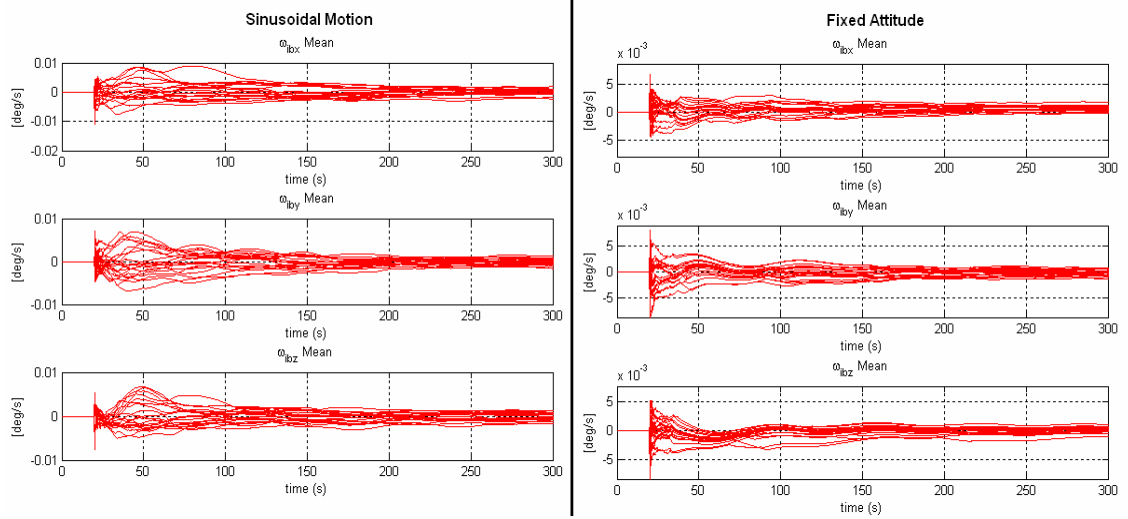


**Figure 4-17: Mode-s2 Mean of the Angular Rate Estimation Error**

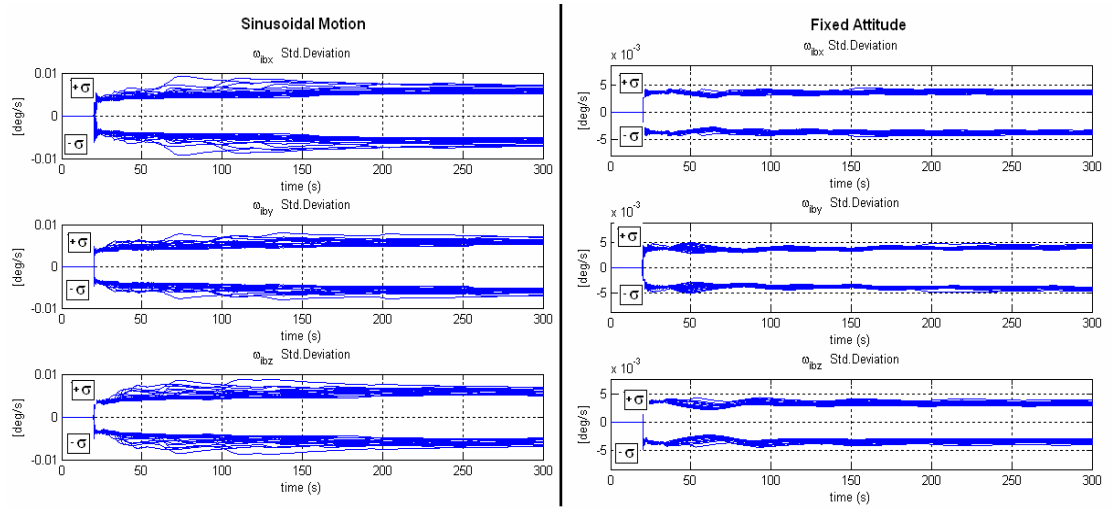


**Figure 4-18: Mode-s2 Standard Deviation of the Angular Rate Estimation Error**

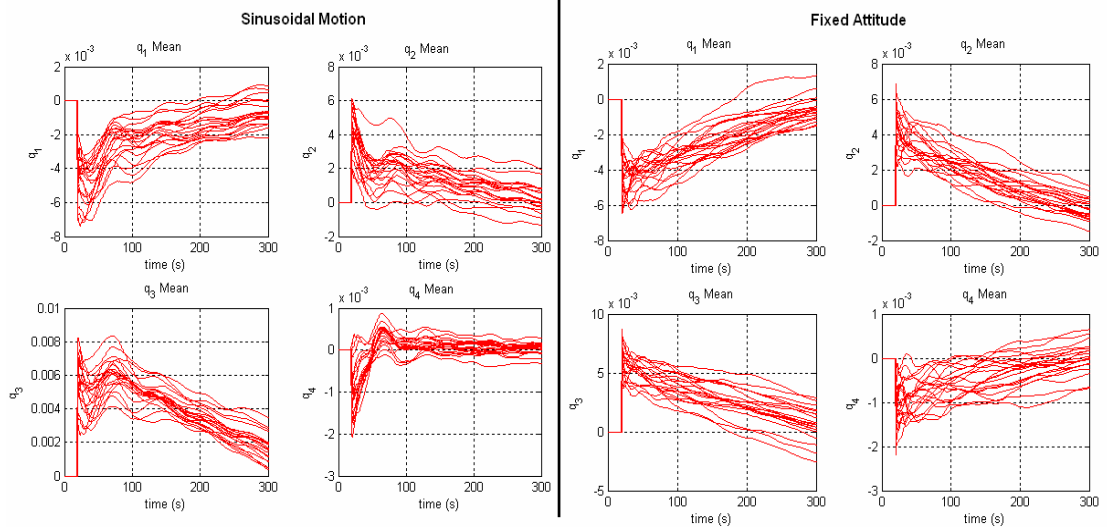


**Figure 4-19: Mode-s2 Mean of the Quaternions Estimation Error**

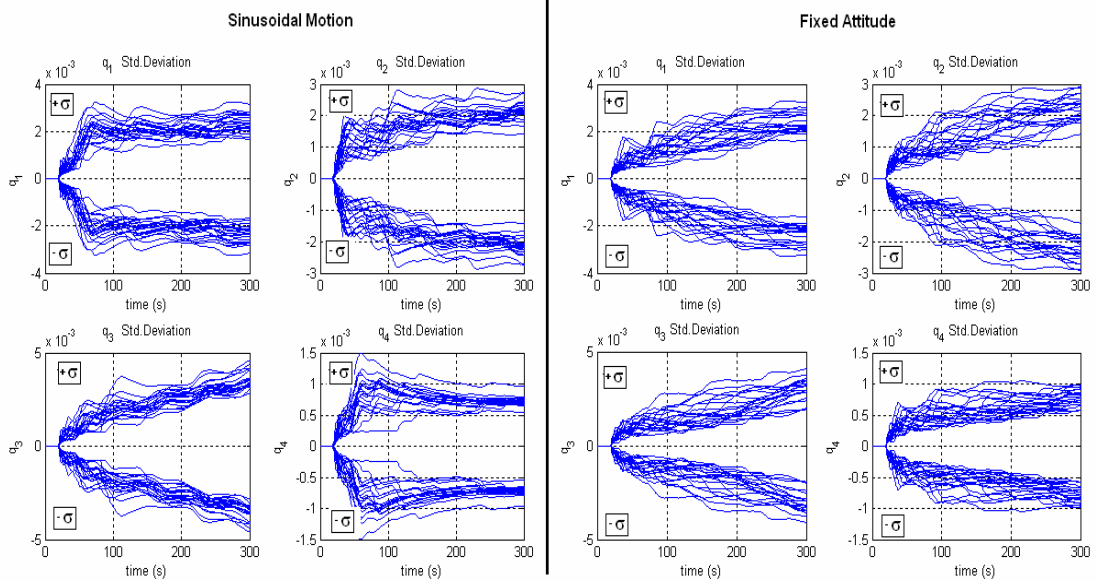


**Figure 4-20: Mode-s2 Standard Deviation of the Quaternions Estimation Error**

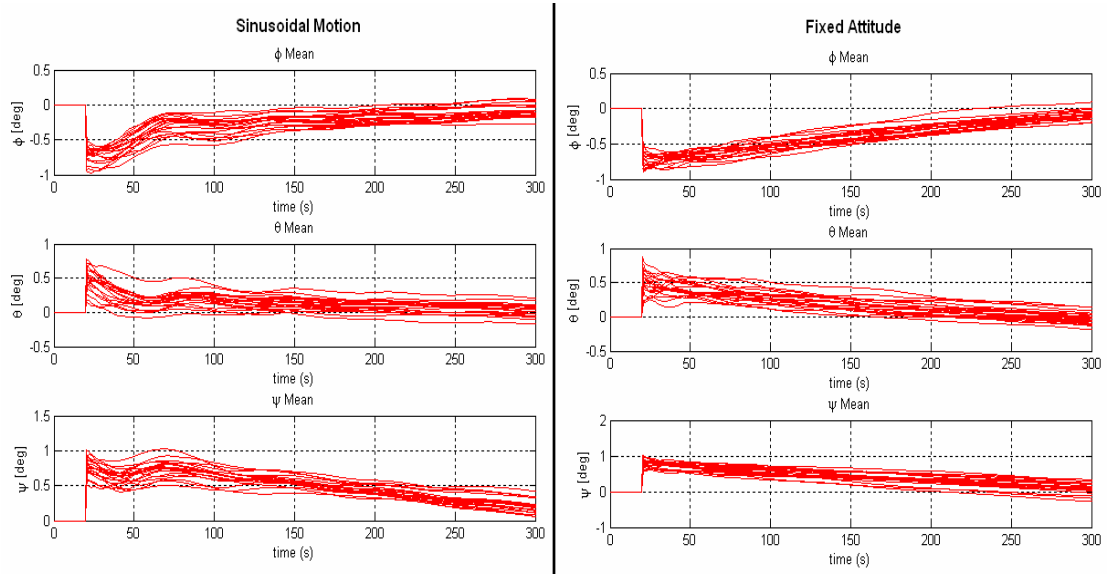


**Figure 4-21: Mode-s2 Mean of the RPY Angles Estimation Error**

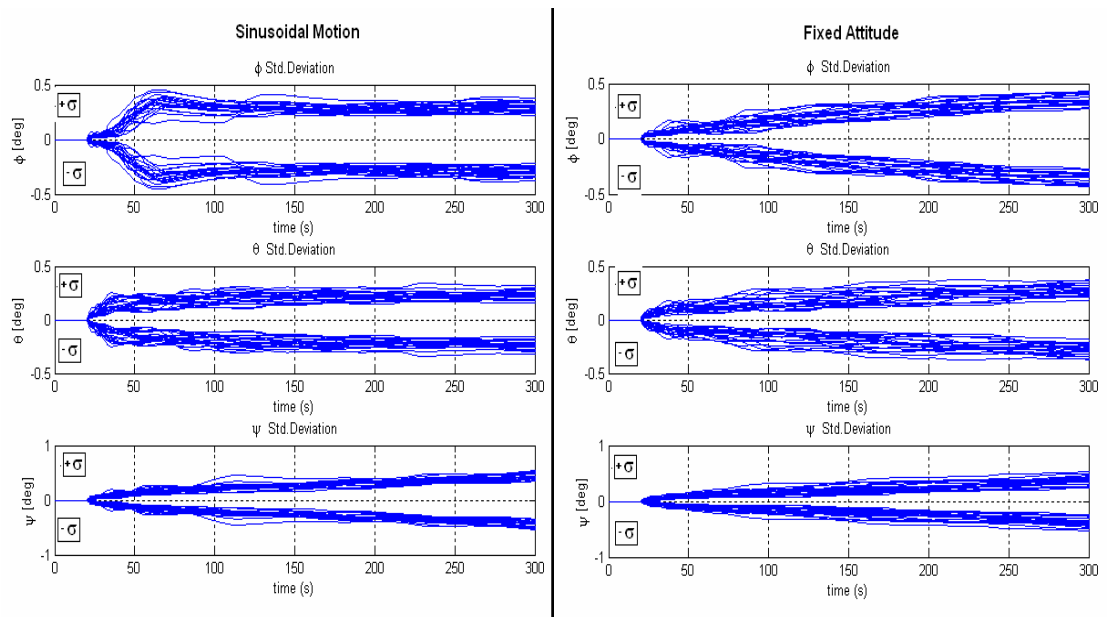


**Figure 4-22: Mode-s2 Standard Deviation of the RPY Angles Estimation Error**

Consequently Monte Carlo results show that the estimation performance for this Mode-s2 is successful for both sinusoidal and fixed attitude motion profile since there are no divergence, instability and offset problems on state estimation. A better estimation performance is achieved due to the usage of the nonlinear system and measurements model on the UKF algorithms and by tuning the UKF parameter  $\kappa$  the bias problem on the yaw angle estimation is resolved.

**Table 4-6: Mode-s2 Statistical Results of the Estimation Error**

$\hat{X}_{err}$	Sinusoidal Motion		Fixed Attitude	
	$\mu_{\hat{x}}$	$\sigma_{\hat{x}}$	$\mu_{\hat{x}}$	$\sigma_{\hat{x}}$
$\hat{\omega}_{IB\_X}^B err. (^{\circ}/sec)$	0.0001	0.0061	0.0007	0.0037
$\hat{\omega}_{IB\_Y}^B err. (^{\circ}/sec)$	-0.0001	0.0060	0.0000	0.0041
$\hat{\omega}_{IB\_Z}^B err. (^{\circ}/sec)$	-0.0001	0.0060	0.0002	0.0034
$\hat{q}_{1err}$	-0.0007	0.0023	-0.0006	0.0024
$\hat{q}_{2err}$	0.0002	0.0022	-0.0002	0.0022
$\hat{q}_{3err}$	0.0017	0.0036	0.0006	0.0030
$\hat{q}_{4err}$	0.0000	0.0007	0.0000	0.0008
$\hat{\phi}_{err} (^{\circ})$	-0.0875	0.2974	-0.0886	0.3537
$\hat{\theta}_{err} (^{\circ})$	0.0188	0.2428	-0.0238	0.2855
$\hat{\psi}_{err} (^{\circ})$	0.1986	0.4327	0.0977	0.3844

A comparison between the EKF and UKF algorithms used on the SACoTS system is given in the following conclusion section with some comments.

#### 4.4 Conclusion

In this chapter, *Kalman Filter Based Attitude Determination System* that is implemented for *Satellite Attitude Control Test Setup* is presented. This chapter

contains also SACoTS motion model, IMU measurement model used in the system and the attitude determination algorithms.

In the ADS system of the SACoTS, two types of Kalman filters, EKF and UKF are implemented to the system. The main objective of this chapter was to determine the performance comparison between these filters and to obtain relatively accurate estimation without using additional reference sensor on the system. The results obtained from the statistical analysis of the EKF and UKF are summarized in the following Table 4-7 in order to compare the performance of these two filters.

**Table 4-7: The Performance Comparison Table of the EKF and UKF**

	Sinusoidal Motion Profile				Fixed Attitude			
	$\mu_{\hat{x}}$	$\mu_{\hat{x}}$	$\sigma_{\hat{x}}$	$\sigma_{\hat{x}}$	$\mu_{\hat{x}}$	$\mu_{\hat{x}}$	$\sigma_{\hat{x}}$	$\sigma_{\hat{x}}$
	( $^{\circ}$ )	( $^{\circ}$ )	( $^{\circ}$ )	( $^{\circ}$ )	( $^{\circ}$ )	( $^{\circ}$ )	( $^{\circ}$ )	( $^{\circ}$ )
	EKF	UKF	EKF	UKF	EKF	UKF	EKF	UKF
$\hat{\phi}_{err}$	-0.0116	-0.0875	0.3141	0.2974	0.0683	-0.0886	0.2161	0.3537
$\hat{\theta}_{err}$	-0.0041	0.0188	0.3183	0.2428	-0.0320	-0.0238	0.1933	0.2855
$\hat{\psi}_{err}$	-1.8384	0.1986	1.1190	0.4327	-4.3171	0.0977	0.1113	0.3844

The performances of the EKF and UKF are considered for both sinusoidal motion profile and fixed attitude. For sinusoidal motion profile, it can be seen that the EKF results are successful for roll angle and pitch angle estimation. The mean values of the estimation error are nearly zeros and the standard deviation of the estimation errors is about  $0.32^{\circ}$  for these first two attitude angles. However, the EKF is not sufficient for the yaw angle estimation. A constant offset is obtained on the estimation ( $\approx 1.85^{\circ}$ ) and an instability also can be observed as the  $\sigma$  values of the yaw angle estimation which is  $\approx 1.12^{\circ}$ . For attitude hold maneuvers, the estimation performance on roll and pitch angle increase to  $\approx 0.20^{\circ}$ , but on the contrary, an augmentation of the bias values on the yaw angle estimation is observed ( $\approx 4.3^{\circ}$ ) even if the related  $\sigma$  is decrease to  $\approx 0.1^{\circ}$  values.

The UKF estimation performance also is appreciated for both sinusoidal and attitude hold maneuver. Regarding to the statistical results, it is seen that UKF improves the estimation performance for sinusoidal motion profile. Especially, the bias problem occurred on the yaw angle estimation is resolved by using the additional tuning parameters of the UKF algorithm. The bias values of the estimation errors can be accepted as less than  $0.1^\circ$  for roll and pitch angle,  $0.2^\circ$  for yaw angle. The standard deviation values of the estimation errors also decrease to  $< 0.3^\circ$  for roll and pitch angle,  $< 0.5^\circ$  for yaw angle. For the attitude hold maneuver also there is a clear improvement on the bias problem that occurred on the yaw angle estimation. It is also observed that there is a little increment on the estimation error for all three attitude angles when considering the  $\sigma$  values. However, one important result obtained for UKF is that the performance of this filter is similar regardless of the motion types. Depending on the simulation results, it is seen that very close estimation errors characteristics are obtained for both kinds of the motion profiles. As mentioned above in section 4.3.1, EKF contains only first order Taylor series expansion in order to simulate the behavior of the nonlinear systems and measurements, but UKF uses the nonlinear models and this provides an advantage for nonlinear systems.

Consequently, regarding to the simulation results obtained for both EKF and UKF, it may be stated that UKF algorithms improves the estimation performance compared to the EKF. This improvement is achieved thanks to the usage of the nonlinear system and nonlinear motion models in the filter.

## **CHAPTER 5**

### **CONCLUSION**

The purpose of this thesis was to generate a Kalman filter based attitude determination algorithms for a hypothetical LEO satellite and for a ground based satellite attitude control test setup.

In order to estimate the angular rates of the satellite during the initial detumbling phase, and additionally to estimate the attitude during to orbital navigation, six different Kalman filter estimation algorithms, depending on six different sensor combinations called modes, are created. The performance of each mode is computed by applying Monte Carlo simulations and the success of various modes are compared to each other. The two important inferences are obtained from the results of the satellite ADS simulations. The first one is about the angular rate estimation at detumbling mode. Here the important point is the sampling rate of the system. Since the magnetometer measurements are very noisy compared to the other reference sensors, the sampling rate is chosen 1 Hz with a goal to catch the difference between two successive measurements. The rotation frequency of the satellite, the measurement frequency of the sensor and the frequency of the estimation system, all together are important factors that affect the estimation performance. For this reason it is very important to select the right sampling rate for the system. The second inference is about the reference sensor used in the system. Some reference sensors do not provide a sufficient attitude determination due to the absence of the sufficient measurement knowledge. It is shown that when satellite rotation vector and measured vector direction become parallel to each other, it is impossible to measure the rotation angle around this axis accurately. Furthermore, a divergence problem on estimation also occurs for the fixed attitude motions. These problems can only be resolved by adding another reference sensor to the system which use different measurements source. Finally, it can be stated that a powerful attitude determination

system for a hypothetical LEO satellite is created and it is shown that extended Kalman filter is an efficient method to fuse the sensor measurements to estimate the states of the spacecraft.

In the second part of this thesis, a cost-effective and relatively accurate attitude determination system is created for the satellite attitude control test setup by using only an IMU as a sensor suite. Two different types of Kalman filter algorithms, EKF and UKF, are implemented to this system. Here, the main objective was to obtain sufficiently accurate estimation performance without using an additional reference sensor on the system. Regarding to the simulation results, it is observed that UKF algorithms improves the estimation performance compared to the EKF due to the usage of the nonlinear system and nonlinear motion model in this filter.

In the future, other filtering methods and algorithms shall be examined. Their estimation accuracy versus the computational loads introduced as well as the associated convergence and divergence problems shall be investigated.

## REFERENCES

- [1] R.E. Kalman, "A new Approach to Linear Filtering and Prediction Problems", Transactions of the ASME- Journal of Basic Engineering, 82 (Series D):35-45, ASME, 1960.
- [2] W.H. Steyn, "A Multi-Mode Attitude Determination and Control System for Small Satellites", Dissertation presented for the Degree of Doctor of Philosophy (Engineering) at the University of Stellenbosch, December 1995
- [3] M.L. Psiaki, "Three-Axis Attitude Determination via Kalman Filtering of Magnetometer Data", AIAA, Vol.13, No.3, Page.506-514 , May-June 1990.
- [4] J.L.Crassidis, J.L. Junkins, "Optimal Estimation of Dynamic Systems", Chapman and Hall / CRC Press LLC, Boca Raton, 2004.
- [5] S.J. Julier, J.K. Uhlmann, H.F. Durrant-Whyte, "A New Approach for Filtering Nonlinear Systems", American Control Conference, Seattle, WA., June 1995.
- [6] V.S. Chernesky, "Development and Control of a Three-Axis Satellite Simulator for the Bifocal Relay Mirror Initiative", Naval Postgraduate School, Monterey California, December 2001.
- [7] J.L. Schwartz, "The distributed Spacecraft Attitude Control System Simulator: From design Concept to Decentralized Control", Blacksburg, Virginia, July 2004.
- [8] B.Kim, E. Velenis, P. Kriengsiri, P. Tsiotras, "Designing a Low-Cost Spacecraft Simulator", IEEE Control Systems Magazine, August 2003.

- [9] D. Jung, P. Tsiotras, “A 3-DoF Experimental Test-Bed for Integrated Attitude Dynamics and Control Research”, Georgia Institute of Technology, Atlanta, 2003.
- [10] S.S. Ose, “Attitude Determination for the Norwegian Student Satellite nCube”, Master’s Thesis, Department of Engineering Cybernetics, Norwegian University of Science and Technology, Norway, June 2004.
- [11] C. Wilkening , “Attitude Determination, Control and Stabilization”, Micro-Satellite Spartnik Team, San José State University, 2001
- [12] B. Wie, “Space Vehicle Dynamics and Control”, AIAA Education Series, Reston, Virginia, 1998
- [13] K. Svartveit, “Attitude Determination of nCube Satellite” Master’s Thesis, Department of Engineering Cybernetics, Norwegian University of Science and Technology, Norway, June 2003.
- [14] T. Lorentzen, “Attitude Control and Determination System for DTUusat1”, CubeSat Project, Department of Automation, Orsted DTU, February 2002.
- [15] J.R.Wertz, “Spacecraft Attitude Determination and Control”, Kluwer Academic Publishers, Dordrecht, Holland, 1988.
- [16] S. Merhav, “Aerospace Sensor Systems and Applications”, Springer-Verlag, New York, 1996.
- [17] Dr. W. Stockwell, “Bias Stability Measurement: Allan Varinace” Crossbow Technology, Inc.
- [18] G. Welch, G. Bishop, “An Introduction to the Kalman Filter”, University of North Carolina at Chapel Hill, Department of Computer Science,

Chapel Hill,NC, 2001.

- [19] P. Zarchan, H. Musoff, “Fundamentals of Kalman Filtering: A Practical Approach”, Progress in Astronautics and Aeronautics, Vol.190, AIAA, Virginia, 2000.
- [20] D.H. Titterton, J.L. Weston, “Strapdown Inertial NavigationTechnology”, second Edition, Paul Zarchan, AIAA, 2004.

## APPENDIX A

### DEFINITIONS AND NOTATIONS

Several different coordinate systems are used in order to describe the motion and the attitude of the satellite and to simulate the satellite's environment. Also, some notational expressions are required to define the orientation of the satellite, to develop the mathematics behind the sensor measurements and to build the Kalman Filters used at sensor fusion algorithms.

In this appendix, detailed explanations are given related to these references frames notations and to the mathematical tools used in this report.

#### A.1 Reference Frames

The detailed explanations of the different coordinate systems used throughout this report are given in this appendix. It is necessary to define these references frames with a view to represent the motion and the attitude of the spacecraft. Each Cartesian coordinate reference frames used in this document are an orthogonal, right-handed axis set [13].

##### A.1.1 Earth-Centered Inertial (ECI) Reference Frames

The ECI frame is assumed to be a non-accelerated frame used for navigation, which is fixed in space with respect to the fixed star defined by the axes  $X_i, Y_i, Z_i$ . The origin of the ECI is located at the center of the Earth with the  $z$ -axis pointing towards the North Pole. The  $x$ -axis is in the vernal equinox direction, the point where the plane of the Earth's orbit about the Sun, crosses the Equator going from south to north. The  $y$ -axis completes the right hand Cartesian coordinate system. The motions of the satellite, the velocity of the Orbit frame and the motion of the Sun is directly compared to this frame. The frame is denoted  $I$  [10].

### **A.1.2 Earth-Centered Earth Fixed (ECEF) Reference Frame**

The ECEF frame has its origin at the center of the Earth and axes which are fixed with respect to the Earth ( $X_e, Y_e, Z_e$ ). The  $x$ -axis lies along the intersection of the plane of the Greenwich meridian with the Earth's equatorial plane. The  $y$ -axis completes the right hand system. The earth frame rotates, with respect to the inertial frame, at a rate  $\omega_e = 7.2921 \times 10^{-5} \text{ rad/s}$  ( $15.0417^\circ/\text{h}$ ) about the  $z$ -axis. The ECEF frame can be used to express the geomagnetic field around the Earth, along with an orbit estimator to create a reference model. The frame is denoted  $E$  [10].

### **A.1.3 Orbit (ORB) Reference Frame**

The ORB frame has its origin at the mass center the satellite, defined by the axes  $X_o, Y_o, Z_o$ . This origin rotates relative to the ECI frame, with a rate of  $\omega_o$  depending on the altitude of the orbit. The  $z$ -axis lies towards the center of the Earth. The  $x$ -axis points in the direction of motion tangentially to the orbit. It is important to note that the *tangent* is perpendicular to the radius vector only in case of a circular orbit. In case of a elliptic orbits, the  $x$ -axis does not align with the satellite's velocity vector. The  $y$ -axis completes the right hand system. The satellite attitude is described in this frame. The orbit reference frame is denoted  $O$  [10].

### **A.1.4 Earth-Centered Orbit (ECOF) Reference Frame**

This is the frame in which the Keplerian elements are defined. The axes of this frame are expresses as  $X_{oc}, Y_{oc}, Z_{oc}$ . The ECOF frame has its origin at the center of the Earth. The  $x$ -axis lies towards perigee,  $y$ -axis along the semiminor-axis and  $z$ -axis perpendicular to the orbit plane. The earth centered orbit frame is denoted  $OC$  [10].

### A.1.5 Body (BODY) Reference Frame

The body reference frame is a right orthogonal axes system fixed in the center of the satellite body and defined by the axes  $X_b, Y_b, Z_b$ . This body frame shares its origin with the orbit frame and is denoted  $B$ . The nadir side of the satellite ( $z$ -axis) intended to point towards the Earth, and the last two axes,  $x$ -axis and  $y$ -axis, coincides with  $x$ -axis and  $y$ -axis of the Orbit frame when the satellite has an attitude of  $0^\circ$  in roll, pitch and yaw. The satellite dynamic equations are expressed in this coordinate system [10] [13].

## A.2 Attitude Representation

The formulation of satellite attitude dynamics involves knowledge of kinematics of a rigid body. Kinematics describes the orientation of a body which has a rotational motion. There are various mathematical representations used to define this orientation with respect to a reference frame. Through this section, three attitude representation methods are described. It is important to note that the attitude knowledge defined with each method can be stored within a computer and can be updated as the satellite rotates using the measurements of turn provided by the rate gyros [20].

### A.2.1 Direction Cosine Matrix

The Direction Cosine Matrix is a  $3 \times 3$  rotation matrix which describes the orientation between two frames. The rotation matrix  $C$  from frame  $A$  to  $B$  is denoted  $C_A^B$  or  $C_{B/A}$ . Consider reference frames  $A$  and  $B$  with a right-hand set of three orthogonal unit vectors. Basis vectors  $\{\vec{b}_1, \vec{b}_2, \vec{b}_3\}$  of  $B$  are expressed in terms of basis vectors  $\{\vec{a}_1, \vec{a}_2, \vec{a}_3\}$  of  $A$  as follows:

$$\begin{aligned}
\vec{b}_1 &= C_{11}\vec{a}_1 + C_{12}\vec{a}_2 + C_{13}\vec{a}_3 \\
\vec{b}_2 &= C_{21}\vec{a}_1 + C_{22}\vec{a}_2 + C_{23}\vec{a}_3 \\
\vec{b}_3 &= C_{31}\vec{a}_1 + C_{32}\vec{a}_2 + C_{33}\vec{a}_3
\end{aligned} \tag{A.2.1}$$

where  $C_{ij} \equiv \vec{b}_i \cdot \vec{a}_j$  is the cosine of the angle between  $\vec{b}_i$  and  $\vec{a}_j$ , and  $C_{ij}$  is simply called the *direction cosine*. Eq. (A.2.1) can be rewritten in a matrix form as follows:

$$\begin{bmatrix} \vec{b}_1 \\ \vec{b}_2 \\ \vec{b}_3 \end{bmatrix} = \begin{bmatrix} C_{11} & C_{12} & C_{13} \\ C_{21} & C_{22} & C_{23} \\ C_{31} & C_{32} & C_{33} \end{bmatrix} \begin{bmatrix} \vec{a}_1 \\ \vec{a}_2 \\ \vec{a}_3 \end{bmatrix} = C_A^B \begin{bmatrix} \vec{a}_1 \\ \vec{a}_2 \\ \vec{a}_3 \end{bmatrix} = C_{B/A} \begin{bmatrix} \vec{a}_1 \\ \vec{a}_2 \\ \vec{a}_3 \end{bmatrix} \tag{A.2.2}$$

where  $C_{B/A}$  is called *Direction Cosine Matrix (DCM)*. DCM is also called the *Rotation Matrix* or *Coordinate Transformation Matrix*.

The rotation matrix is also an orthonormal matrix because each set of basis vectors of  $A$  and  $B$  consists of orthogonal unit vectors and it is also orthogonal matrix because the product of  $C_{B/A} \cdot C_{B/A}^T$  is an identity matrix. So this orthonormality can be expressed as follows [12]:

$$C_{B/A} = (C_{A/B})^{-1} = (C_{A/B})^T \tag{A.2.3}$$

### A.2.2 Euler Angles

Euler angles method is a transformation from one coordinate frame to another and it is defined by three successive rotations about different axes taken in turn. For example, a transformation from references axis to a new coordinate frame may be expressed as follows:

a. Rotation through angle  $\psi$  about reference  $z$ -axis

$$C_1 = \begin{bmatrix} \cos \psi & \sin \psi & 0 \\ -\sin \psi & \cos \psi & 0 \\ 0 & 0 & 1 \end{bmatrix} \quad (\text{A.2.4})$$

b. Rotation through angle  $\theta$  about reference  $y$ -axis

$$C_2 = \begin{bmatrix} \cos \theta & 0 & -\sin \theta \\ 0 & 1 & 0 \\ \sin \theta & 0 & \cos \theta \end{bmatrix} \quad (\text{A.2.5})$$

c. Rotation through angle  $\phi$  about reference  $x$ -axis

$$C_3 = \begin{bmatrix} 1 & 0 & 0 \\ 0 & \cos \phi & \sin \phi \\ 0 & -\sin \phi & \cos \phi \end{bmatrix} \quad (\text{A.2.6})$$

where  $\psi, \theta, \phi$  are referred to as the Euler rotation angles.

For instance, a transformation from  $A$  reference frame to  $B$  reference frame may be expressed as the product of these three separate transformation as follows:

$$C_A^B = C_3 C_2 C_1 \quad (\text{A.2.7})$$

Similarly, the inverse transformation will give the rotation information from  $B$  reference frame to  $A$  reference frame, expressed as follows [20]:

$$C_B^A = C_1^T C_2^T C_3^T \quad (\text{A.2.8})$$

$$C_B^A = \begin{bmatrix} c\theta c\psi & -c\phi s\psi + s\phi s\theta c\psi & s\phi s\psi + c\phi s\theta c\psi \\ c\theta s\psi & c\phi c\psi + s\phi s\theta s\psi & -s\phi c\psi + c\phi s\theta s\psi \\ -s\theta & s\phi c\theta & c\phi c\theta \end{bmatrix} \quad (\text{A.2.9})$$

where;

$$c\alpha = \cos \alpha$$

$$s\alpha = \sin \alpha$$

### A.2.3 Quaternions

Although the Euler angles representation has a clear physical interpretation, unfortunately there is always a possibility to be at a singularity because of the trigonometric expressions which exist in the transformation matrix. To overcome the problem with singularities in the attitude representation, quaternions are used in computations.

The quaternion attitude representation allows a transformation from one coordinate frame to another to be effected by a single rotation ( $\gamma$ ) about a vector ( $\mu$ ) defined in the reference frame. The quaternion is a four element vector representation, the elements of which are functions of the orientation of a vector and the magnitude of the rotation.

$$q = \begin{bmatrix} q_1 \\ q_2 \\ q_3 \\ q_4 \end{bmatrix} = \begin{bmatrix} (\mu_x / \mu) \sin(\gamma / 2) \\ (\mu_y / \mu) \sin(\gamma / 2) \\ (\mu_z / \mu) \sin(\gamma / 2) \\ \cos(\gamma / 2) \end{bmatrix} \quad (\text{A.2.10})$$

The unit quaternions satisfy the constraint  $q^T q = 1$ , or

$$q_1^2 + q_2^2 + q_3^2 + q_4^2 = 1 \quad (\text{A.2.11})$$

For instance, a transformation from  $B$  reference frame to  $A$  reference frame by using quaternions can be given as follows [20]:

$$C_B^A = \begin{bmatrix} q_1^2 - q_2^2 - q_3^2 + q_4^2 & 2(q_1q_2 - q_3q_4) & 2(q_1q_3 + q_2q_4) \\ 2(q_1q_2 + q_3q_4) & -q_1^2 + q_2^2 - q_3^2 + q_4^2 & 2(q_2q_3 - q_1q_4) \\ 2(q_1q_3 - q_2q_4) & 2(q_2q_3 + q_1q_4) & -q_1^2 - q_2^2 + q_3^2 + q_4^2 \end{bmatrix} \quad (\text{A.2.12})$$

#### A.2.4 Relationships Between DCM, Euler Angles and Quaternions

As seen in the previous sections, the direction cosines may be expressed in terms of Euler angles or quaternions. In the following Eq. (2.2.13), the relationship between DCM, Euler angles and quaternions for the rotation from frame  $B$  to  $A$  is given:

$$C_B^A = \begin{bmatrix} c\theta c\psi & -c\phi s\psi + s\phi s\theta c\psi & s\phi s\psi + c\phi s\theta c\psi \\ c\theta s\psi & c\phi c\psi + s\phi s\theta s\psi & -s\phi c\psi + c\phi s\theta s\psi \\ -s\theta & s\phi c\theta & c\phi c\theta \end{bmatrix} \quad (\text{A.2.13})$$

$$\begin{bmatrix} q_1^2 - q_2^2 - q_3^2 + q_4^2 & 2(q_1q_2 - q_3q_4) & 2(q_1q_3 + q_2q_4) \\ 2(q_1q_2 + q_3q_4) & -q_1^2 + q_2^2 - q_3^2 + q_4^2 & 2(q_2q_3 - q_1q_4) \\ 2(q_1q_3 - q_2q_4) & 2(q_2q_3 + q_1q_4) & -q_1^2 - q_2^2 + q_3^2 + q_4^2 \end{bmatrix}$$

When the elements of the above Eq. (A.2.13) are compared, it can be noticed that Euler angles may be expressed in terms of direction cosines or quaternions, and also similarly, the quaternion elements may be written directly in terms of Euler angles or direction cosines. In the following equations some of these relationships are summarized [20]:

***Quaternions expressed in terms of Direction Cosines***

$$\begin{aligned}
 q_1 &= \frac{1}{4q_4} (C_{B\ 32}^A - C_{B\ 23}^A) & q_2 &= \frac{1}{4q_4} (C_{B\ 13}^A - C_{B\ 31}^A) \\
 q_3 &= \frac{1}{4q_4} (C_{B\ 21}^A - C_{B\ 12}^A) & q_4 &= \frac{1}{2} \sqrt{1 + C_{B\ 11}^A + C_{B\ 22}^A + C_{B\ 33}^A}
 \end{aligned} \tag{A.2.14}$$

***Quaternions expressed in terms of Euler angles***

$$\begin{aligned}
 q_4 &= \cos \frac{\phi}{2} \cos \frac{\theta}{2} \cos \frac{\psi}{2} + \sin \frac{\phi}{2} \sin \frac{\theta}{2} \sin \frac{\psi}{2} \\
 q_1 &= \sin \frac{\phi}{2} \cos \frac{\theta}{2} \cos \frac{\psi}{2} - \cos \frac{\phi}{2} \sin \frac{\theta}{2} \sin \frac{\psi}{2} \\
 q_2 &= \cos \frac{\phi}{2} \sin \frac{\theta}{2} \cos \frac{\psi}{2} + \sin \frac{\phi}{2} \cos \frac{\theta}{2} \sin \frac{\psi}{2} \\
 q_3 &= \cos \frac{\phi}{2} \cos \frac{\theta}{2} \sin \frac{\psi}{2} + \sin \frac{\phi}{2} \sin \frac{\theta}{2} \cos \frac{\psi}{2}
 \end{aligned} \tag{A.2.15}$$

***Euler angles expressed in terms of direction cosines***

$$\begin{aligned}
 \phi &= \tan^{-1} \left( \frac{C_{B\ 32}^A}{C_{B\ 33}^A} \right) \\
 \theta &= \sin^{-1} \left( -C_{B\ 31}^A \right) \\
 \psi &= \tan^{-1} \left( \frac{C_{B\ 21}^A}{C_{B\ 11}^A} \right)
 \end{aligned} \tag{A.2.16}$$

**A.3 Transformation Between Different Frames**

The different rotations between frames used in this report are described in this section. It is necessary to define these transformations with a view to obtain the different sensor measurements done in different frames [10].

### A.3.1 Transformation From ECOF to ECI and ECEF Frames

The rotation between these frames can be required for the orbit estimator model and for the comparison of the some kind of reference sensors measurements with their respective reference model. In the following equations the rotation matrix from ECOF to ECI and ECEF are given.

$$C_{OC}^I = C_z(-\Omega) C_x(-i) C_z(-\omega) \quad (\text{A.3.1})$$

$$C_{OC}^E = C_z(-\Omega + \theta) C_x(-i) C_z(-\omega) \quad (\text{A.3.2})$$

where  $\Omega$  is the Right Ascension of Ascending Node,  $i$  is the inclination of the satellite,  $\omega$  is Argument of Perigee and  $\theta$  is the ascension of the zero meridian.  $C_x$  and  $C_z$  are the different simple rotations defined by Eq. (A.2.4) and Eq. (A.2.6), respectively.

### A.3.2 Transformation From ECEF to ECI Frame

The rotation of the ECEF relative to the ECI is a rotation through angle  $\lambda = \omega_e t$  (longitude position) about reference coincident  $Z_I$  and  $Z_E$  axes, where  $\omega_e$  is the Earth rotation rate and  $t$  is the time passed since the ECEF and ECI frame were aligned. This rotation can be expressed as follows:

$$C_E^I = C_{z_I, \alpha} = \begin{bmatrix} \cos \lambda & \sin \lambda & 0 \\ -\sin \lambda & \cos \lambda & 0 \\ 0 & 0 & 1 \end{bmatrix} \quad (\text{A.3.3})$$

### A.3.3 Transformation From ECI to ORB Frame

The rotation from ECI to ORB frame is dependent on the satellite rotation velocity  $\omega_o$ . The ORB is rotated an angle  $L$  about  $Y_I$  axis and it is expressed as

$L = L_0 + \omega_o.t$ . Here  $L_0$  is the latitude position of the satellite and  $t$  is the time since last passing of  $0^\circ$  latitude. This rotation can be expressed as:

$$C_{Y_I, \beta} = \begin{bmatrix} \cos L & 0 & \sin L \\ 0 & 1 & 0 \\ -\sin L & 0 & \cos L \end{bmatrix} \quad (\text{A.3.4})$$

An additional -90 degree turn is needed about  $Y_I$  axis to obtain the Orbit frame relative to the ECI frame. This motivates the following rotation:

$$C_{Y_I, -\pi} = \begin{bmatrix} 0 & 0 & 1 \\ 0 & 1 & 0 \\ -1 & 0 & 0 \end{bmatrix} \quad (\text{A.3.5})$$

the combination of the Eq. (A.3.4) and Eq. (A.3.5) gives the total rotation which is necessary to transform a vector given in ECI frame to an ORB frame representation:

$$C_I^O = \begin{bmatrix} -\sin L & 0 & \cos L \\ 0 & 1 & 0 \\ -\cos L & 0 & -\sin L \end{bmatrix} \quad (\text{A.3.6})$$

where  $L$  represents the latitude position of the satellite.

#### A.3.4 Transformation From ECEF to ORB Frame

The rotation from ECEF to ORB frame is dependent on the latitude and longitude position of the satellite. This rotation can be expressed by the combination of the following rotations:

$$C_E^O = C_I^O . C_E^I \quad (\text{A.3.7})$$

So the total rotation which is used to transform a vector from ECEF to ORB can be written as:

$$C_E^O = \begin{bmatrix} -\sin L \cos \lambda & -\sin L \sin \lambda & 0 \\ -\sin \lambda & \cos \lambda & 0 \\ -\cos L \cos \lambda & -\cos L \sin \lambda & -\sin L \end{bmatrix} \quad (\text{A.3.8})$$

### A.3.5 Transformation From ORB to BODY Frame

The rotation matrix used frequently in this report with a view to obtain the attitude of the satellite is the transformation between Orbital frame and Body frame expressed in quaternion parameters. Using Eq. (A.2.12), rotation matrix from BODY frame to ORB frame can be expressed as follows:

$$C_B^O = \begin{bmatrix} q_1^2 - q_2^2 - q_3^2 + q_4^2 & 2(q_1q_2 - q_3q_4) & 2(q_1q_3 + q_2q_4) \\ 2(q_1q_2 + q_3q_4) & -q_1^2 + q_2^2 - q_3^2 + q_4^2 & 2(q_2q_3 - q_1q_4) \\ 2(q_1q_3 - q_2q_4) & 2(q_2q_3 + q_1q_4) & -q_1^2 - q_2^2 + q_3^2 + q_4^2 \end{bmatrix} \quad (\text{A.3.9})$$

Similarly, rotation from ORB frame to BODY frame can be written by using the orthonormality property of the matrix (Eq. (2.2.3)):

$$C_O^B = \begin{bmatrix} q_1^2 - q_2^2 - q_3^2 + q_4^2 & 2(q_1q_2 + q_3q_4) & 2(q_1q_3 - q_2q_4) \\ 2(q_1q_2 - q_3q_4) & -q_1^2 + q_2^2 - q_3^2 + q_4^2 & 2(q_2q_3 + q_1q_4) \\ 2(q_1q_3 + q_2q_4) & 2(q_2q_3 - q_1q_4) & -q_1^2 - q_2^2 + q_3^2 + q_4^2 \end{bmatrix} \quad (\text{A.3.10})$$

## A.4 Kinematics Differential Equations

In preceding sections the problem of describing the attitude of a rigid body with respect to a reference frame is studied. In this section, the kinematics, in which the

relative orientation between two reference frames is time dependent, is presented by using the kinematics differential equations. Kinematics differential equations may be derived by propagating the attitude representations with time and these propagations are formulated as follows [12] [20]:

***Propagation of the direction cosine matrix with time:***

The propagation of the direction cosine matrix is given as follows:

$$\dot{C}_B^O = C_B^B \Omega_{OB}^B \quad (\text{A.4.1})$$

where;

$$\Omega_{OB}^B = \begin{bmatrix} 0 & -\omega_z & \omega_y \\ \omega_z & 0 & -\omega_x \\ -\omega_y & \omega_x & 0 \end{bmatrix} \quad (\text{A.4.2})$$

here,  $\Omega_{OB}^B$  is the skew-symmetric matrix form of the angular rate vector  $\omega_{OB}^B = [\omega_x \ \omega_y \ \omega_z]^T$ , which represents the turn rate of the B-frame with respect to O-frame expressed in body axes.

***Propagation of the Euler angles with time:***

The propagation of the body rates depending on the Euler angles is formulated as follows:

$$\begin{bmatrix} \omega_x \\ \omega_y \\ \omega_z \end{bmatrix} = \begin{bmatrix} \dot{\phi} \\ 0 \\ 0 \end{bmatrix} + C_3 \begin{bmatrix} 0 \\ \dot{\theta} \\ 0 \end{bmatrix} + C_3 C_2 \begin{bmatrix} 0 \\ 0 \\ \dot{\psi} \end{bmatrix} \quad (\text{A.4.3})$$

The above equation can be rearranged and expressed in component form. As a result Euler angles rate expression related to the body rates can be written as follows:

$$\begin{aligned}\dot{\phi} &= (\omega_y \sin \phi + \omega_z \cos \phi) \tan \theta + \omega_x \\ \dot{\theta} &= \omega_y \cos \phi - \omega_z \sin \phi \\ \dot{\psi} &= (\omega_y \sin \phi + \omega_z \cos \phi) \sec \theta\end{aligned}\tag{A.4.4}$$

***Propagation of the quaternions with time:***

Quaternions are propagated in accordance with the following equation:

$$\dot{q} = \frac{1}{2} \Omega q\tag{A.4.5}$$

where;

$$\Omega = \begin{bmatrix} 0 & \omega_z & -\omega_y & \omega_x \\ -\omega_z & 0 & \omega_x & \omega_y \\ \omega_y & -\omega_x & 0 & \omega_z \\ -\omega_x & -\omega_y & -\omega_z & 0 \end{bmatrix}\tag{A.4.6}$$

## APPENDIX B

### SENSORS USED ON SATELLITE ADS SIMULATIONS

This appendix contains the product specification sheets of the sensors used on the satellite attitude determination system simulations.

#### B.1 Rate Gyroscopes

Navigation Systems

NORTHROP GRUMMAN

*The FOG 200 is designed for a wide range of applications requiring high reliability and long life*

### FOG 200

#### Design

The FOG 200 is a small, medium performance fiber optic gyro (0.1°/hr typical in-run drift stability). Currently Northrop Grumman produces the FOG 200 in single, dual and three axis versions. The FOG 200 is designed for a wide range of applications requiring high reliability and long life.

#### Features and Benefits

- Medium accuracy, low noise
- Available as remote single, dual and three axis versions
- Available as a single axis assembly
- Drift stability of 0.1°/hour
- High angular rate capability, 1,000 degrees/second
- Solid state, high reliability, long life
- Rugged, high vibration version available (200 g rms)

#### Applications

The FOG 200's performance and environmental capability make it suitable for a number of demanding applications including:

- Precision Camera Stabilization
- Gun Turret
- FLIR Stabilization
- Line-of-Sight Tracking
- Radar Stabilization

The gyro channels have wide bandwidth that enable the unit to be used for applications such as gimbal stabilization and motion compensation in very dynamic environments.



#### Interface

The FOG 200 has a high speed, proprietary digital interface and provides up to three axes of delta angle at wide bandwidth.

The FOG 200 requires ±5V

#### Size

Each remote FOG sensor is:  
1.2 x 2.25 x 2.25 in.  
(3.05 x 5.72 x 5.72 cm)

#### Electronics

1 - Axis 1.9 x 4.05 x 4.78 in.  
(4.83 x 10.29 x 12.14 cm)  
2 - Axis 1.09 x 4.13 x 5.75 in.  
(2.77 x 10.49 x 14.60 cm)  
3 - Axis 1.27 x 5.0 x 8.0 in.  
(3.23 x 12.7 x 20.32 cm)

#### Weight

Each remote FOG sensor	0.17 lb (0.08 kg)
1 - Axis Electronics	1.20 lb (0.54 kg)
2 - Axis Electronics	2.13 lb (0.97 kg)
3 - Axis Electronics	3.30 lb (1.50 kg)

#### Environment

These FOGs were designed and qualified for flight in a military fighter aircraft. The operating temperature range is -55° C to + 71° C.

Since FOGs are solid state instruments and have no moving parts, they generally perform better than other gyro technologies in a vibration environment.



## FOG 200

### Performance

Northrop Grumman developed the FOG 200 gyro for military applications that demand high accuracy over a wide temperature range. A summary of the gyro's performance is shown in table 1.

Any gyro's performance is affected by the operating environment. In a very benign environment, gyro bias stability (short term drift) for this FOG is approximately 0.01 deg/hr. FOG 200 performance over temperature, when modeled by the user is typically 0.25°/hr. In stable temperature conditions drift stability is 0.1°/hr.

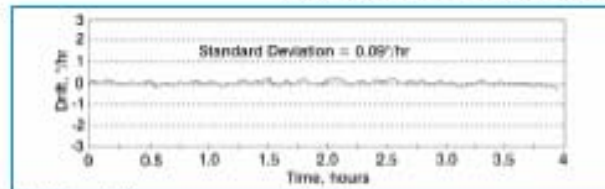


Table 1

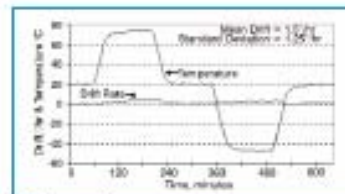
Parameter	Typical Performance*
Operating temperature	-40° C to +71° C
Power consumption**	5 watts/gro
Input voltages	±5 V
Electrical interface, digital bandwidth (higher bandwidth available)	Proprietary
MTBF	100,000 hr
Noise, angle random walk	0.012°/hr
Long-term gyro bias, over temperature	3.0°/hr
Long-term modeled bias, over temperature	0.25°/hr
Dynamic range, with standard I/O	90°/sec
Dynamic range, with non-standard I/O	760°/sec
Scale factor (0.1 arc sec with max rate of 100 deg/sec)	0.4 arc sec/LSB
Scale factor, long term stability over temperature	2,000 ppm
Scale factor, short term, fixed temperature	100 ppm
misalignment	10 m rad

\*All statistical values are one sigma \*\*At 25° C, additional 4 watts at ±55° C

The following figures show data from typical FOG 200s.

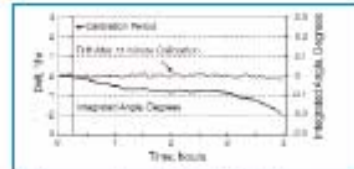


Short Term Drift



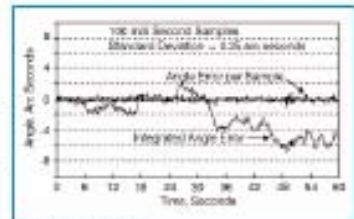
Absolute Drift Over Temperature

Performance over temperature is better than 10°/hr without any thermal modeling.



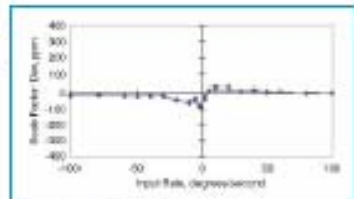
Performance after In-Flight Calibration

The data above shows the expected drift rate and heading error growth for a gyro initially aligned and calibrated against GPS.



Short Term Noise

Test data above shows both instantaneous error in arc seconds and integrated angle in arc seconds.



Scale Factor Linearity

The data above shows the excellent scale factor linearity of FOG 200 gyro and its digital signal processing.

For more information, please contact:

Northrop Grumman Corporation  
Navigation Systems  
21240 Burbank Boulevard  
Woodland Hills, CA 91367 USA  
1-866-NGN6SYS(646-2879)  
www.nsls.northropgrumman.com

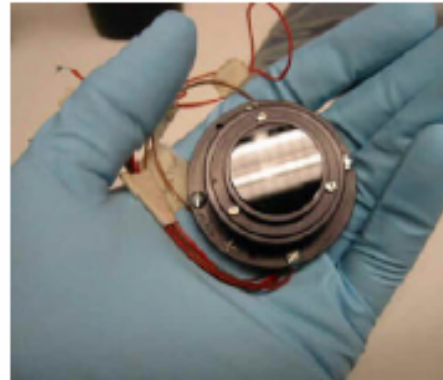
## B.2 Sun Sensor



[HOME PAGE](#)  
[SUNSENSORS](#)  
[ELECTRO-  
OPTICAL  
INSTRUMENTS](#)  
[INFRARED  
SOURCES](#)  
[SOLAR PANELS](#)  
[CONTACT US](#)  
[E-MAIL](#)

## SUN SENSORS

MODEL 0.5 SUN SENSOR



### FEATURES

- $\pm 0.5^\circ$  TWO AXIS SUN READOUT ACCURACY OVER  $100^\circ$  FIELD
- EARTH ALBEDO ERROR MINIMIZATION
- WEIGHT = < 40 grams
- POWER = < 50 mwatts
- RELIABILITY =  $> 0.999$  FOR A 15 YEAR MISSION
- ACTIVE PARTS COMPLEMENT COMPRISES ONLY ONE QUAD
- S LEVEL PARTS AVAILABLE WITH QUANTITY ORDERS
- SUITABLE FOR LEO, GEO, OR INTERPLANETARY APPLICATION
- PROPRIETARY SIGNAL PROCESSING SOFTWARE INCORPORATED INTO MICROCONTROLLER COMPUTER, REQUIRING < 100 KBYTES OF MEMORY
- + 5 TO + 15 VOLT POWER INPUT
- QUALIFIED FOR 2002 FLIGHT ON CUBESAT SPACECRAFT:
  - $-30^\circ\text{C}$  TO  $+80^\circ\text{C}$  THERMAL VACUUM (3 CYCLES)
  - $0.16 \text{ g}^2/\text{Hz}$ . 50-800 Hz. RANDOM VIBRATION



Magnetometers measure the external magnetic field for the purpose of attitude determination and for the prediction of the torque applied by magnetic torquers.

Magnetometers have been part of the attitude determination and control system (ADCS) of many satellite missions since the start of space-flight. They are simple, robust and provide a moderate accuracy for the magnetic flux vector measurement.

ZARM has teamed with Microcosm to provide high performance magnetometers and system support that meet all your program requirements and keep your budget and schedule on target.

Our production process meets the highest standards for performance and workmanship, with excellent quality control.

## Design Features

- Aluminum alloy housing
- Radiation protection enclosure for the sensor and electronics inside the housing
- All components are surface mounted devices (SMD)
- Double insulated fluxgate sensor wires
- MIL-C 24308 non-magnetic connectors
- Titanium bolts and housing parts

## Off-the-Shelf Equipment

Measurement Type	Fluxgate (1000)	FCM Analog
Resolution	40 to 40 pT	40 to 40 pT
Standard Measurement Rate	30 pT per pT	30 pT per pT
Dynamic Range	<math>10^3</math> pT to <math>10^5</math> pT	<math>10^3</math> pT to <math>10^5</math> pT
Power Consumption	<math>100</math> mW	<math>100</math> mW
Power Supply	3.3V to 5V	3.3V to 5V
Output	<math>1</math> to <math>10</math> bits	<math>1</math> to <math>10</math> bits
Size	1.5" x 1.5" x 1.5"	1.5" x 1.5" x 1.5"
Weight	<math>10</math> grams	<math>10</math> grams
Frequency Response	<math>10</math> Hz to <math>10</math> kHz	<math>10</math> Hz to <math>10</math> kHz
Temperature Operating Range	<math>10</math> to <math>50</math> C	<math>10</math> to <math>50</math> C
Interface	Analog/Serial	Analog/Serial
Electromagnetic Interference Immunity	<math>10</math> dB to <math>10</math> dB	<math>10</math> dB to <math>10</math> dB
Physical Dimensions	1.5" x 1.5" x 1.5"	1.5" x 1.5" x 1.5"
Weight	10 grams	10 grams
Connector	Spacecraft-Style	Spacecraft-Style
Footprint	1.5" x 1.5"	1.5" x 1.5"
Options	<ul style="list-style-type: none"> <li>Dual Configuration</li> <li>3-axis or 6-axis</li> <li>Radiation tolerant (1000)</li> </ul>	<ul style="list-style-type: none"> <li>Dual Configuration</li> <li>3-axis or 6-axis</li> <li>Radiation tolerant (1000)</li> </ul>
Operating Temperature	Operating Temperature	Operating Temperature
Operating Voltage	Operating Voltage	Operating Voltage
Output Impedance	Output Impedance	Output Impedance

NOTE: All data is for a 1000 series magnetometer. Components are subject to change without notice.



Fluxgate Sensor Manufacturing and Final Design

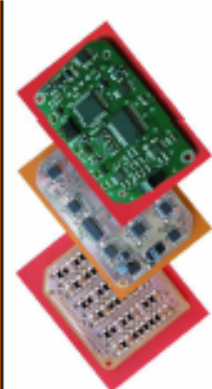
## Performance

- Low power consumption
- Low mass and size
- Good linearity and accuracy
- Radiation tolerant - 50 kRAD

Two different sensor concepts, dedicated to measure the magnetic fields onboard a satellite within ADCS systems:  
 ► Fluxgate based instruments with noise below 1 nT.  
 ► Anisotropic magneto resistive (AMR) based instruments with lower resolution, but compact size.

Measurement Type	Fluxgate	AMR Analog	AMR Digital
Resolution	40 to 40 pT	40 to 40 pT	40 to 40 pT
Standard Measurement Rate	30 pT per pT	30 pT per pT	30 pT per pT
Dynamic Range	<math>10^3</math> pT to <math>10^5</math> pT	<math>10^3</math> pT to <math>10^5</math> pT	<math>10^3</math> pT to <math>10^5</math> pT
Power Consumption	<math>100</math> mW	<math>100</math> mW	<math>100</math> mW
Power Supply	3.3V to 5V	3.3V to 5V	3.3V to 5V
Output	<math>1</math> to <math>10</math> bits	<math>1</math> to <math>10</math> bits	<math>1</math> to <math>10</math> bits
Size	1.5" x 1.5" x 1.5"	1.5" x 1.5" x 1.5"	1.5" x 1.5" x 1.5"
Weight	<math>10</math> grams	<math>10</math> grams	<math>10</math> grams
Frequency Response	<math>10</math> Hz to <math>10</math> kHz	<math>10</math> Hz to <math>10</math> kHz	<math>10</math> Hz to <math>10</math> kHz
Temperature Operating Range	<math>10</math> to <math>50</math> C	<math>10</math> to <math>50</math> C	<math>10</math> to <math>50</math> C
Interface	Analog/Serial	Analog/Serial	Digital/Serial
Electromagnetic Interference Immunity	<math>10</math> dB to <math>10</math> dB	<math>10</math> dB to <math>10</math> dB	<math>10</math> dB to <math>10</math> dB
Physical Dimensions	1.5" x 1.5" x 1.5"	1.5" x 1.5" x 1.5"	1.5" x 1.5" x 1.5"
Weight	10 grams	10 grams	10 grams
Connector	Spacecraft-Style	Spacecraft-Style	Spacecraft-Style
Footprint	1.5" x 1.5"	1.5" x 1.5"	1.5" x 1.5"
Options	<ul style="list-style-type: none"> <li>Dual Configuration</li> <li>3-axis or 6-axis</li> <li>Radiation tolerant (1000)</li> </ul>	<ul style="list-style-type: none"> <li>Dual Configuration</li> <li>3-axis or 6-axis</li> <li>Radiation tolerant (1000)</li> </ul>	<ul style="list-style-type: none"> <li>Dual Configuration</li> <li>3-axis or 6-axis</li> <li>Radiation tolerant (1000)</li> </ul>
Operating Temperature	Operating Temperature	Operating Temperature	Operating Temperature
Operating Voltage	Operating Voltage	Operating Voltage	Operating Voltage
Output Impedance	Output Impedance	Output Impedance	Output Impedance

Your custom design



Electronic Board: FCM analog, AMR analog, AMR digital

ZARM's Microcosm's experience includes specialists in both hardware definition as well as production.

Services include:

- Magnetometer system engineering and attitude control subsystem design support
- Fabrication and testing of high-performance magnetometers
- High-precision ADCS system simulations
- Development of the overall solution of your project

ZARM was established in 1985 and has become one of the most important centers for applied space and production technologies in Europe. Microcosm has been in the business of finding technologies to reduce Space mission costs for more than a decade.

Together we have committed to providing cost-effective magnetometer solutions for space projects from small, low-cost single satellites to large-scale constellations.

## B.3 Star Sensor

### ■ ■ ■ ASTRO 15 Autonomous Star Sensor

The ASTRO 15 is Jena-Optronik's most advanced star sensor product. Its design reflects more than 20 years experience in star sensor development. ASTRO 15 is a flight proven, autonomous star tracking system for 3-axis attitude determination for long-term GEO and LEO missions for telecom, science and Earth observation. ASTRO 15 represents a single box design.

More than 30 flight units of the ASTRO 15 sensor have been ordered for Geostationary Communication/ Earth Observation satellites. E.g., ASTRO 15 is the standard star sensor for Boeing's 702 platform.

#### Key Features

- high accuracy, full autonomy and state-of-the-art technology
- modular composition of functional sensor units for flexible construction and application
- radiation-hard electronic components plus very efficient radiation shielding
- high robustness of identification algorithms
- high slew rate capability
- life time more than 15 years

#### Technical Data

<b>Dimensions:</b>	Ø 192 mm height 440 mm (incl. baffle)
<b>Mass:</b>	4.3 kg (without baffle)
<b>Standard Sun Shades:</b>	25° Sun Exclusion Angle (mass 1.6 kg) 30° Sun Exclusion Angle (mass 1.5 kg) (other angles optional)
<b>Power:</b>	Star Tracker: < 9.0 W Autonomous Sensor: < 10.0 W Peltier Cooler: < 5.0 W
<b>Temperature:</b>	Operational: -20°C...+55°C Non-operational: -40°C...+75°C
<b>Lens system:</b>	refractive Focal Length: 55.0 mm Aperture: Ø 50 mm
<b>CCD Resolution:</b>	1024 [h] x 1024 [v]
<b>CCD-Cooling:</b>	active Peltier cooler passive radiator cooling possible (option)
<b>Sensor Performance:</b>	Field of View: 13.8° x 13.8° (phys.); 13.25° x 13.25° (eff.) Star Accuracy (BOI): bias: ≤ 2.5 arcsec (1σ) noise: ≤ 2.5 arcsec (1σ) (6.0 m <sub>r</sub> star) LOS Accuracy (BOI): ≤ 1 arcsec (1σ), pitch/yaw ≤ 10 arcsec (1σ), roll Sensitivity: 6.5 m <sub>r</sub> G0-star (at t=250ms) Slew Rate: 0.0 .. 0.3°/s with full accuracy 0.3 .. 2.0°/s with reduced accuracy Update rate: 4 Hz, tracking & attitude determination (quaternion output)
<b>Operating Modes:</b>	Standby, Search & Track 3-Axis Attitude Determination Load/Dump Mode, Self Test Mode
<b>Data Interface:</b>	MIL 1553 B, RS 422

Jena-Optronik GmbH, Pflauringstr. 41, D-07745 Jena, Germany  
Phone: +49 (0)3641 200 110, Fax: +49 (0)3641 200 222, e-mail: info@jena-optronik.de  
<http://www.jena-optronik.de>

April 2004

# APPENDIX C

## SENSORS USED ON SACOTS

This appendix contains the product specification sheet of the IMU used on the satellite attitude control test setup simulations.

### VG700

FIBER OPTIC VERTICAL GYRO SYSTEM

- ▼ Fiber Optic Gyro Stability < 20"/hr
- ▼ Fully Compensated Angular Rate and Linear Acceleration Outputs
- ▼ SAE (Earth Coordinate) Navigation Frame
- ▼ Automotive Compatible 10-30 VDC Input Supply

#### Applications

- ▼ Automotive Testing



#### VG700AB

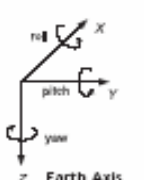
The Crossbow VG700AB is designed specifically for automotive test applications. It combines Crossbow's third generation high performance fiber optic gyros with the latest in silicon micro-machined (MEMS) accelerometer technology to provide a highly accurate dual function Vertical Gyro (VG) and Inertial Measurement Unit. The new third generation FOG sensor provides excellent bias stability of < 20"/hr (constant temp.) and low noise.

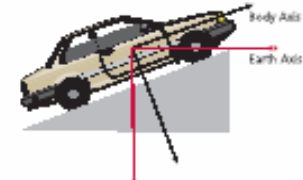
The VG700AB is available in two configurations: earth coordinates or body coordinates. The VG700AB-201 provides roll and pitch angle; roll, pitch and yaw angular rate; and X, Y, Z tangential acceleration (earth coordinate) in accordance with SAE Navigation Frame definition. The VG700AB-202 provides

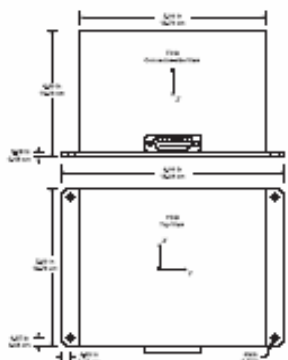
roll and pitch angle; roll, pitch and yaw angular rate; and X, Y, Z body-axis acceleration.

The VG700AB consists of three fiber optic rate gyros, three silicon accelerometers, a high-performance DSP and automotive power supply all packaged in one small (6" x 5" x 4") aluminum housing. Fully compensated angular rate and linear acceleration outputs are provided in addition to the roll and pitch angles. Data is available in both analog and digital (RS-232) formats.

Each Inertial System comes with a User's Manual offering helpful hints on programming, installation, and product information. In addition, Crossbow's GYRO-VIEW software is included to assist you in system development and evaluation, and allows you to perform data acquisition.







inertial systems

72

Document Part Number: 6030-0039-12 Rev D

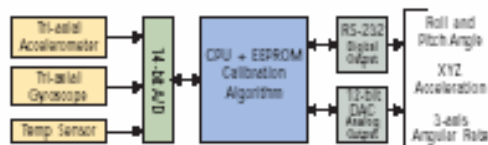
crossbow technology, inc ▼ 4145 n. first street ▼ san jose, ca 95134-2109

165

Specifications	VG700AB-201 VG700AB-202	Remarks
<b>Performance</b>		
Update Rate (Hz)	> 100	Continuous Update Mode
Start-up Time Wild Data (sec)	< 1	
<b>Attitude</b>		
Range: Roll, Pitch (°)	± 180, ± 90	
Static Accuracy (°)	< ± 0.75	
Dynamic Accuracy (° rms)	2.5	
Resolution (°)	< 0.1	
<b>Angular Rate</b>		
Range: Roll, Pitch, Yaw (°/sec)	± 200	
Bias: Roll, Pitch, Yaw (1/yr)	< ± 20	Constant temp.
Scale Factor Accuracy (%)	< 2	Over temp.
Non-Linearity (1/yr)	< 1	Up to 100 °/sec.
Resolution (°/sec)	< 0.025	
Bandwidth (Hz)	> 100	-3 dB point
Random Walk (1/yr) <sup>1/2</sup>	< 0.4	
<b>Acceleration</b>		
Range: XYZ (g)	± 4	
Bias: XYZ (mg)	< 12	
Scale Factor Accuracy (%)	< 1	
Non-Linearity (1/yr)	< 1	
Resolution (mg)	< 0.6	
Bandwidth (Hz)	> 10	-3 dB point
Random Walk (1/yr) <sup>1/2</sup>	< 1.0	
<b>Environment</b>		
Operating Temperature (°C)	-40 to +60	
Non-Operating Temperature (°C)	-55 to +95	
Non-Operating Vibration (g rms)	5	20 Hz - 2 KHz random
Non-Operating Shock (g)	100	1 ms half sine wave
<b>Electrical</b>		
Input Voltage (VDC)	10 to 30	
Input Current (A)		< 0.75
Power Consumption (W)	< 8	At 15V DC
Digital Output Format	RS-232	
Analog <sup>2</sup> Range (VDC)	± 4.096	Pins 8, 9, 10, 12, 13, 14
	0 to 5.0	Pins 5, 6, 7
<b>Physical</b>		
Size (in)	5.0 x 6.0 x 4.0	Incl. mounting flanges
(cm)	12.70 x 15.24 x 10.16	Incl. mounting flanges
Weight (lbs)	< 3.5	
(kg)	< 1.6	
Connector	15 pin sub-miniature "D" male	

Notes

- <sup>1</sup> Non-Linearity specified at less than 1% FS over entire range.
- <sup>2</sup> All DAC analog outputs are fully buffered and are designed to interface directly to data acquisition equipment.
- Specifications subject to change without notice.

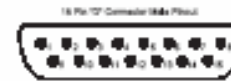


VG Block Diagram

Ordering Information

Model	Description	Gyro (°/sec)	Accel (g)	Axis Coordinates
VG700AB-201	Fiber Optic Vertical Gyro	± 200	± 4	Earth
VG700AB-202	Fiber Optic Vertical Gyro	± 200	± 4	Body

CALLFACTORY FOR OTHER CONFIGURATIONS



Pin	Function
1	RS-232 Transmit Data
2	RS-232 Receive Data
3	Input Power
4	Ground
5	X-axis accel analog voltage <sup>1</sup>
6	Y-axis accel analog voltage <sup>1</sup>
7	Z-axis accel analog voltage <sup>1</sup>
8	X-axis tangent accel scaled analog voltage <sup>2</sup>
9	Y-axis tangent accel scaled analog voltage <sup>2</sup>
10	Yaw rate analog voltage <sup>2</sup>
11	NC - Factory Use Only
12	Roll angle analog voltage <sup>3</sup>
13	Pitch angle analog voltage <sup>3</sup>
14	Z-axis tangent accel scaled analog voltage <sup>2</sup>
15	NC - Factory Use Only

- <sup>1</sup> The accelerometer voltage outputs are derived directly from the accelerometers without compensation or scaling. They represent acceleration in body axis coordinates.
- <sup>2</sup> The angular rate analog outputs are scaled to represent degrees per second. These outputs are scaled by a 0.0 constant.
- <sup>3</sup> Analog output depends on IMU measurement mode. The pitch output is for angle mode, in angle mode pin 12 is roll angle, pin 13 is pitch angle, pin 8 is Z-axis acceleration. For frame, pin 8 is Z-axis acceleration. For frame, and pin 14 is Z-axis acceleration. For frame. See manual for details.

Navigation frame is defined as the air system that is in the same plane as the earth coordinate system.

VG700AB-201 Pin Diagram\*

\*For VG700AB-202 pins 8, 9, 14 output body frame acceleration in angle mode.



inertial systems

## **APPENDIX D**

### **THREE AXIS SATELLITE ATTITUDE CONTROL TEST SETUPS**

This appendix presents the details about the satellites test setups that are mentioned on the Section 4.1. The characteristics of the investigated test setups are listed as follows:

#### **D.1 TASS (Three Axis Satellite Simulators)**

TASS and TASS-2 are the three axis satellite test simulator that exist at Naval Postgraduate School (Monterey, California). TASS is the first generation of the satellite simulator. Attitude determination of the TASS contains one 3 axis rate gyros, one 3 axis sun sensor and one 3 axis magnetometer. The signal processing algorithms are used because of the high level noises occurred on the sensor measurements. Two light sources are used in order to obtain three axis attitude information from the sun sensor, one of them provide the roll and pitch angles measurements, the other provide the yaw angle measurement. Here, it is seen that it is very difficult to adjust the sun sensor and it is important to select the right light sources for acquiring a correct measurements. It is also stated that magnetometer is never used during the tests because of its noisy measurements.

The second generation of TASS, called TASS-2, contains more complex sensor system in order to obtain accurate attitude knowledge. In this test setup one Inertial Measurement Unit (including 3 axis rate gyro and 3 axis accelerometer), 3 axis magnetometer, 3 axis inclinometer and 3 axis sun sensor are used. The following figures show the configuration of the TASS and TASS-2 respectively [6]



**Figure App.D.1: TASS [6]**

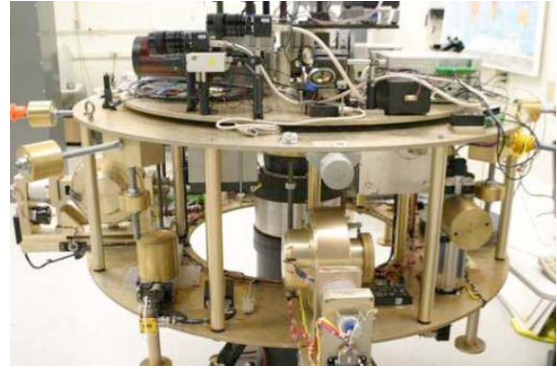


**Figure App.D.2 TASS-2 [6]**

## **D.2 WHORL-1 and WHORL-2**

WHORL-1 and WHORL-2 are the test setups used to carry out the formation flight tests. These test setups belong to Virginia Polytechnic Institute and State University (Blacksburg, Virginia, USA). WHORL-1 is a tabletop style and WHORL-2 is a dumbbell style spherical air bearing. The dumbbell style provides more rotational freedom in three axis as seen on the following figures. The only sensor used in both of the system is the Inertial Measurement Unit containing 3 axis rate gyros and accelerometer. Here rate gyros are used as inertial sensor and accelerometers are used as reference sensor by comparing its measurements with the gravity vector direction [7].

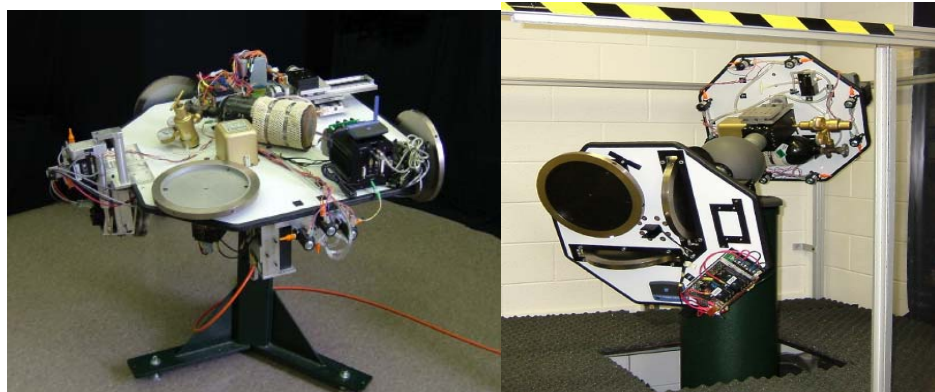


**Figure App.D.3: WHORL-1 and WHORL-2 [7]**

### D.3 IACS-1 and IACS-2

IACS-1 (Integrated Attitude Control System) and IACS-2 are respectively the first and the second generation satellite test setups of the Georgia Institute of Technology. The sensor system of the first generation contains only a dynamic measurement unit-attitude heading referenced sensor (DMU-AHRS [Crossbow Technologies, Inc]) including 3 axis rate gyros, accelerometer and magnetometer. In the IACS-2 sensor packet is completely different. A 3 axis rate gyros (RG02-32) is used as inertial sensor and reference sensors packet contains 3 axis magnetometer (Humphrey (Goodrich Sensor Systems) FM02-0101), 2 axis sun sensor (by ACEi, Corp.). the following figures show the configuration of the IACS-1 and IACS-2 respectively [8] [9].

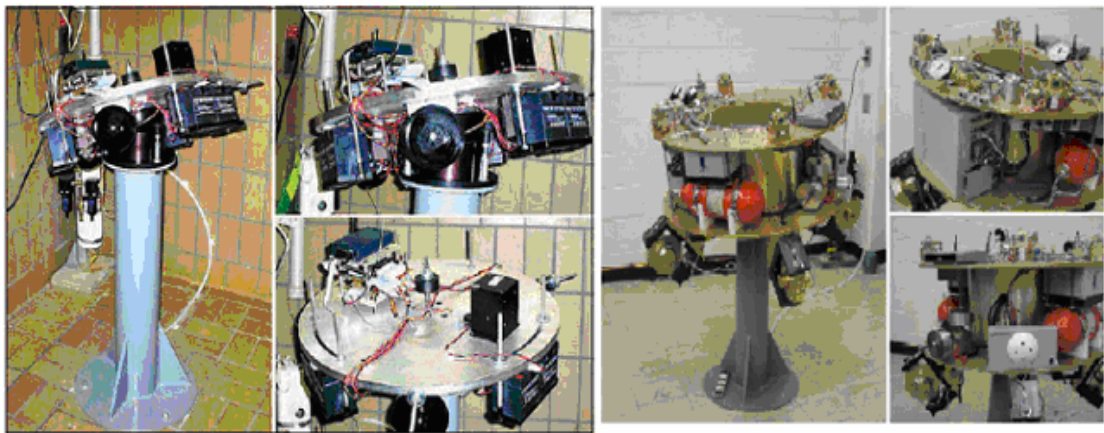


Figure App.D.4: IACS-1 and IACS-2 [8][9]